Dissertation

submitted to the

Combined Faculties of the Natural Sciences and Mathematics

of the Ruperto-Carola-University of Heidelberg, Germany

for the degree of

Doctor of Natural Sciences

Put forward by
Matthew Raymond Gent
born in: Kettering, United Kingdom
Oral examination: 17.07.2023

"Validation and Application of The *Stellar Abundances and atmospheric Parameter Pipeline* to derive fundamental parameters of stars in the era of large-scale stellar surveys"

Referees: Dr. Maria Bergemann, Priv. Dr. Andreas Koch-Hansen

Topic in German - Summary in German (max 200 words)

SAPP ist eine Pipeline zur Bestimmung genauer Parameter von Sternen in großen Durchmusterungen wie Gaia-ESO und Gaia. Sie kombiniert verschiedene Beobachtungen, darunter Spektren, Photometrie, Astrometrie und asteroseismische Daten, mit Hilfe von Bayes'schen Schlussfolgerungen. SAPP wurde anhand von Vergleichssternen validiert und bricht Entartungen zwischen Parametern auf, was zu präzisen Ergebnissen führt. Bei der effektiven Temperatur liegt der typische Fehler bei etwa 100 K, wobei spektroskopische Modelle die Unsicherheit dominieren. Die Unsicherheit von Log(g) hängt von den Beobachtungsdaten ab und reicht von 0,03 dex bis 0,06 dex. Die Metallizitäten werden mit einer Genauigkeit von 0,03 dex für PLATO-Ziele ermittelt, die durch seismische Prioritäten verbessert wird. SAPP verwendet auch ein iteratives Schema, das die Beziehung max = f(Teff, log g) verwendet und robuste Ergebnisse mit kleinen Unterschieden in Temperatur und Metallizität liefert. Es liefert fundamentale Parameter mit einer Genauigkeit von 1%, erfüllt die Ziele von PLATO und ermöglicht die Erforschung der galaktischen Struktur, einschließlich der radialen Migration und der Alters-Metallizitäts-Relation. SAPP wird verwendet, um die -armen und -reichen Populationen in der galaktischen Scheibe mit Hilfe von Gaia-ESO-Spektren, Gaia EDR3-Astrometrie und Photometrie zu untersuchen. Nichtlokale thermodynamische Gleichgewichtsmodelle bestimmen Parameter und Häufigkeiten. Eine kalte, metallarme -arme Scheibe wird in lokalen Verteilungen gefunden, was auf eine gemeinsame Entwicklung der dicken und dünnen Scheibe hindeutet. Diese Verteilungen zeigen gut definierte Trends im Alter und im kinematischen Raum (V_ϕ). Die genauen Alters- und Häufigkeitsschätzungen von SAPP tragen zum Verständnis der galaktischen Eigenschaften bei, wie z. B. Messungen des radialen Gradienten.

Topic in English - Summary in English (max 200 words)

SAPP is a pipeline designed to determine accurate parameters of stars in large surveys like Gaia-ESO and Gaia. It combines various observations, including spectra, photometry, astrometry, and asteroseismic data, using Bayesian inference. Validated with benchmark stars, SAPP breaks degeneracies between parameters, yielding precise results. For effective temperature, the typical error is about 100 K, with spectroscopic models dominating uncertainty. Log(g) uncertainty depends on observables, ranging from 0.03 dex to 0.06

dex. Metallicities are recovered with a precision of 0.03 dex for PLATO targets, improved by seismic priors. SAPP also employs an iterative scheme using max = f(Teff, log g) relation, yielding robust results with small differences in temperature and metallicity. It provides fundamental parameters accurate within 1%, meeting PLATO's goals and enabling exploration of the Galactic structure, including Radial Migration and Age Metallicity Relation. SAPP is used to investigate the -poor and -rich populations in the Galactic disc using Gaia-ESO spectra, Gaia EDR3 astrometry, and photometry. Non-Local Thermodynamic Equilibrium models determine parameters and abundances. A cold metal-poor -poor disc is found in local distributions, suggesting co-evolution of the thick and thin disc. These distributions show well-defined trends in age and kinematic space (V_ϕ). SAPP's accurate age and abundance estimations contribute to understanding Galactic characteristics such as Radial Gradient Measurements.

Contents

List of Figures

List of Tables

Abstract

We introduce the Stellar Abundances and atmospheric Parameters Pipeline (SAPP) pipeline that will be used to determine the classical parameters of stars observed within large stellar surveys such as Gaia-ESO, Gaia and eventually the PLATO space mission. The pipeline has been designed with the goal to return accurate and precise characterisation of surface stellar parameters, including effective temperature, surface gravity, metallicity, and detailed chemical abundances. We use the Bayesian inference method to combine observations of a star from different telescopes, including high-resolution wide-band stellar spectra, photometry in different bands, astrometry, asteroseismic constraints, and Infra-Red flux method. We validate the code on a set of 22 benchmark stars that includes 19 FGK -dwarfs and 3 GK-subgiants. Our results suggest that combining various observables is the most optimal approach, as it allows to break numerous degeneracies between different parameters. This yields more accurate values of stellar parameters and more realistic uncertainties associated with them. For effective temperature, we obtain the typical combined (statistical + systematic) error of ≈ 100 K as spectroscopic models dominate in statistical uncertainty. For log(g) the uncertainty depends strongly on the type and precision of observables, and ranges from 0.03 dex to 0.06 dex in the best case, when accurate parallaxes and asteroseismic data are available. Metallicities can generally be recovered to the precision of 0.03 dex in the parameter space of PLATO targets. The accuracy of [Fe/H] estimates improves with the inclusion of seismic priors. We also show that a direct iterative scheme, that employs the empirical $\nu_{\rm max} = {\rm f}(T_{\rm eff}, \log g)$ relation, and iterating with spectroscopic calculations returns robust results, with $T_{\rm eff}$ differences of the order 20 K for the majority of stars. The effect on metallicity is below 0.03 dex. Therefore, SAPP will provide fundamental parameters accurate to within 1% which satifies PLATO's requirements necessary to achieve its scientific goals. Accurate age and chemical abundance estimations from SAPP signify it's ability to explore the Galactic structure by further understanding characteristics such as Radial Migration, Age Metallicity Relation and Radial Gradient Measurements. Thus, we use the SAPP to investigate the chemical, temporal, and kinematical structure of the α-poor and α-rich populations in the Galactic disc. We employ the medium-resolution spectra from the Gaia-ESO large spectroscopic survey, as well as Gaia EDR3 astrometry and photometry. The stellar parameters and chemical abundances are determined using Non-Local Thermodynamic Equilibrium (NLTE) models of syn-

thetic spectra. Ages are computed for a large sample of subgiants, turn-off, and late main sequence stars using `Garstec` evolutionary tracks. We find evidence of a cold metal poor alpha poor disc in the $[\alpha/\mathrm{Fe}]$ distributions in the local volume. Of which a sub-sample of older stars exist from this disc within a temporal overlap which could be explained by co-evolution of the thick and thin disc. These distributions are characterised by well defined trends in the space of age- and kinematic (V_{ϕ}).

A short recognition...

I would like thank the Max Plank Institute for Astronomy (MPIA) for hosting my doctoral research and my supervisor Dr Maria Bergemann for taking me under her wing, introducing me to PLATO, 4MOST, and WEAVE surveys and the opportunity to research in her group.

I would like to thank colleagues and the working professionals at MPIA for their help, contributions to a suitable work environment despite large impacts from the pandemic.

I am very grateful for Dr Andreas Koch for agreeing to review my thesis, and I wish to thank Prof. Dr. Friedrich Röpke and Prof. Dr. Matthias Bartelmann for willingly joining my examination committee.

I would like to thank members of PLATO, 4MOST and WEAVE for welcoming me to their working groups, introducing and developing SAPP as well as lending expertise in developing the pipeline. I would like to give special thanks to Thierry Morel, the head of Work Package 122 of PLATO.

I would like to acknowledge my collaborators: Jeffrey Gerber, Aldo Serenelli, Maria Bergeman, and more listed in the authorship of my first paper which took a long time to develop as one of the first official PLATO endorsed papers. I am very grateful for my collaborators in my second on-going paper: Phillip Eitner (a fellow PhD student in my group at MPIA), Chervin Laporte, Aldo Serenelli, Sergey Koposov, and of course Maria Bergemann. I especially would like to thank Jennifer Friske for joining recently and providing helpful contributions towards the paper with respect to Galactic dynamics.

I would like to thank my family for supporting me, checking on me despite my response time, and especially my brother Luke Gent, for giving statistical help and encouraging me constantly.

Lastly, I would like to thank everyone at MPIA whom I consider my friends, you know who you are, thank you for sticking around despite spending most of our PhD in home office.

Chapter 1

Introduction

1.1 Motivation

The past decade has seen revolutionary developments in astronomical surveys and large-scale observational programs aimed at assembling high-quality data for millions of stars in the Galaxy, most notably the Gaia space mission (Gaia Collaboration et al. 2016). Much of the early efforts were motivated by using stars as tracers of Galactic structure and evolution, for example: Gaia-ESO (Gilmore et al. 2012a), LAMOST (Chu & Cui 1996), RAVE (Steinmetz et al. 2006), APOGEE (Majewski et al. 2007). These have allowed us to pursue one of the main quests in modern astrophysics: to understand the formation history of the Milky Way.

In order to study the formation history, several key sources of information are required which provide the following: phase-space information, ages, elemental abundances for a large number of stars within the Galaxy. There are three main constraints on the formation history of the Galaxy this study aims to explore: Galactic merger history, growth rate of the disk, and radial migration of stars. What do these mean and what do we need to start our quest?

1.2 What is known about the Galactic structure?

The Milky way is a large spiral galaxy with the approximate age of 13 Gyr (close to the age of the universe) (Cayrel et al. 2001; Cowan et al. 2002). It can be decomposed into three primary parts: Halo, Disc and Bulge (Tolstoy et al. 2009). Fig. 1.1 is a basic schematic of the Milky way showing these different parts as well as depicting globular clusters.

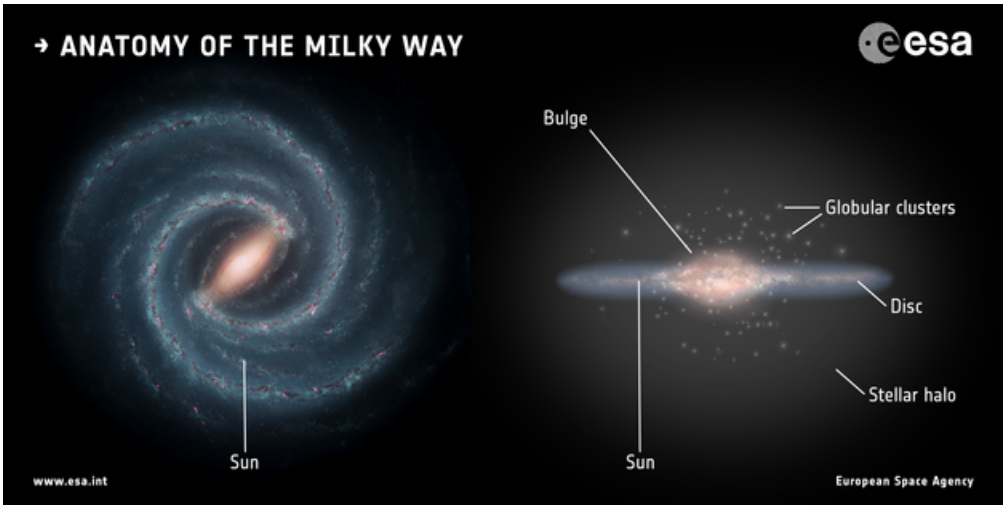

Figure 1.1: Anatomy of the Milky Way depicted by NASA/JPL-Caltech (left) as seen from above perpendicular to the Galactic plane. ESA figure (on right) is from the perspective edge-on to the Galactic disk.

The best way to distinguish and explore the evolution of these structural components of the Galaxy is to understand the main physical properties of their stellar populations (Freeman & Bland-Hawthorn 2002; Bland-Hawthorn & Gerhard 2016a; Barbuy 2019). These are characterised by a distinct distribution of ages, chemical compositions, stellar densities, and kinematics.

The common view of the main attributes of the Galactic disc is that it can be split into two major components: thick and thin disc Mitschang et al. (2014); Bergemann et al. (2014); Bensby et al. (2014). The thick disc stars are old, metal poor and have large dispersions in their vertical space motions. The thin disk, on the other hand, is young, metal rich and have a small vertical velocity dispersion (Bensby et al. 2003; Nordström et al. 2004b; Bensby et al. 2005; Anguiano et al. 2012). Evidence of the presence of a Galactic thick disc was first presented by Gilmore & Reid (1983), showing that the density of stars as a function of the vertical distance (Z) from the Galactic plane could not be explained by a single exponential. Several observational studies that followed have established that compared to the thin disc, the thick disc has a stellar population that is kinematically hotter, it rotates about the Galactic centre more slowly, lastly that it has different chemical properties, mainly higher [α/Fe] ratios at a given metallicity (Bensby et al. 2003, 2005; Reddy et al. 2006; Bensby et al. 2007; Fuhrmann 2008; Feltzing & Bensby 2009). The bulge is barred and X-shaped with a core that contains nuclear star clusters and a super massive black hole (Sagitarrius A*) with a mass of 4.1×10^6 $M_\odot$ (Ness & Lang 2016; Barbuy et al. 2018). The inner regions of the bulge

contain lots of stellar populations with stars as old as 13 Gyrs (Barbuy et al. 2018) .

The stellar Halo in terms of mass is mostly Dark matter. Similar to the bulge it is also thought to host the oldest stars in the Universe, with ages above 13 Gyrs and highly eccentric orbits (Belokurov et al. 2006), (White & Croft 2000). Many studies such as (example REFERERENCES MISSING) find sub-structure within the Halo, stellar streams and over-densities.

Using accurate age-dating methods, parallaxes (thus distances), and abundance estimation we can discern the time evolution of the chemical structure of the Galaxy. Comparing the plethora of observations with theoretical models we can identify the role of various processes such as in-fall, outflow, radial migration acting to shape the geometry, dynamics and chemistry of the Galaxy.

Spiral star-forming galaxies have their baryonic matter dominated by the disc which has a non-uniform metallicity and usually decreases with distance to the Galactic Centre. This trend is called the Radial Metallicity Gradient (henceforth known as RMG) Stanghellini et al. (2019). This has been known for a long time, starting with work pioneered by Aller (1942), and later by Searle (1971), and Pagel & Edmunds (1981). A vertical gradient also exists and has been investigated by several studies such as Cheng et al. (2012a); Schlesinger et al. (2014) whom reach different conclusions on how distinct thick and thin disc stellar populations are. However, it can be agreed that inspecting different elements at different epochs allows one to track disc evolution. Determining formation scenarios for any part of the disc where it is vertical or radial in direction requires the ages of stellar populations.

Of the most recent studies, Bergemann et al. (2014) derived an RMG specific to [Fe/H] and [Mg/Fe][1]. Fig. 1.2 shows four panels, describing how stars are distributed with the vertical distance from the Galactic plane (Z) and Galactocentric radius (R).

The second and third panel show iron and magnesium metallicity versus Galactic radius with Age as the colour scale in Gyrs. Three open clusters (NGC6705, Trumpler20, NGC4815) are also plotted as representative stellar populations.

[1]The abundance ratio is defined as the logarithm of the ratio of a star's iron abundance compared to that of the Sun: [Fe/H] = $\log(N_{Fe}/N_H)$ - $\log(N_{Fe}/N_H)_\odot$, where N_{Fe} and N_H are the number of iron and hydrogen atoms per unit of volume respectively. The square brackets represent this ratio to the Solar abundances. Since these are logarithm in form, we define Magnesium abundance as: [Mg/Fe] = [Mg/H] - [Fe/H]

With these gradients, one can make several different interpretations in regards to disc formation.

The first panel shows the spatial age distribution of the stars and we can see clear trends, with the oldest stars increasing in number as we go away from the plane. However, this distribution is not symmetric with respect to positive and negative Z. Bergemann et al. (2014) calculated [Fe/H], [Mg/Fe] - Radius gradients for different intervals of Z. This allowed them to probe the inner and outer disc of the Galaxy separately. They found that stars close to the plane (within |Z| of 300 pc) have a Δ[Fe/H]/ΔR value of -0.068 $\pm$ 0.0014 dex/kpc which is more than that of the outer part of the plane ($300 \leq Z_{max} \leq 800$ pc) -0.114 $\pm$ 0.009 dex/kpc. This was surprising as other studies found flatter or positive RMG at larger vertical distances to the plane. However it was discussed that this result could be due to the small data set the study had.

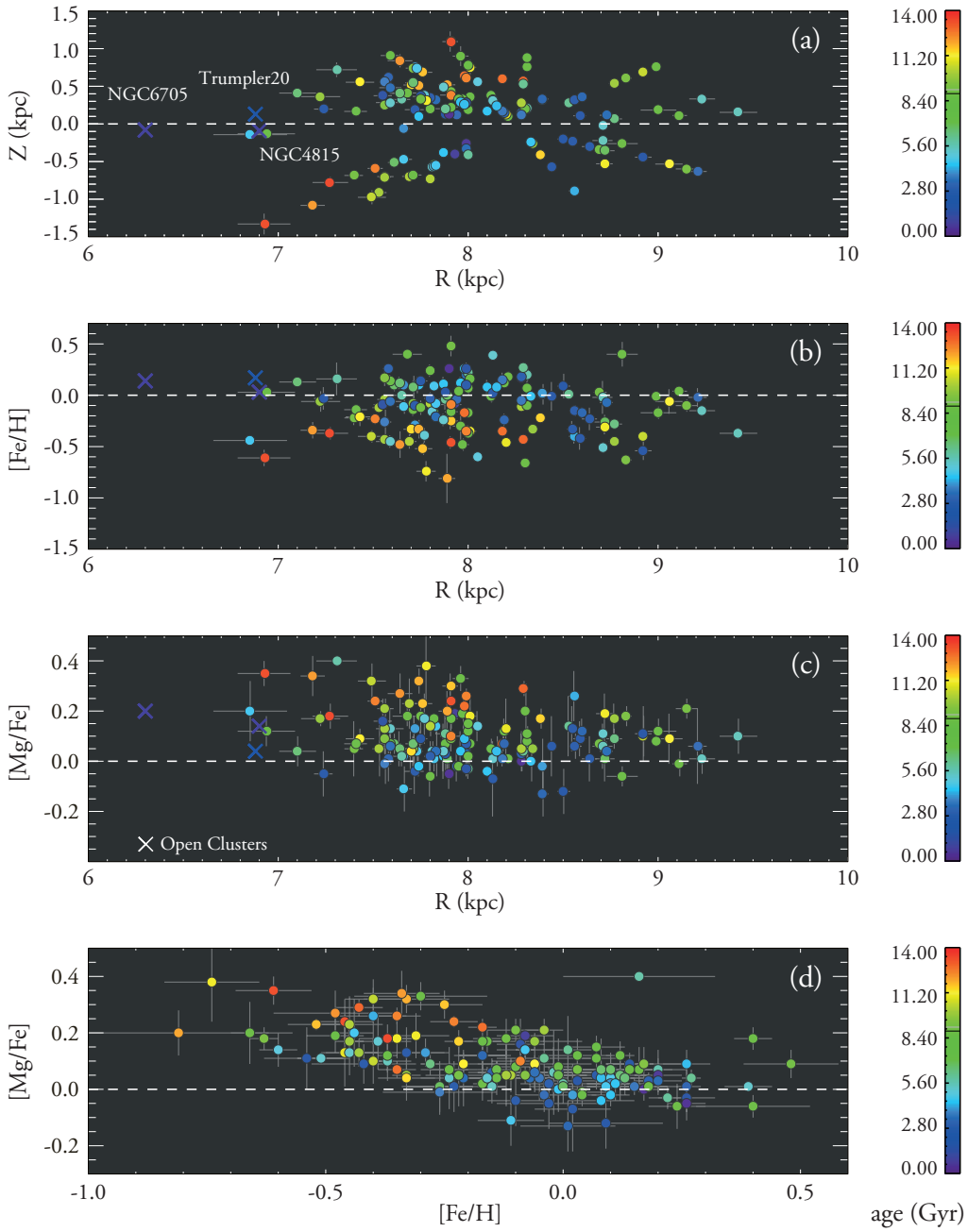

Figure 1.2: The first panel shows Galactic vertical height versus Galactic Radius in kpc. The second and third panel depicts the Radial Metallicity Gradient for [Fe/H] and [Mg/Fe] respectively. The fourth and final panel plots [Mg/Fe] versus [Fe/H]. The colour scale for all subfigures is stellar age in Gyrs.

The RMG above allows us to explore what is known as Radial Migration which is prominent in the "Inside-Out" formation of the disk. Orbits of stars are affected by the spiral arms and the bar of the Milky Way.

This displacement of stars from their birth radii can occur due to the exchange of angular momentum, which can be produced by different processes (Cheng et al. 2012a). For example, stars interact with the transient spiral structure, this occurs due to resonant scattering with the spiral arms. The star is located at the co-rotation radius which causes it to migrate inwards or outwards while keeping a circular orbit (Sellwood & Binney 2002). Another way is through interaction of the Milky Way disc with in-falling satellites (Quillen et al. 2009; Bird et al. 2012). Analysis of Gaia spectroscopy suggests that the inner Halo of the Milky Way originated from another Galaxy (Helmi et al. 2018). Radial Migration can provide an insight into the merger history of the Milky Way. Helmi et al. (2018) reports an analysis of the kinematics, chemistry, age and spatial distribution of stars that are mainly linked to two major Galactic components: the thick disc and the stellar halo. They demonstrated that the inner halo is dominated by debris from an object that is referred as Gaia–Enceladus. Mergers have been shown to be effective at mixing the outer disc via gravitational perturbing.

Also, an overlap of the dynamical resonances corresponding to the bar and spiral structure can lead to this phenomenon. Minchev & Famaey (2010) and Minchev et al. (2011) demonstrated that a strong exchange of angular momentum occurs when a stellar disc is perturbed by a central bar and SS simultaneously, which is shown to be very efficient and forms a bimodal distribution, with two local maxima close to the corotation and outer Lindblad resonance of the bar, regardless of the pattern speed of the spiral. Due to dual resonance, stars in the simulations successfully migrate.

Therefore, due to this process stars' galactocentric distance changes which implies that they have been born not where we observe them today. This is important for us as it can explain the shape of the RMG, specifically how flat it is at larger scale heights. Radial migration washes out the gradients by mixing the populations Cheng et al. (2012a).

Ages can be derived using stellar structure models and asteroseismology, determination of chemical composition requires stellar atmospheric models combined with spectroscopy. Stellar densities and kinematics are measured with observations from large stellar surveys such as Gaia. Kinematics allow

you to calculate the orbital motion, obtaining the orbital motion of the stars means that we can predict their migration over time, since we know the ages, we can so to speak rewind the clock to when they were born and therefore show where they were born. Martínez-Barbosa et al. (2014) attempted to determine the birth radius of the Sun by integrating the orbit backward in time using an analytical model of the Galaxy which includes the contribution of spiral arms and a central bar. This could be applied to other stellar populations. Thus allowing to directly simulate Radial Migration.

1.3 Age-Metallicity relation

Decomposition of the Milky Way's disc based on stellar ages and chemical composition provides a direct connection to the history of the disc and helps constrain chemical evolution models. Stars in the disc display very large range of ages and chemical abundances, spanning the range of $\sim$ 10 gyr and 3 dex in [Fe/H] (Ruchti et al. 2011). Besides, the velocities and orbits of stars in the disc preserve some memory of the perturbations caused by the transient spiral arms, the bar, and mergers with satellite galaxies (Schönrich & Binney 2009a,c; Minchev et al. 2013; Laporte et al. 2018). This leads, in particular to radial migration, heating, and vertical excursions of stars away from the disc (Laporte et al. 2019b).

Therefore, the formation history of the disc gives us an opportunity to constrain the cosmological model Lineweaver (1999). By calculating the different proportions of matter, dark matter and dark energy within the Galaxy from observations of the Galactic rotation curve as well as stellar density surveys such as Gaia, we can pin point which cosmological model that needs to be used in order for a disc to develop with these proportions at its current age. Calculating Dark Matter density from the Rotation Curve has been done in many studies, most recently by Sofue (2020). This could be plausible because formation of the Galactic disc occurs at a time where the models significantly diverge as you can see in Fig. 1.3.

Bergemann et al. (2014) provides an insight to the relationship between age and metallicity (hereafter, the AMR - Age Metallicity Relationship) and α enhancement of FGK stars in the Galactic disk. By analysing high resolution UVES spectra from Gaia-ESO they were able to find that an observed age-metallicity relation exists and splits between young and old stars ($\approx$ 8 Gyrs). Their results depict an age-metallicity plot for the Milky way disk, Fig. 1.5

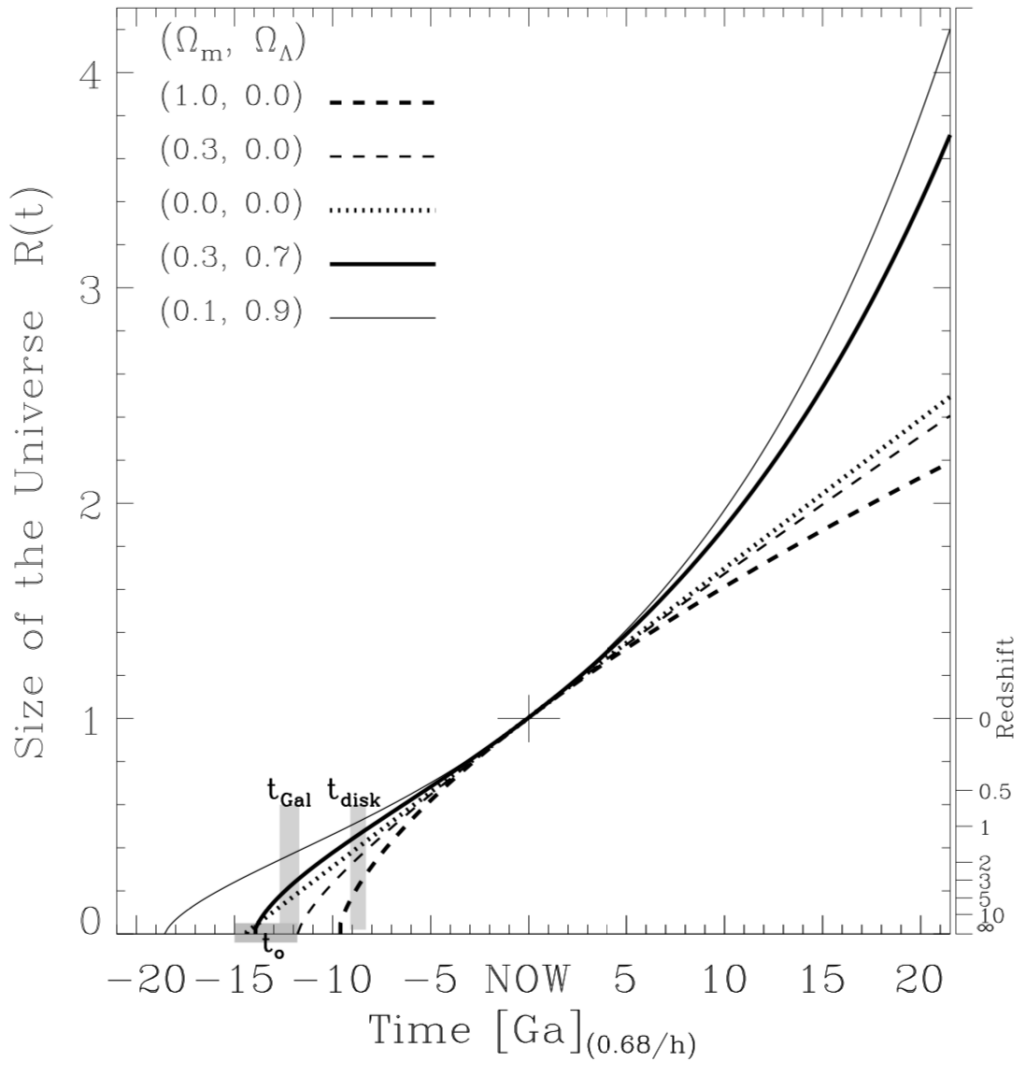

Figure 1.3: Size of the universe in units of the scale factor R(t), as a function of time. There are five cosmological models ranging in Ω_m and Ω_Λ values. Redshift can be quantified on the right axis. Depicted are two epochs representing the origin of the Universe (t_0), the Galaxy (t_{Gal}), and the Galactic disc (t_{disk}), with the uncertainties shaded in grey.

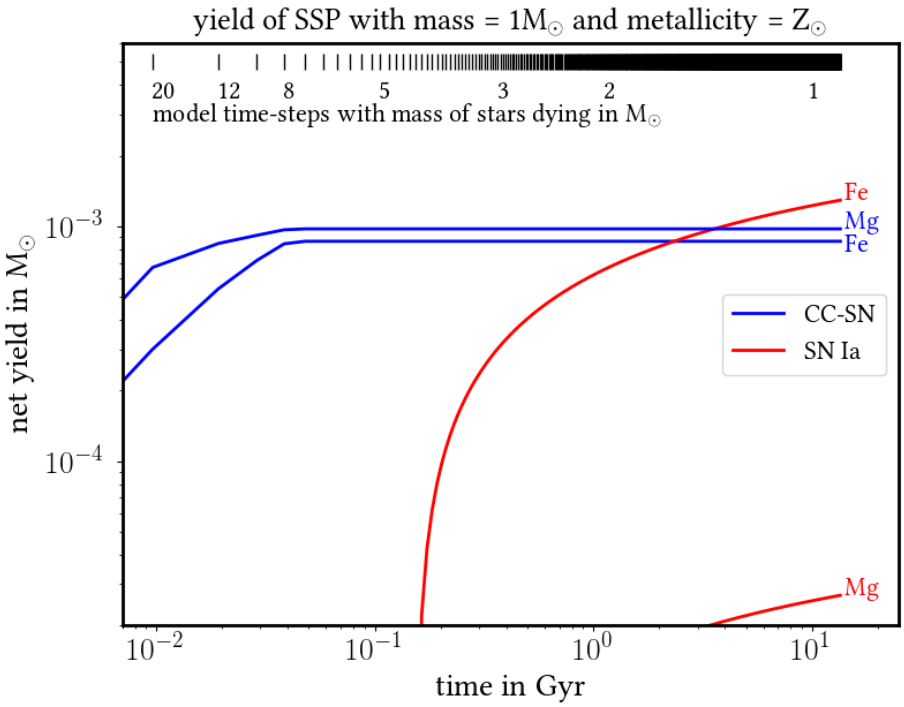

Figure 1.4: Net abundance distribution of the interstellar medium in M⊙ integrated over time in Gyrs. These simulations are made using the Chemby framework developed by Rybizki et al. (2017). Blue solid line represents Fe and Mg abundances from Core-Collapse Supernovae populations, red solid line represents Fe and Mg abundances from Type 1a Supernovae populations.

shows trends which have been demonstrated in earlier observational studies (Edvardsson et al. 1993; Rocha-Pinto et al. 2000) of the disk. Between 0 and 8 Gyrs, the trend is on average flat where the scatter in metallicity spans approximately 1 dex. Beyond 8 Gyrs, there is a decline in [Fe/H] suggesting the older the star, the more metal poor they are. Another critical parameter for understanding the evolution of the chemical enrichment is the ratio of the abundance of the alpha-element Mg to Fe (i.e. [Mg/Fe]), this is a very important astrophysical quantity, as it represents a chemical clock sensitive to the enrichment timescales by SN Ia and SN II (Chiappini et al. 1999). Their findings suggest that [Mg/Fe] rich stars are on average much older than [Mg/Fe] poor stars. This signifies the prevalence of SN II - outcomes of massive star evolution - in the chemical enrichment during the earliest phases of the Galaxy Fig. 1.4.

Notwithstanding many recent efforts to constrain the AMR in the galactic disc (Bensby et al. 2014; Bovy et al. 2016; Mackereth et al. 2017), the problem

still remains open. One of the critical aspects of these measurements is the selection function (Nandakumar et al. 2017): that is, owing to the way an astronomical facility observes the sky, one may preferentially observe stars with some specific characteristics (metallicity, distance, age in different directions on sky. This has to be carefully accounted for in the analyses. Also, the quality of stellar ages and metallicites has not been sufficient, so far, to provide a robust constrain on the astrophysical dispersion of ages at a given metallicity, depending on the Galactocentric radius and distance from the plane. Recent attempts have provided interesting constraints on the radial behaviour of the [Mg/Fe] ratio across the disc (Hayden et al. (2015) based on APOGEE, Lian et al. (2020); Wheeler et al. (2020) based on LAMOST; Lin et al. (2020) based on GALAH). However, so far these efforts have been limited by the lack of robust ages and phase-space, in order to clearly separate the in-situ and ex-situ stellar populations (especially in the context of the debate on the ex-situ formation of the galactic thick disk, e.g. Brook et al. (2005); Bournaud et al. (2009); Vera-Ciro et al. (2016); Miranda et al. (2016), as well as to isolate the contribution from the halo at high altitudes and bulge in the inner regions of the disk.

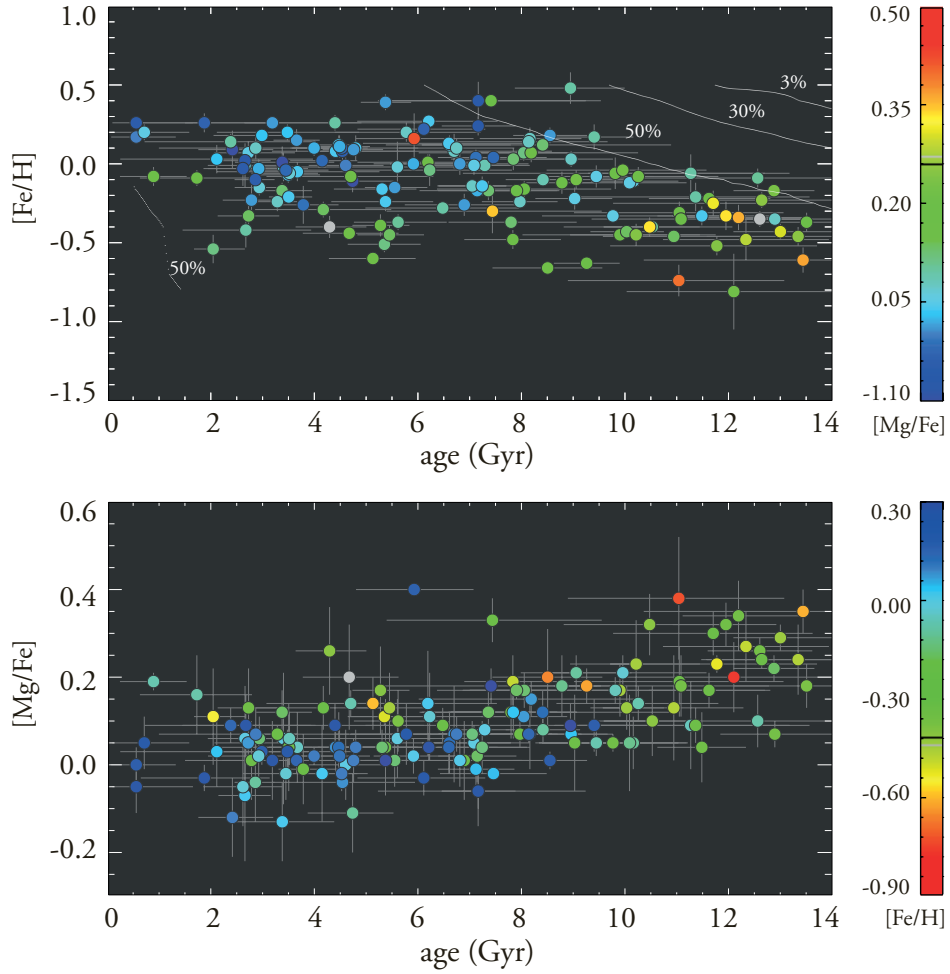

Figure 1.5: *Top*: Age-metallicity plot for the Milk Way disk. Colour scale represents [Mg/Fe] value and the contours indicate the relative sample completeness. *Bottom*: Distribution of stars in [Mg/Fe] versus age plane, the colour scale is in [Fe/H]. Ages are in Gyrs.

1.4 Overview

In this work, I attempt to develop a self-consistent numerical tool that is necessary to attack several scientific aspects, from updating the AMR to serving as the work horse for parameter estimation for large stellar survey space missions such as PLATO. We start with a decisive sample of stars with robust and homogeneously determined abundances of different chemical elements, ages, kinematics, temperatures and surface gravities. We end with a numerical code that will be used to provide fundamental stellar parameters of stars within all main galactic components: from the bulge, through the inner disk, solar neighbourhood, outer disk, old disc (usually referred to as the thick disk, e.g. Recio-Blanco et al. (2014); Sharma et al. (2019); Palla et al. (2020), and the halo.

We use the completed large medium-resolution spectroscopic survey Gaia-ESO combined with Gaia astrometry, photometry, and asteroseismology surveys (CoRoT and Kepler). These give us a unique opportunity to provide detailed measurements of radial and vertical evolution of the abundances of Fe, Mg, and other elements across the entire Galaxy. This allows us to use data with unprecedented multi-dimensionality and precision compared to previous studies.

The most robust way to measure all these astrophysical tags is to combine all observational information available for stars in a single comprehensive framework, that justifies the choice of the Bayesian framework - the heart of the work described in this study. The Bayesian technique is not new (Pont & Eyer 2004; Serenelli et al. 2013; Schönrich & Bergemann 2014) and has been applied to stellar physics before. Each study derived different stellar parameters using varying observational sources e.g. Pont & Eyer (2004) created a Bayesian framework which calculated ages from isochrone fitting (which involves comparing Temperature, Luminosity, [Fe/H] to those from the isochrone). Serenelli et al. (2013) used a Bayesian scheme to derive Masses, Ages, and distances with GARSTEC stellar tracks, this required accurate effective temperatures, surface gravity and [Fe/H] obtained by independent means. Schönrich & Bergemann (2014) developed a Bayesian framework which at its core inspired the creation of SAPP with promises of observation input flexibility and being the first generalised Bayesian approach for stellar parameter determination.

Using the Bayesian framework in essence is a combination of several proba-

bility distribution functions in a multi-dimensional parameter space that can be combined/explored depending on the available observational information of the star and the desired physical quantities. This style of parameter determination allows one to take into account all the different uncertainties that different observational methods have.

Photometry is limited by reddening, spectra contain lots of diagnostic features in a typical stellar spectrum, but each line suffers from its own systematics (imperfect physical models, specific telescopes). Parallax is not always one-to-one with distance. Usually manual intervention is required where lines are re-weighted, photometry is re-calibrated, ad-hoc "corrections" are applied or simply data is removed. With a Bayesian scheme, the different observational inputs succeed the most with different parameters, therefore combining the information with robust uncertainties maximises the accuracy of all the stellar parameters. The study that I propose will benefit from this scheme for the ability to combine all the observational information self-consistently.

The thesis is organised as follows. In Chapter 2, I present work of the first 2 years of my PhD culminated into a publication Gent et al. (2022). I introduce the motivation for writing a pipeline to determine stellar parameters, described the methodology, present observation data I used to validate the pipeline, and describe the results and performance of SAPP. In Chapter 3, I present the application of the SAPP pipeline on the Gaia-ESO survey, outside of the PLATO space mission. This is the first full scale test of the pipeline on a stellar survey, whereby I use the results to perform a chemo-dynamical analysis of the Milky Way's disc. This required validating the stellar parameters and robustly determining ages, as this data was beyond the benchmark stars analysed in Gent et al. (2022). This chapter is based on a paper that is currently in its second referee process, soon to be submitted. Each chapter contains an abstract for the study, and overview. Chapter 4 summarises the main highlights, and leads towards future perspectives of the application of SAPP, further describing its current use in other co-authored studies.

Chapter 2

The SAPP pipeline for the determination of stellar abundances and atmospheric parameters of stars in the core program of the PLATO mission

We introduce the SAPP (Stellar Abundances and atmospheric Parameters Pipeline), the prototype of the code that will be used to determine parameters of stars observed within the core program of the PLATO space mission[1]. The pipeline is based on the Bayesian inference and provides effective temperature, surface gravity, metallicity, chemical abundances, and luminosity. The code in its more general version can have a much wider range of application. It can also provide masses, ages, and radii of stars and can be used for stars of stellar types not targeted by the PLATO core program, such as red giants. We validate the code on a set of 27 benchmark stars that includes 19 FGK-type dwarfs, 6 GK-type sub-giants, and 2 red giants. Our results suggest that combining various observables is the optimal approach, as it allows to break degeneracies between different parameters and yields more accurate values of stellar parameters and more realistic uncertainties. For the PLATO core sample, we obtain a typical uncertainty of $27\,(\mathrm{syst.}) \pm 37$ (stat.) K for T_{eff}, 0.00 ± 0.01 dex for $\log g$, 0.02 ± 0.02 dex for metallicity [Fe/H], -0.01 ± 0.03 $\mathrm{R}_{\odot}$ for radii, -0.01 ± 0.05 $\mathrm{M}_{\odot}$ for stellar masses, and -0.14 ± 0.63 Gyrs for ages. We also show that the best results are obtained by combining the ν_{max} scaling relation and stellar spectra. This resolves the notorious problem of degeneracies, which is particularly important for F-type stars.

[1]This chapter has been adopted from my first refereed published paper: https://ui.adsabs.harvard.edu/abs/2022A%26A...658A.147G/abstract

2.1 Introduction

The past decade has seen revolutionary developments in astronomical surveys and large-scale observational programs aimed at assembling high-quality data for millions of stars in our Galaxy. Many of the ongoing efforts are motivated by using stars as tracers of Galaxy structure and evolution (e.g., *Hipparcos*: Perryman et al. 1997a, 2MASS: Skrutskie et al. 2006, SDSS/SEGUE: Yanny et al. 2009, GCS: Nordström et al. 2004a, Gaia-ESO: Gilmore et al. 2012b; Randich et al. 2013, LAMOST: Cui et al. 2012, RAVE: Steinmetz et al. 2006, Gaia: Gaia Collaboration et al. 2016, APOGEE: Majewski et al. 2017, GALAH: De Silva et al. 2015). With the advent of exoplanet science, the role of stars as exoplanet hosts is becoming increasingly important. Space-based missions - CoRoT, Kepler, and TESS - are discovering new exoplanets at an astonishing rate (e.g. Borucki et al. 2010; Buchhave et al. 2014; Ricker et al. 2015), but also yield precise data for the studies of stellar interiors with asteroseismology techniques (e.g. Christensen-Dalsgaard 2002; Huber et al. 2013; Serenelli et al. 2017). Future facilities, such as PLATO (Rauer et al. 2014), are opening entirely new perspectives for studies of exoplanets in different environments and for studies of stars at the level of details that have so far been only available for our Sun.

In this work, we introduce the SAPP pipeline[2] that will be used for the determination of atmospheric parameters of stars observed within the core program of the PLATO space mission (Montalto et al. 2021). The code will provide stellar effective temperature ($T_{\rm eff}$), metallicity ([Fe/H]), surface gravity ($\log g$), radial velocities, and detailed chemical composition, among other parameters. Our ambitious goal is to reach uncertainties as low as 1% on $T_{\rm eff}$ and [Fe/H], for instance, in order to match the high spectral data quality provided by upcoming ground-based facilities, such as WEAVE and 4MOST. The SAPP is written in Python and the source code is public and available for use[3].

Our approach to the analysis of our targets is somewhat different from other available pipelines and codes (e.g., SME: Valenti & Piskunov 1996; Piskunov & Valenti 2017, The Cannon: Ness et al. 2015, The Payne: Ting et al. 2016, Rix et al. 2016, Ting et al. 2019, MATISSE: Recio-Blanco et al. 2006, CNN StarNet: Bialek et al. 2020), although our analysis shares many of the elements with these software units. It is beyond the scope of this paper to pro-

[2] We stress that the detailed approach to the analysis of PLATO targets will evolve.
[3] https://github.com/mg477/SAPP

vide a detailed comparison of our code with the other programs, as ultimately the design of a computer program follows the needs and objectives of a given research project, and this sets the conceptual and numerical basis of a code. In our case, motivated by the need to provide accurate and precise astrophysical parameters for several 10^5 (and more) stars to enable their exploitation in studies of exoplanets, we have chosen a Bayesian inference method as the basis of the code (see, e.g. Jofré et al. 2019, for a review of methods and models). The idea of using Bayesian techniques is not new, and it has been already presented in a number of studies (e.g. Pont & Eyer 2004; Jørgensen & Lindegren 2005; Serenelli et al. 2013; Schönrich & Bergemann 2014; Bailer-Jones et al. 2018; McMillan et al. 2018; del Burgo & Allende Prieto 2018; Steinmetz et al. 2020). In this work, we closely follow the methodology outlined in Schönrich & Bergemann (2014) and combine various sources of observational information, including electromagnetic spectra, parallaxes, photometry, and seismic constrains to determine astrophysical parameters of stars. It has been already shown (e.g. Pont & Eyer 2004; Jørgensen & Lindegren 2005; Gruberbauer et al. 2012; Bazot et al. 2012) that the analysis of fundamental parameters of stars, masses and metallicities, especially benefits from the Bayesian approach. Therefore, in order to take the full advantage of the Bayesian formalism, we also include stellar evolution models that give us the ability to determine masses, luminosities, radii, and ages of stars in a single consistent framework taking into account the correlations between all relevant parameters.

The chapter is organised as follows. Section 3.2 gives an overview of the observed sample of stars that are used to validate the approach developed in this work. In Sect. 2.3 we outline the basic concepts behind the numerical part of the code and review the input parameters and input models, including stellar structure models, stellar atmospheres, and the grids of stellar spectra. In Sect. 3.7 we present the results of the analysis of the benchmark stars, as well as clusters and in Sect. 2.5 we describe the operation of SAPP briefly in the context of the PLATO space mission (Rauer et al. 2014). We close the paper with the discussion of forthcoming improvements to the pipeline in Sect. 2.6 and draw conclusions in Sect. 2.7.

Table 2.1: Reference parameter sample of benchmark stars

Star ID	HD	V mag	Ks mag	Parallax mas	$T_{\rm eff}$ K	log g dex	[Fe/H] dex	Mass $M_\odot$	Age Gyrs	Radius $R_\odot$	Luminosity $L_\odot$
Gaia-ESO											
18 Sco	HD 146233	5.50	4.19 ± 0.29	70.74 ± 0.06	5810 ± 80	4.44 ± 0.03	0.03 ± 0.03	1.02 ± 0.06	2.90 ± 0.50	1.01 ± 0.01	1.05 ± 0.06
α Cen A	HD 128620	0.01	-1.52 $\pm$ 0.05*a*	743.00 $\pm$ 1.30 (3)	5792 ± 16	4.31 ± 0.01	0.26 ± 0.08	1.11 ± 0.00	5.26 ± 0.95	1.22 ± 0.01	1.52 ± 0.01
α Cen B	HD 128621	1.33	-0.64 $\pm$ 0.05*a*	743.00 $\pm$ 1.30 (3)	5231 ± 20	4.53 ± 0.03	0.22 ± 0.10	0.94 ± 0.00	5.26 ± 0.95	0.86 ± 0.00	0.50 ± 0.01
β Hyi	HD 2151	2.70	1.3 $\pm$ 0.04*b*	133.72 $\pm$ 0.27 (1)	5873 ± 45	3.98 ± 0.02	-0.04 ± 0.06	1.14 ± 0.05	6.40 ± 1.40	1.89 ± 0.03	3.52 ± 0.09
β Vir	HD 102870	3.60	2.28 $\pm$ 0.01*c*	90.89 $\pm$ 0.19 (1)	6083 ± 41	4.10 ± 0.02	0.24 ± 0.07	1.34 ± 0.04	4.00 ± 1.00	1.68 ± 0.01	3.58 ± 0.04
δ Eri	HD 23249	3.54	1.62 ± 0.29	110.03 $\pm$ 0.19 (1)	5022 ± 34	3.76 ± 0.02	0.06 ± 0.05	1.33 ± 0.07	6.19	2.35 ± 0.01	2.94 ± 0.00
η Boo	HD 121370	2.68	1.31 $\pm$ 0.02*d*	87.75 $\pm$ 1.24 (2)	6099 ± 28	3.79 ± 0.02	0.32 ± 0.08	1.64 ± 0.07	2.67 ± 0.10	2.67 ± 0.02	8.97 ± 0.12
CoRoT 20	HD 49933	5.76	4.72 ± 0.02	33.53 ± 0.04	6635 ± 91	4.20 ± 0.03	-0.41 ± 0.08	1.28 ± 0.01	1.83 ± 0.10	1.46 ± 0.01	3.52 ± 0.04
Procyon	HD 61421	0.37	-0.70 $\pm$ 0.01*e*	284.56 $\pm$ 1.26 (2)	6554 ± 84	4.00 ± 0.02	0.01 ± 0.08	1.50 ± 0.07	1.87 ± 0.13	2.05 ± 0.03	6.90 ± 0.35
Sun	...	...	...	...	5777 ± 1	4.44 ± 0.01	0.03 ± 0.05	1.00 ± 0.00	4.56 ± 0.00	1.00 ± 0.00	1.00 ± 0.00
Kepler Legacy											
KIC 10162436	HD 188819	8.66	7.36 ± 0.02	7.30 ± 0.01	6259 ± 49	3.98 ± 0.02	-0.07 ± 0.02	1.41 ± 0.05	2.57 ± 0.43	2.01 ± 0.03	...
KIC 10644253	BD+47 2683	9.26	7.87 ± 0.03	10.35 ± 0.01	6126 ± 27	4.40 ± 0.02	0.13 ± 0.02	1.16 ± 0.02	1.37 ± 0.72	1.12 ± 0.00	1.45 ± 0.09
16 Cyg A	HD 186408	5.95	4.43 ± 0.02	47.32 ± 0.02	5839 ± 42	4.29 ± 0.02	0.09 ± 0.01	1.07 ± 0.01	7.36 ± 0.31	1.22 ± 0.01	1.52 ± 0.05
16 Cyg B	HD 186427	6.20	4.65 ± 0.02	47.33 ± 0.02	5809 ± 39	4.36 ± 0.02	0.06 ± 0.01	1.04 ± 0.05	7.05 ± 0.63	1.11 ± 0.02	1.21 ± 0.11
KIC 12258514	HD 183298	8.16	6.76 ± 0.02	12.25 ± 0.01	6046 ± 24	4.12 ± 0.02	0.03 ± 0.02	1.25 ± 0.02	5.50 ± 0.40	1.59 ± 0.02	2.63 ± 0.12
KIC 3427720	BD+38 3428	9.22	7.83 ± 0.02	10.74 ± 0.01	6092 ± 24	4.39 ± 0.02	-0.02 ± 0.02	1.10 ± 0.02	2.97 ± 0.78	1.12 ± 0.01	1.37 ± 0.08
KIC 6106415	HD 177153	7.21	5.83 ± 0.02	24.16 ± 0.01	6090 ± 17	4.30 ± 0.02	-0.04 ± 0.01	1.04 ± 0.02	4.55 ± 0.28	1.21 ± 0.01	1.61 ± 0.09
KIC 6225718	HD 187637	7.53	6.28 ± 0.02	19.03 ± 0.02	6308 ± 33	4.32 ± 0.02	-0.11 ± 0.01	1.17 ± 0.04	2.23 ± 0.20	1.23 ± 0.02	2.08 ± 0.11
KIC 7940546	HD 175226	7.42	6.17 ± 0.02	12.96 ± 0.02	6319 ± 28	4.00 ± 0.02	-0.10 ± 0.01	1.51 ± 0.09	2.42 ± 0.17	1.97 ± 0.04	5.69 ± 0.35
KIC 9139151	BD+45 2796	9.29	7.95 ± 0.02	9.76 ± 0.01	6136 ± 27	4.38 ± 0.02	0.10 ± 0.02	1.18 ± 0.03	1.49 ± 0.68	1.16 ± 0.01	1.81 ± 0.11
Other											
ν Ind	HD 211998	5.29	3.54 ± 0.26	35.13 ± 0.06	5320 ± 24	3.46 ± 0.02	-1.43 ± 0.06	0.85 ± 0.05	11.00 ± 1.06	...	...

The reference parameter sample of well-studied FGK stars used for the tests reported in this work. The errors of V-mag are 0.01 mag. KIC 12069424 is 16 Cyg A and KIC 12069449 is 16 Cyg B. See Sect. 2.2.2 for a more detailed description. vsini values are not tabulated here however they range from 1.1 kms^{-1} (α Cen B) to 12.7 kms^{-1} (η Boo). The Ks magnitudes are taken from Cutri et al. (2003), except for the stars marked in the table, for which they were calculated from K magnitudes taken from the following references, transformed to Ks using Eq. (A1) from Carpenter (2001): *a*Engels et al. (1981), *b*Glass (1974); Engels et al. (1981); Carter (1990), *c*Johnson et al. (1966, 1968); Aumann & Probst (1991), *d*Johnson et al. (1966); Johnson (1967); Blackwell et al. (1979); Ghosh et al. (1984); Selby et al. (1988); Arribas & Martinez Roger (1989), *e*Low & Johnson (1964); Johnson et al. (1966); Glass (1974); Veeder et al. (1978); Engels et al. (1981); Tapia et al. (1984); Roth et al. (1984); Evans et al. (1987); Alonso et al. (1994). The photo-geometric distances of the stars are taken from Bailer-Jones et al. (2021), these use Gaia eDR3 parallaxes which are not marked in the table (Gaia Collaboration 2020). The stars that are marked, the distances were calculated using the formula d = 1/π and thus parallaxes shown are from, 1Gaia Collaboration (2020), 2van Leeuwen (2007), 3Pourbaix & Boffin (2016). Mean and standard deviation are given in case of more than one reference.

All parameters that have an uncertainty of 0.00 are accurate to less than 0.00 of the given unit.

The current solar effective temperature is 5772 $\pm$ 1 K (Prša et al. 2016), the use of the older value of 5777 K within this study is justified by the SAPP's systematic uncertainties which are more than 10 K.

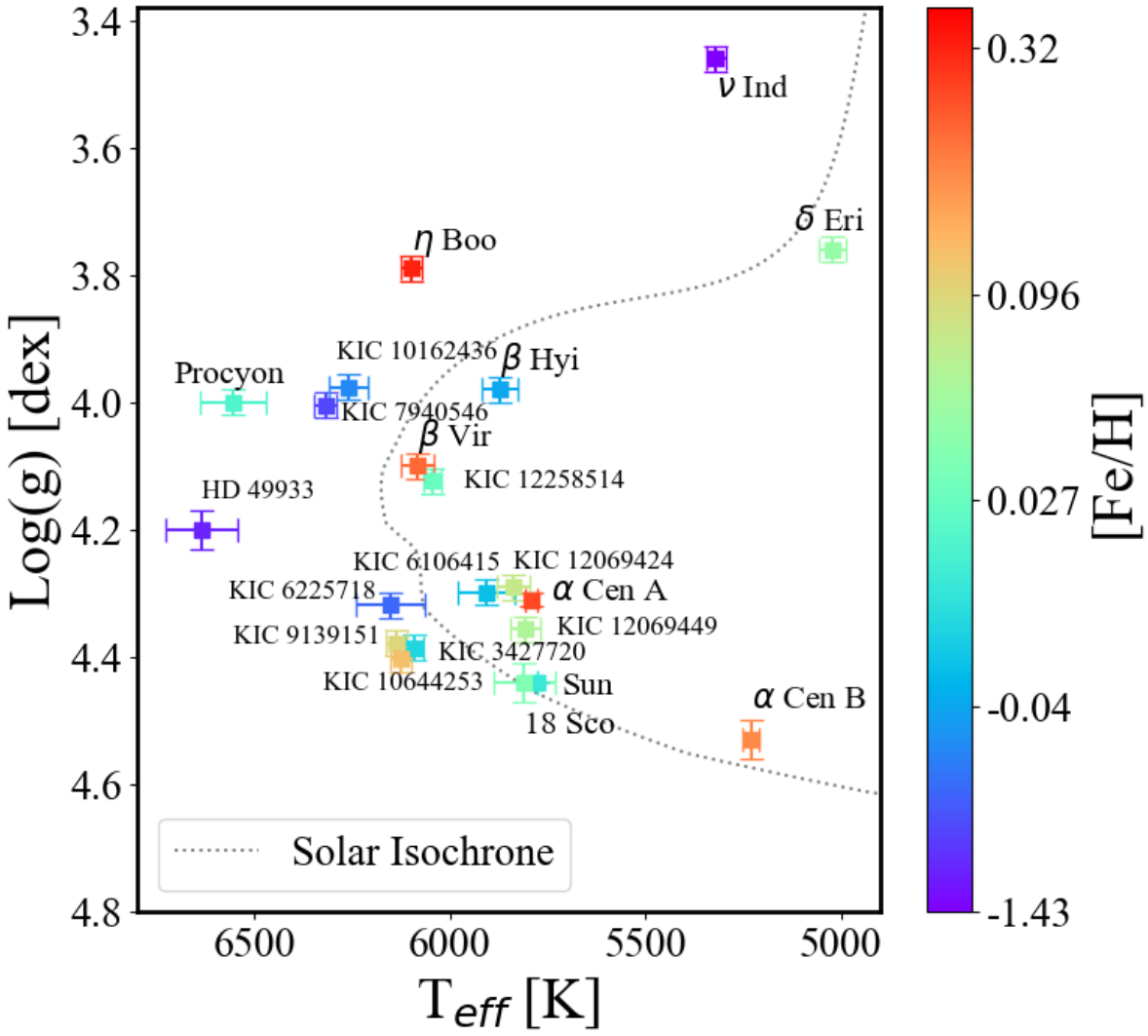

Figure 2.1: $T_{\rm eff}$-log g diagram of the benchmark targets. Colour scale represents metallicity (blue end is metal poor and red end is just above solar metallicity). Each star is plotted with its reference values (Table 2.1) on top of a solar isochrone.

2.2 Observations

2.2.1 Observed data

The core PLATO sample focuses on main-sequence stars and sub-giants (Montalto et al. 2021). Therefore, we first focus on these types of stars, but owing to the versatility of the code and input physics, we also present in Sect. 2.4.6 the performance of the code on spectra of red giants in the Galactic field and

in stellar clusters.

Our core validation stellar sample includes Gaia benchmark stars (Heiter et al. 2015), Kepler Legacy stars (Silva Aguirre et al. 2017; Nissen et al. 2017), and a very metal-poor star ν ind (Chaplin et al. 2020). These stars are shown in the $T_{\rm eff} - \log g$ plane in Fig 2.1, and they provide a representative coverage of the current PIC (Montalto et al. 2021). The stars cover a broad range in effective temperatures, from 5022 K (δ Eri) to 6635 K (HD 49933), and surface gravities from $\log g = 3.46$ (ν Ind) to $\log g = 4.53$ dex (α Cen B). One of the stars in the sample (η Boo) is a relatively fast rotator (for FGK-type stars) with a projected equatorial rotational velocity $v_{\sin \rm i} = 12.7$ kms^{-1}. Some of the stars have a super-solar metallicity, in excess of +0.2 dex (η Boo, α Cen A,B system), whereas the most metal-poor star in the sample is ν Ind with [Fe/H] $= -1.43$ dex (Chaplin et al. 2020).

The spectra of the benchmark stars are taken from the ESO public archive. For the majority of stars, spectra obtained with the high-resolution UVES spectrograph mounted on VLT are available. For the Kepler stars, reduced combined spectra taken with HARPS-N facility were kindly provided by P. E. Nissen (priv.comm.). The UVES spectra (4800 to 6800) have a resolving power of $\lambda/\delta\lambda \approx 47\,000$ (Dekker et al. 2000) and the HARPS data of 115 000 (Mayor et al. 2003).The signal-to-noise ratio (S/N) of the UVES and HARPS spectra is in the range from 200 to over 1 000. The spectra are all pre-processed (described in section 2.3.5) by the SAPP using different procedures developed, this includes continuum normalisation, radial velocity correction and contaminant treatment. Then we degrade the resolving power of the spectra to $R = 20\,000$ and reduce the wavelength coverage to 5300 - 5600 Å in the optical spectral window. This is done to ensure that our tests are as predictive as possible: spectra with such characteristics represent a plausible scenario, in which for the vast majority of PLATO targets only spectra observed with medium-resolution (R $\approx$ 20 000) facilities, such as 4MOST, WEAVE, and APOGEE, will be available.

The observed photometry for these stars was extracted from the Gaia EDR3 catalogue Gaia Collaboration et al. (2016, 2018); Gaia Collaboration (2020), which we supplemented with 2MASS magnitudes (JHK$_s$) and Johnson-Cousins photometric data, where available. For most stars in the sample, we used the photo-geometric distances from Bailer-Jones et al. (2021) catalogue. If they were not available (see Table 2.1), then Gaia parallaxes π are converted into

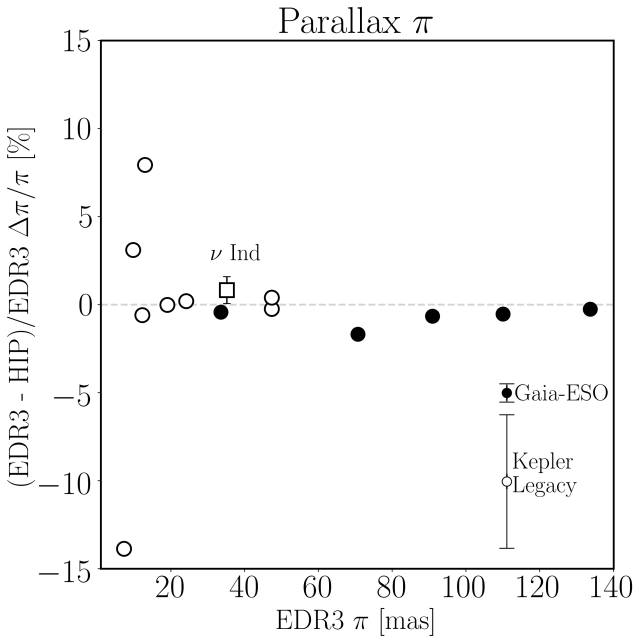

Figure 2.2: Percentage difference between Gaia EDR3 parallax and Hipparcos parallax (van Leeuwen 2007) with respect to Gaia EDR3 in mas. The error represents the uncertainty of EDR3 parallaxes and Hipparcos parallaxes propagated through the percentage difference. The open circles represent the Kepler legacy stars, the solid black circles represent Gaia-ESO stars, and the single open square represents our metal poor star ν Ind. The average uncertainty for the Kepler Legacy and Gaia-ESO stars are in the bottom right corner.

distances via $d\ [\mathrm{pc}] = 1/\pi$. This is a suitable approximation in this work, because the benchmark stars are all nearby targets, with the most distant system being KIC 10162436 at around 138 pc. If Gaia parallaxes were not available, then values from the Hipparcos catalogue were supplemented (Perryman et al. 1997b; van Leeuwen 2007). The largest percentage difference between distances from Bailer-Jones et al. (2021) and using the inverse parallax values are 0.02% for Gaia EDR3 and 0.39 % for Hipparcos, respectively. The comparison between EDR3 and Hipparcos parallaxes can be seen in Fig. 2.2, where it can be seen that the maximum propagated percentage difference for Kepler Legacy stars are $\sim 5\%$ and for Gaia-ESO less than 0.5%.

The observed magnitudes were corrected for interstellar extinction using the `Stilism` tool (Capitanio et al. 2017). The tool maps the local Interstellar Matter (ISM) based on measurements of starlight absorption by dust (reddening effects) or gaseous species (absorption lines or bands). It provides line-of-sight reddening interpolated on a given distance, Galactic longitude, and latitude with associated uncertainties. Figure 2.3 depicts the line-of-sight red-

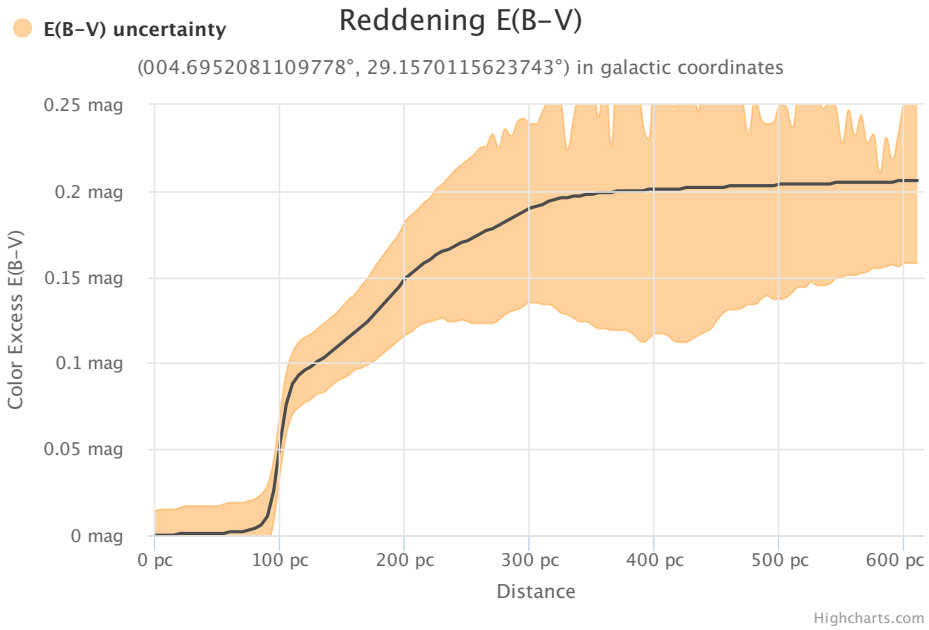

Figure 2.3: Figure extracted with Galactic coordinates of 18 Sco: l = 004.695, b = +29.157. Reddening value E(B-V) in magnitude versus distance in parsecs. The black solid line is E(B-V) as a function of distance, the yellow shaded region represents the E(B-V) uncertainty.

dening value (black solid line) with uncertainty (yellow shaded region) versus the distance in parsec. This figure was created using the *Stilism* tool for the Galactic coordinates for the star 18 Sco. For the benchmark stars, the reddening is small (E(B-V) $\lesssim$ 0.015 mag) and is implemented via the extinction correction (see equation 2.9).

2.2.2 Stellar parameters of the benchmark stars

Stellar parameters for our benchmark stars were obtained from several literature sources, the priority being given to Jofré et al. (2018), because they provide a comprehensive homogeneous analysis of all classical stellar parameters, including metallicity and detailed chemical abundances, derived with constraints from independent data. This study is based on the analysis presented by Jofré et al. (2014) and Heiter et al. (2015). All parameters for ν Ind were adopted from Chaplin et al. (2020).

In short, the determination of parameters for the Gaia benchmark stars is as follows. The $T_{\rm eff}$ values rely on interferometric angular diameters measured with CHARA and VLTI facilities and bolometric fluxes obtained either via integrating the observed Spectral Energy Distributions (SEDs) or indirectly by converting the photometry into $F_{\rm bol}$ using synthetic calibrations. δ Eri is

the only star, for which we give a preference to the recent accurate $T_{\rm eff}$ and radius values based on the interferometric angular diameter measured with VLTI/PIONEER (Rains et al. 2020). The surface gravities were determined using masses estimated from evolutionary tracks, angular diameters, and Hipparcos parallaxes, which are mostly in excellent agreement with Gaia DR2 and Gaia EDR3 values for the reference sample (see Fig. 2.2). The surface gravities were verified using asteroseismic scaling relations, where possible. Metallicities are model-dependent quantities: here we adopt the Non-Local Thermodynamic Equilibrium (NLTE) estimates. Luminosity measurements are taken from Heiter et al. (2015), whereas masses are adopted from different sources. For δ Eri's mass is taken from Bruntt et al. (2010) with age adopted from Thévenin et al. (2005). α Cen A & B have masses and radii from Kervella et al. (2017) with age from Joyce & Chaboyer (2018). The mass and age of ν Ind are taken from Chaplin et al. (2020), but no luminosity or radius are provided in that study. HD 49933 has mass, age, and radius estimated by Liu et al. (2013). The age and radius sources vary star-by-star, for 18 Sco age Monroe et al. (2013) and radius Bazot et al. (2018), for β Hyi age and radius Brandão et al. (2011), β Vir age Eggenberger & Carrier (2006) and radius Boyajian et al. (2012), η Boo age Carrier et al. (2005) and radius van Belle et al. (2007), Procyon age Liebert et al. (2013) and radius from Kervella et al. (2004).

For the Kepler Legacy sample, stellar parameters were adopted from Nissen et al. (2017), except the 16 Cyg A & B binary, for which the interferometric $T_{\rm eff}$ estimate from White et al. (2013) is given a preference. We do not use ν Ind or the Kepler stars in the analysis of $T_{\rm eff}$ (except 16 Cyg A & B), because their $T_{\rm eff}$ were not determined in the same fundamental way as those of Gaia benchmark stars and large scatter exists between different estimates (e.g. Wu & Li 2017 for KIC 6225718). The interferometric angular diameter (AD) measurements for KIC 6225718 and KIC 6106415 exist, however, the errors of the $T_{\rm eff}$ estimates are unfortunately too large (70 to 90 K) to provide a meaningful constraint on the methods. The estimates of mass (M), radius (R), luminosity (L), and age (τ) for the majority of these stars come from Serenelli et al. (2017) (KIC 10162436, KIC 10644253, KIC 3427720, KIC 9139151) and Creevey et al. (2017) (16 Cyg A & B, KIC 12258514, KIC 6106415, KIC 6225718, KIC 7940546).

2.3 Methods

2.3.1 Bayesian probability approach

The conditional probability of a set of model parameters $\mathbf{X} = \mathrm{X}_1,...,\mathrm{X}_n$ given a set of observations $\mathbf{O} = \mathrm{O}_1,...,\mathrm{O}_m$ is given by Bayes theorem and results from from the combined probability $\mathrm{P}(\mathbf{X},\mathbf{O}) = \mathrm{P}(\mathbf{X}|\mathbf{O})\mathrm{P}(\mathbf{O})$. Hence,

$$P(\mathbf{X}|\mathbf{O}) = \frac{P(\mathbf{X})}{P(\mathbf{O})} P(\mathbf{O}|\mathbf{X}), \tag{2.1}$$

where $\mathrm{P}(\mathbf{X}|\mathbf{O})$ is the posterior probability, that is the conditional probability of the parameter set $\mathbf{X}$ given the set of observables $\mathbf{O}$. $\mathrm{P}(\mathbf{O}|\mathbf{X})$ is the likelihood, i.e. the probability of the observations occurring given the set of parameters $\mathbf{X}$. $\mathrm{P}(\mathbf{X})$ is the prior probability ascribed to a set of predefined parameters. The denominator $\mathrm{P}(\mathbf{O})$ is function only of the observations, and it is not relevant for determination of stellar model parameters, as it acts only as a normalisation factor. Therefore, the expression above can be simplified to

$$P(\mathbf{X}|\mathbf{O}) \propto P(\mathbf{X}) P(O_1, ..., O_m|\mathbf{X}), \tag{2.2}$$

where the posterior $\mathrm{P}(\mathbf{X}|\mathbf{O})$ is a probability distribution function (PDF) on the chosen parameter space. For the remainder of this paper the observational likelihoods are abbreviated by a prime given the set of parameters, i.e. $P'(\mathbf{X})$. The current implementation of SAPP assumes observables are statistically independent, which allows decomposing $P(O_1, ..., O_m|\mathbf{X})$ as,

$$P'(\mathbf{X}) = P(O_1, ..., O_m|\mathbf{X}) = \prod_{j=1}^{m} P(O_j|\mathbf{X}). \tag{2.3}$$

More specifically, based on the observables used in this work,

$$\begin{aligned} P(\mathbf{X}|\mathbf{O}) \propto P(O_{spec}|\mathbf{X}) \cdot P(O_{mag,dist}|\mathbf{X}), \\ \cdot P(O_{seism}|\mathbf{X}) \cdot P_{prior}(\mathbf{X}), \end{aligned} \tag{2.4}$$

where the subscripts refer to a specific observable, j: "spec" for stellar spectra (fluxes against wavelength), "mag" for photometric magnitudes and their products, "seism" for asteroseismic quantities ($\Delta\nu$, $\nu_{\max}$), and "prior" for any priors. Here $\mathrm{P}_{prior}(\mathbf{X})$ is the prior probability distribution, this can represent the initial mass function (IMF), selection function, or any other source of information that further constrains the parameter space. For this study just

the IMF (see Sect. 2.3.9 and the age step size (from model grid points, see Sect. 2.3.8) are used as a prior. All observables are assumed to be normally distributed, i.e.

$$P(O_j|\mathbf{X}) = \prod_k^{N_j} G_j(x - \bar{x}_k, \sigma_k), \tag{2.5}$$

where N_j is the number of parameter points (index running over k) for the given observable j. Therefore,

$$G_j(x - \bar{x}_k, \sigma_k) = \frac{1}{(\sigma_k^{N_j} 2\pi)^{\frac{1}{N_j}}} \exp\left[-\frac{(x-\bar{x}_k)^2}{2\sigma_k^2}\right] \tag{2.6}$$

It is easy to modify the expression for the likelihood to include statistically dependent observables by introducing the use of their correlation matrix. This is usually not necessary, but in this work we explore the influence of covariance in the analysis (see Sect. 2.4.5) and therefore, we also perform additional calculations with equation 2.6 modified to:

$$G_j(x - \bar{x}_k, \sigma_k) = \frac{\exp(-\frac{1}{2}(\mathbf{x} - \bar{\mathbf{x}}_\mathbf{k})^\mathrm{T} \Sigma^{-1} (\mathbf{x} - \bar{\mathbf{x}}_\mathbf{k}))}{\sqrt{(2\pi)^{\mathbf{N_j}} |\Sigma|}}, \tag{2.7}$$

where Σ is the covariance matrix. The individual likelihoods are described in the following sections. Similar to Schönrich & Bergemann (2014), we include spectra, photometry, parallax, stellar evolution models, and asteroseismic constraints, when available.

The core parameter space is defined as follows. The quantities $T_{\rm eff}$, $\log g$, and [Fe/H] represent the *key parameter space*, which all grids (photometric, asteroseismic, spectroscopic) of the SAPP share. On the other hand, mass M, age τ, and radius R, Luminosity L, and abundances are secondary parameters. They can only be inferred from some of the grids and so have dependencies on each of the three parameters in the *key parameter space*.

2.3.2 Synthetic photometry

The photometry PDF $P(O_{mag,dist}|\mathbf{X})$ relates magnitudes and parallaxes to the model predictions. We denote the stellar model magnitudes at model point i and magnitude k_1 by m_{i,k_1} and the photometric observation in the filter k_1 (such as G, $G_{\rm Bp}$ or $G_{\rm Rp}$) with O_{k_1}:

$$P_i(O_{\mathrm{mag,dist}}|\mathbf{m},d,r) = \prod_{k_1}^{N_{k_1}} P(O_{k_1}|m_{i,k_1},\mu(d),A_{k_1}(r)), \tag{2.8}$$

in accordance with equation (2.6),

$$P(O_{k_1}|m_{i,k_1},\mu(d),r) = G_j(m_{i,k_1} - (O_{k_1} - \mu(d) - A_{k_1}),\sigma_{k_1}), \tag{2.9}$$

where the extinction value is $A_{k_1}(r)$ is a function of reddening,r, and μ(d) = 5 log(d)-5 is the distance modulus and σ_{k_1} is the photometric error combined for the k_1 band.

The extinction in an individual photometric band is calculated using:

$$R_{k_1} = \frac{A(k_1)}{E(B-V)}, \tag{2.10}$$

where the values of R were adopted from Casagrande et al. (2011):

$$R_{k_1} = \begin{cases} 4.23,\ k_1 = \mathrm{B_T} \\ 3.24,\ k_1 = \mathrm{V_T} \\ 0.86,\ k_1 = \mathrm{J} \\ 0.5,\ k_1 = \mathrm{H} \\ 0.3,\ k_1 = \mathrm{Ks} \end{cases} \tag{2.11}$$

For the Gaia EDR3 dataset, the A_G value can be given, however it is not always available/correct (REF). In this case, (G_{Bp}-G_{Rp}) color-dependent extinction coefficients presented in Casagrande et al. (2021a) are used for G, G_{Bp} and G_{Rp} (see Fig. 2.4). For the magnitudes, we separate the PDFs entirely (G, G_{Bp}, G_{Rp}) and (H, J, Ks, B, V).

2.3.3 Distance and extinction uncertainties with respect to photometry

To include the uncertainty of distance modulus and extinction in computing the photometric PDF, μ(d) and A_{k_1} must be considered as separate quantities. In equation 2.9, μ(d) and A_{k_1} enter as parameters in each band with no error, to account for the measured value and error, an additional factor in the likelihood is introduced,

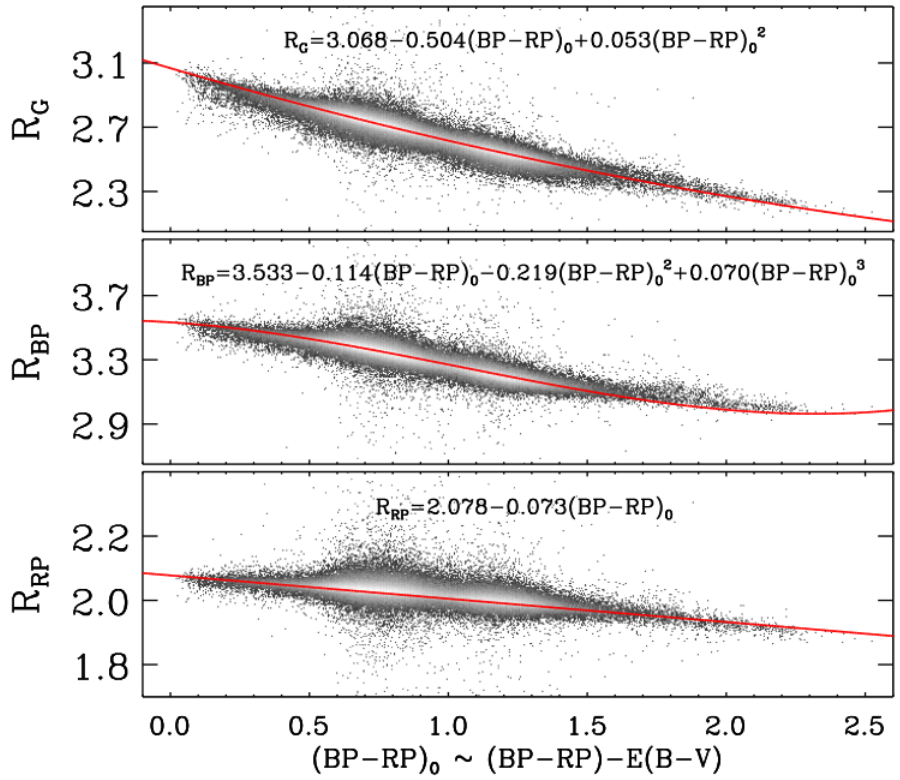

Figure 2.4: De-reddened colour-dependent extinction coefficients for each Gaia filter, G, G_{Bp} and G_{Rp}. Figure 1 in Casagrande et al. (2021a).

$$P_{i,\alpha,\beta} = P_i(O_{\mathrm{mag,dist}}|\mathbf{m},d,r) \times \exp\left[-\frac{(\mu_\alpha - \mu(d))^2}{2\delta\mu(d)^2}\right] \times \exp\left[-\frac{(A_{k_1,\beta} - A_{k_1}(r))^2}{2\delta A_{k_1}(r)^2}\right], \tag{2.12}$$

where $P_{i,\alpha,\beta}$ is marginalised over parameters μ_α and $A_{k_1,\beta}$ which vary over a large range in values centering around the observed quantities μ(d) and A_{k_1}.

2.3.4 Asteroseismic constraints

Cool stars, typically FGK, show ubiquitous oscillations which are excited by convective motions in their envelopes, the same mechanism responsible for solar oscillations. These so-called solar-like oscillations are characterised by a regular pattern showing modes of consecutive radial order to be almost equally spaced in frequency. The difference in frequency values of such consecutive modes determines the large frequency separation $\Delta\nu$. Moreover, the

distribution of power as a function of frequency shows a well defined peak at the so called frequency of maximum power, $\nu_{\rm max}$. These two quantities are related through standard asteroseismic scaling relationships (e.g. Chaplin & Miglio 2013; Serenelli et al. 2017) to fundamental stellar parameters as follows:

$$\Delta\nu \simeq \Delta\nu_{\odot} \sqrt{\frac{\rho}{\rho_{\odot}}} = \Delta\nu_{\odot} \sqrt{\frac{M}{R^3}} \tag{2.13}$$

where $\Delta\nu_{\odot} = 135.1$ μHz (Huber et al. 2011), ρ is the mean density of the star, and $\rho_{\odot}$ is the solar mean density, and the last equality assumes the stellar mass M and radius R are expressed in solar units.

For $\nu_{\rm max}$, the relation is:

$$\nu_{\rm max} \simeq \nu_{\odot} \frac{g}{g_{\odot}} \sqrt{\frac{T_{\rm eff,\odot}}{T_{\rm eff}}} = \nu_{\odot} \frac{M}{R^2} \sqrt{\frac{T_{\rm eff,\odot}}{T_{\rm eff}}}, \tag{2.14}$$

where the solar values are $\nu_{\odot}$ = 3090 μHz (Huber et al. 2011), $\log g_{\odot} =$ 4.44, and $\rm T_{eff,\odot}$ = 5777 K (Heiter et al. 2015) and, again, the last expression assumes solar units for M and R.

The $\nu_{\rm max}$ taken from the stellar evolution model is calculated using the aforementioned relationship, given the model values of $T_{\rm eff}$, M, and R. However, $\Delta\nu$ is computed from the radial orders (l=0) according to the prescription in White et al. (2011). We denote the stellar model asteroseismic quantities at model point i and quantity $\rm k_2$ by $\nu_{{\rm seism},i,k_2}$. It should be stressed that $\nu_{\rm max}$ and $\Delta\nu$ are, strictly speaking, not direct observables. The analysis of light curves and the oscillation power-spectrum is a complex and non-trivial procedure that involves a number of parameters, and it is far beyond the scope of this work to incorporate it into the present scheme[4]. We therefore refer to these quantities as observables (Belkacem et al. 2011). The asteroseismology likelihood is constructed as:

$$P_i(O_{\rm seism}|\nu) = \prod_{k_2}^{N_{k_2}} P(O_{k_2}|\nu_{i,k_2}) \tag{2.15}$$

$$P(O_{k_2}|\nu_{i,k_2}) = G_j(\nu_{i,k_2} - O_{k_2}, \sigma_{k_2}) \tag{2.16}$$

[4]It shall be kept in mind that dedicated PLATO WPs are in charge of the light curve analysis.

2.3.5 Spectroscopy

Pre-processing of spectra

Typically when spectra are taken, depending on the facility the data is run through a reduction pipeline which cleans the data of atmospheric interference such as tellurics (these aren't always caught), blaze functions, cosmic rays and other features. Some pipelines also perform continuum normalisation on the spectra, however, these aren't always fully successful. Meaning, the spectra collected is not ready for science. It must be further processed by the studies intending to analyse the data. We found a plethora of these issues for different spectra collected. For example, spectra from Gaia-ESO iDr5 fit files were somewhat continuum normalised but not fully, the given continuum was closer to 5 percent above unity. HARPS and UVES spectra were not always continuum normalised and also suffered from different contaminants. They both had to be corrected for telluric and treated for cosmic rays.

i. Contaminant treatment

We mask the pixel location of the tellurics by inspecting the solar spectra for each given facility and then used those masks for any spectra taken by those telescopes. The masks were via "Noising-up" the errors i.e. we increase the error at the telluric pixel and 1.7 Å around it such that the fitting routine does not mistake it for a line. The cosmic ray treatment is simple, we apply a sigma clipping routine to the spectra pre-normalisation. The spectra are clipped to 2.5 sigma, no less otherwise vital information is lost. This is very important to treat as the cosmic ray contamination appears as an emission line, thus it will affect the continuum normalisation routine, since we use linear fitting.

ii. Normalisation routine

1. Search through spectra for negative fluxes, zero value or NaN pixels (this can happen due to reduction pipelines/bad pixels on CCD). If any bad pixels are found, remove said pixels from spectra.
2. Sigma clip the data to remove cosmic ray emissions. See fig. 2.5
3. Search through the spectra for any significant gaps (lost data)
4. Split spectra into individual segments. We developed our own list of zones to split the data in by carefully inspecting the wings of strong lines that appear in the spectra. See fig. 2.6

5. Divide the entire spectra by its median value. We found this aids in the normalisation routine by bringing the overall spectra closer to unity. For example if most of the points are above 1, dividing by the median will reduce the spectra down, if most of the points are below 1, dividing by the median will increase the spectra towards 1.
6. Find a linear regression fit for each segment. Divide the segment by said fit.
7. For each segment, split data in half (the split point actually is the pixel closest to unity within 2.5 of the middle pixel), divide by the median and find a linear fit for each half. Divide each half by its given linear fit.
8. Ignore the previous step if the lines are deemed as broad. For example, H_α line would be too broad for this secondary normalisation to work.
9. Stitch each normalised segment together and output the continuum normalised spectra. An example of normalised spectra for Gaia-ESO HR10, UVES and HARPS can be seen with fig. 2.12.

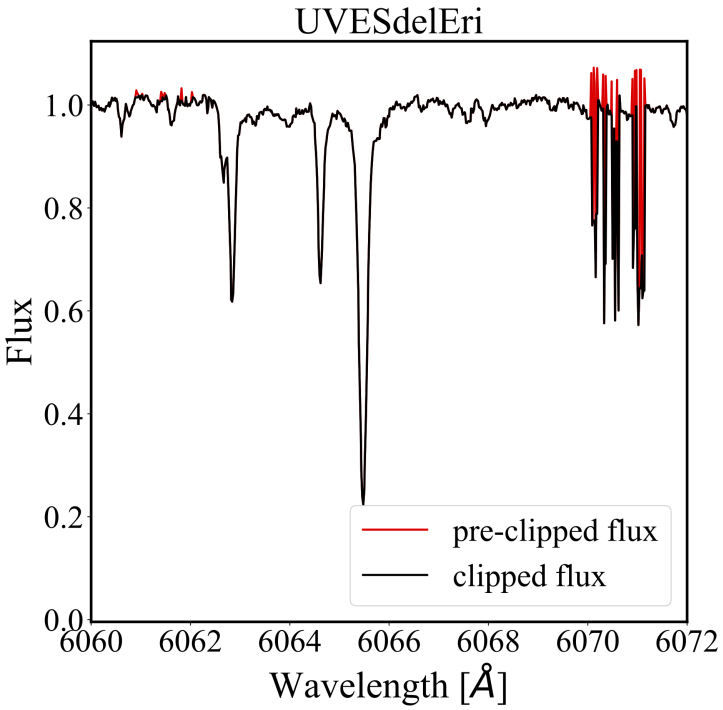

Figure 2.5: Comparing UVES spectra of the star δ Eri before and after sigma clipping with $\sigma = 2.5$

Radial-velocity correction

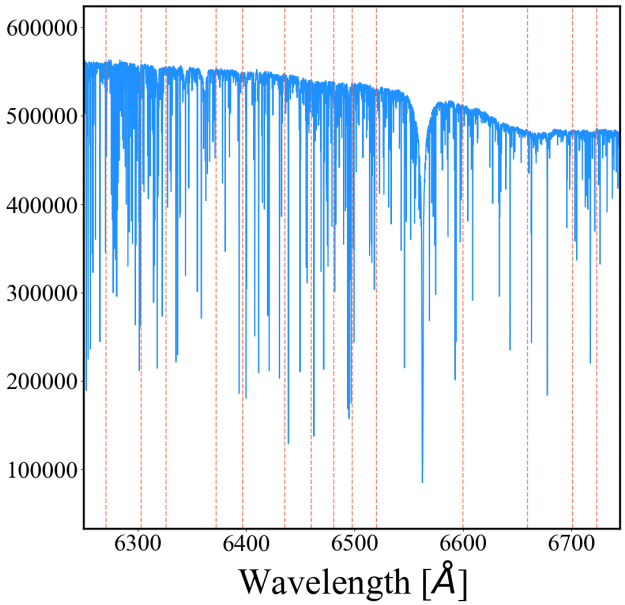

Figure 2.6: 18 Sco HARPS-North spectra (blue solid line) from 6250 to 6745 . The red-dashed lines over-plotted represent wavelength segments defined within the continuum normalisation routine.

After continuum normalising spectral data and treating contaminants, a further reduction step is required, radial velocity correction. The radial-velocity of a star represents the relative motion of the star with respect to the observer at the time of observation. The motions doppler shift the light and either blue shift or red shifts it. What we observe is the spectra is shifted along its wavelength scale by some amount.

This greatly affects analysis of the spectra of the star, specifically the line profiles of the models will not match the lines from the observations. This will result in a high χ^2 value for many pixels and thus produce an erroneous "best-fit" model with incorrect parameters. We decided to write our own RV correction procedure as it is relatively simple and allows us to verify the RV value given typically with the spectral data (sometimes it is not given). To shift the spectra to rest frame with a RV value known, the following equation is required,

$$\lambda_0 = \lambda_{obs}/(\Delta RV/c + 1) \tag{2.17}$$

Our procedure took direct inspiration from PyAstronomy RV correction module, *PyAstronomy.pyasl.crosscorrRV*, which is a collection of astronomy pack-

ages (Czesla et al. 2019). The procedure we follow involves testing a range of RV values, doppler shift the observed spectrum and compare it to a model which is in the rest frame. As all the stars in our benchmark sample are on the main-sequence and so sub-giant/dwarfs, we only require one model for RV correcting our spectra, a Main-Sequence star such as our Sun. A spectral model of R $\approx$ 500,000 was created using Turbospectrum (Plez 2012) with the classical parameters of the Sun (see table .2.1). This model works as a template because despite some changes in the HR Diagram, all the stars' line profiles should approximately match the location of the Solar line profiles. Therefore, one linearly shifts the observed spectrum and see how well the lines match. This is done via Cross-Correlating, a method whereby we measure the similarity of two spectra (observed and model) as a function of the displacement of one relative to the other. To calculate the Cross-Correlation exactly, the procedure does the following:

1. Create a list of plausible ΔRV values, for example -50 to 50 kms^{-1} with a resolution of 0.05 kms^{-1}.
2. For each ΔRV value, interpolate the model template spectra onto the observation spectra wavelength frame. This can be done by making λ_{obs} the subject of equation 2.17, thus $\lambda_{0,shift} = \lambda_0 \times (\mathrm{RV/c} + 1)$ where λ_0 in this case is the original model wavelength (i.e. rest frame). Interpolating ensures the model wavelength scale sampling matches the observation scale exactly.
3. Calculate the Cross-Correlation value using the following equation,
$$\mathrm{CC} = \sum_i \mathrm{flux}[i]_{\mathrm{obs}} \times \mathrm{flux}[i]_{0,\mathrm{shift}},$$
where i represents the wavelength pixel. This total number is the CC value given the ΔRV value used.
4. Calculate CC for all ΔRV values and locate where the maxima occurs, this will indicate the ΔRV value required for Radial-Velocity correction.

Figure 2.7 depicts two sub-figures with the results of calculating the RV correction of UVES α Centauri A spectra. The first sub-figure plots a variable called "CC" (Cross-Correlation) versus RV correction in kms^{-1}, here we see the peak of the CC is at ΔRV = -36.2 kms^{-1}. The second sub-figure shows three spectra, the black solid line is the observed spectra pre-shifted, the black dashed line is the observed spectra RV shifted and the grey solid line is the Solar model.

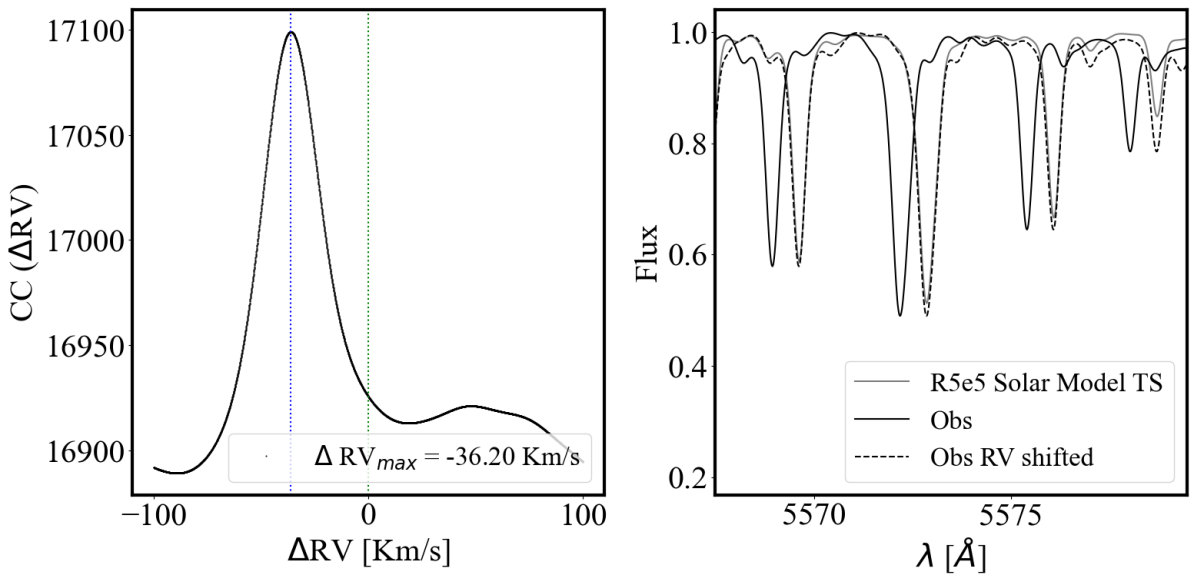

Figure 2.7: Two subfigures representing the radial-velocity correction process for a UVES spectra of Alpha Cen A convolved to HR10 resolution. Sub-figure on the left depicts the Cross-Correlation value versus the doppler rv shift for a given model and observation comparison. The Sub-figure on the right shows the radial-velocity corrected spectra (black solid line) and the un-corrected spectra (black dashed line) versus the high resolution Solar model from Turbospectrum (grey solid line).

Spectroscopic models

The main difference with the approach outlined in Schönrich & Bergemann (2014) is our code does not use synthetic grids directly, but relies on the Payne algorithm. This is a fast model-reconstruction technique, which is based on artificial neural networks (ANN) (Ting et al. 2016, 2019). The conceptual idea of the method is to use an ANN (or a set of ANNs) to represent how the flux at each point across the stellar spectrum varies with each individual stellar parameter, e.g. the $T_{\rm eff}$ (but the number of parameters is only limited by the dimensionality of the spectral grids). Once trained, the ANN layers, which act like a function that predicts a flux value at each point, can be used to quickly re-create an almost exact copy of the original spectrum. The typical error of the flux is $\lesssim 10^{-3}$, which corresponds to the interpolation error of $\lesssim 0.1\%$ (Kovalev et al. 2019). Such "generic" spectra can be used to quickly create analogues of stellar spectra computed ab-initio. The input training grids of synthetic spectra must be computed on a random mesh and must be uniformly distributed in the full space of parameters.

Here we use the Payne model trained on an 8-D grid ($T_{\rm eff}$, $\log g$, [Fe/H], micro-turbulence $v_{\rm mic}$, $v_{\rm brd}$ (which accounts for macro-turbulence and pro-

jected rotation velocity $v \sin i$), [Mg/Fe], [Ti/Fe], [Mn/Fe]). The training grids (see Kovalev et al. 2019, for more details) cover the entire parameter space of FGKM-type main-sequence stars, sub-giants and red giants, that is $4000 \leq T_{\rm eff} \leq 7000$ and $1.0 \leq \log g \leq 5.0$, and metallicity $-2.6 \leq$ [Fe/H] $\leq +0.5$. $v_{\rm brd}$ is used because it is not possible to resolve the separate influence of macro-turbulence and rotation broadening components at the typical resolving power of observed stellar spectra (see also Mashonkina et al. 2017; Kovalev et al. 2019). Both $v_{\rm mic}$ and $v_{\rm brd}$ are randomly and evenly distributed in the parameter space, corresponding to typical values measured for FGK stars. $v_{\rm mic}$ varies from 0.5 to 2 km^{-1}, whereas $v_{\rm brd}$ varies from 5 to 25 km^{-1}. The elements are chosen, because for them reliable NLTE atomic models were available to us at the stage of model grid development. The reference solar composition adopted in that grid was taken from Grupp (2004a) and scaled-solar abundances were used for all elements, except Mg, Ti, Fe, and Mn, for which the meteoritic values from Grevesse & Sauval (1998) were used. The main advantage of this approach, compared to classical methods, is the significant improvement in performance. The standard method, which relies on symmetric grids with an equidistant step size is computationally very costly and forbids computing separate grids for all possible detailed abundances, while still keeping up with the rapid developments in atomic and molecular physics (e.g. Belyaev & Voronov 2020; Den Hartog et al. 2021) and 3D NLTE radiative transfer methods (e.g. Bergemann et al. 2019; Gallagher et al. 2020; Bergemann et al. 2021). The current grids allow us to determine [Mg/Fe], [Ti/Fe], [Mn/Fe], but it can be extended to an arbitrary number of chemical elements in future.

The physics of the input model spectra was extensively described in Kovalev et al. (2019). In short, these are synthetic spectra models computed using 1D NLTE radiative transfer for Fe, Mg, Ti, and Mn. The MAFAGS-OS (Grupp 2004a,b) 1D hydrostatic model atmospheres with opacity sampling (OS) were used, owing to their more extended parameter coverage (up to mid A-type) and denser grid sampling. We note, however, that extensive comparative tests were performed in different studies, showing that the MAFAGS-OS and MARCS model (Gustafsson et al. 2008) provide very similar thermodynamic structures and results based on these models are virtually identical (Bergemann et al. 2012, 2019). Owing to the assumption of hydrostatic equilibrium, the transport of energy by convection has to be parametrised. In the MAFAGS-OS model, the latter is computed using the mixing-length theory

(Böhm-Vitense 1958; Cox & Giuli 1968; Canuto & Mazzitelli 1991). Microturbulence, the parameter that - for the lack of full 3D RHD treatment - approximates the effect of velocities on scales smaller than the photon mean free path, is a free parameter in the grid. We note, however, that the calculations of new multi-dimensional NLTE grids with average 3D models are already in progress, and the grids will make the use of ad-hoc adjustable parameter $v_{\rm mic}$ obsolete.

Model-data comparison

In the spectroscopic module, the SAPP relies on the gradient descent method, a standard first-order iterative optimisation algorithm that allows to locate the global minimum in the parameter space. As shown in Kovalev et al. (2019), the main advantage of the gradient descent method is that it allows to greatly speed-up the spectroscopic analysis compared to other methods. The average run-time of this module is about 0.4 seconds per star, and this procedure yields all spectroscopic quantities, including $T_{\rm eff}$, metallicity, detailed chemical abundances, etc.

Once the global minimum in the 8-D parameter space is found, we construct the spectroscopic PDF P($O_{spec}|\mathbf{X}$) by assuming a normal distribution with the 1 σ uncertainty for $T_{\rm eff}^{spec}$, $\log g_{spec}$, and [Fe/H]$_{spec}$ which are provided by the gradient descent method. Other types of spectroscopic PDFs were extensively studied in Schönrich & Bergemann (2014). The other derived spectroscopic parameters (chemical abundances, $v_{\rm brd}$, $v_{\rm mic}$) are kept at their best fit values. The discretisation and parameter space of the spectroscopic PDF follows the model grid points defined by the stellar evolution tracks described in Sect. 2.3.8. We note, however, that the latter has no influence on the shape and amplitude of P($O_{spec}|\mathbf{X}$).

Hence, P($O_{spec}|\mathbf{X}$) for a given parameter space model point i is indexed over quantity k_3,

$$P_i(O_{spec}|\mathbf{X}) = \prod_{k_3}^{N_{k_3}} P(O_{k_3}|\mathrm{X}_{i,k_3}), \tag{2.18}$$

for each spectroscopic parameter O_{k_3},

$$P(O_{k_3}|\mathrm{X}_{i,k_3}) = G_j(\mathrm{X}_{i,k_3} - O_{k_3}, \sigma_{k_3}) \tag{2.19}$$

where $O_{spec} = T_{\rm eff}^{spec}$, $\log g_{spec}$, $[\rm Fe/H]_{spec}$ and $\mathbf{X}_i = T_{{\rm eff}i}$, $\log g_i$, $[\rm Fe/H]_i$ respectively. For this construction of spectroscopic PDF, $N_{k_3} = 3$, and k_3 indexes from 1.

For the case of covariance, equation 2.7 is used instead of equation 2.5.

Error model

Since our model grids have only eight dimensions, we have implemented a more restrictive approach with respect to the statistical analysis of individual observations. Kovalev et al. (2019) used the full spectrum fit, however, this is sub-optimal, because different spectral lines correspond to the abundances of different chemical elements across the entire periodic table, and using low-dimensional training grids does not allow to account for the true chemical abundance patterns of the star, which are in most cases not scaled-solar (Bergemann et al. 2014).

Therefore, in this work, instead of pre-selecting spectral lines by eye, as it has been common in previous literature studies, we resort to a robust statistical procedure. The procedure entails a comparison of the reference synthetic spectra of the benchmark stars (using the reference stellar parameters and abundances obtained as described in Sec. 2.2.2) with the observed spectra that allows to find the wavelength regions that are poorly described by our synthetic models. These regions are not masked, but rather we evaluate the residuals between the model flux and observed flux at each wavelength point. These mono-chromatic residuals, which we refer to as "the error model", serve as systematic uncertainties, so that the total combined error per wavelength point is determined by adding the error model in quadrature with the observed flux error.

Fig. 2.8 shows such a map of residuals ordered by Z (atomic number of the element) in the wavelength window 5300 to 5600 Å . This procedure, as we show in Sect. 2.4.1 yields very robust results for the CONTROL sample of stars. Given the limitations of our 1D NLTE models, such as the absence of realistic treatment of convection and turbulent motions that are a fundamental property of FGKM-type stars - the use of the residual map is justified.

Correlation

It shall be pointed out that some spectroscopic parameters are highly correlated with each other, owing to underlying physics of energy transfer in stellar atmospheres. Fig. 2.9 shows the covariances for all eight parameters in the

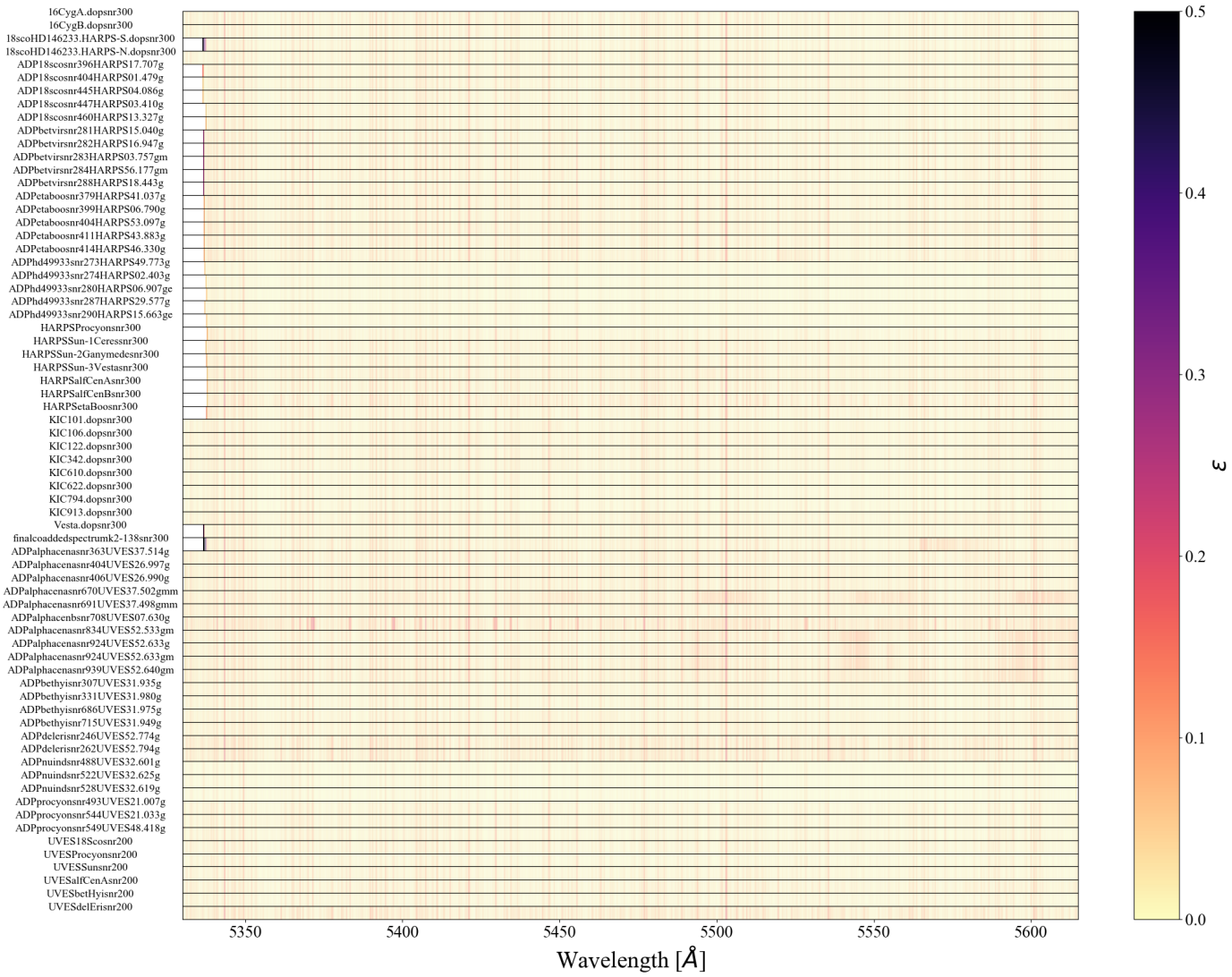

Figure 2.8: Y axes represents the name of the stellar spectra, the X axes is wavelength in angstroms. The colour axes represents the absolute residual between specific spectra and the stars corresponding reference model.

spectroscopic module. The core parameters - $T_{\rm eff}$, $\log g$, and [Fe/H] show the most significant correlation, but also the α-enhancement (e.g., [Mg/Fe] or [Ti/Fe]) and micro-turbulence correlate with metallicity in different regimes of parameter space. This is often the reason why alternative constraints on the core parameter space are necessary. The impact of covariance on the final results is discussed in Sect. 2.4.5.

2.3.6 Infra-red flux method

The Infra-Red Flux method (IRFM) is another efficient method to determine effective temperature and angular diameter of a star (e.g., Blackwell & Shallis

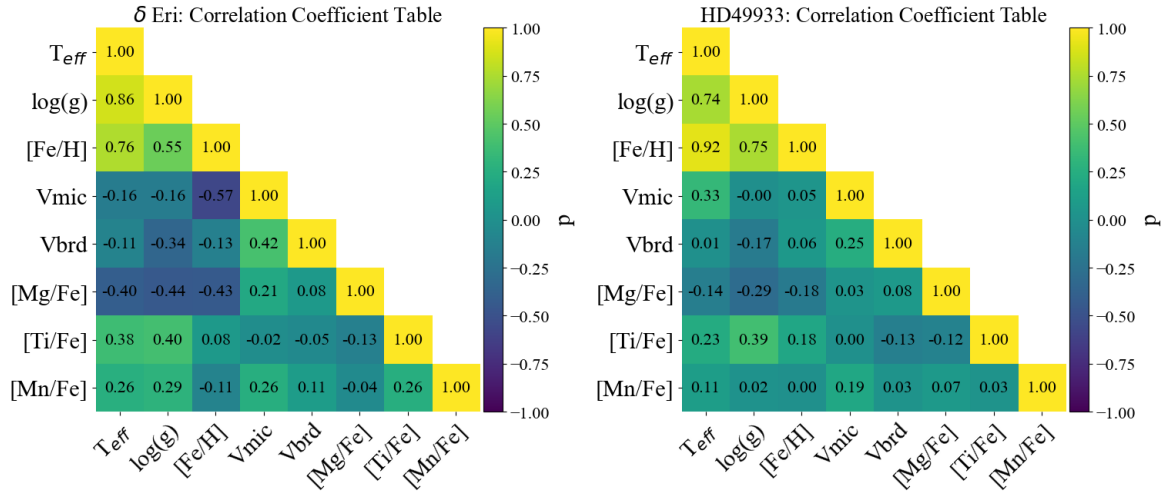

Figure 2.9: Correlation coefficient tables split into two sub-figures. Each sub-figure has a colour scale that represents the correlation coefficient, which ranges from -1 (negatively correlated), 0 (no correlation), 1 (positively correlated). This number informs how each spectroscopic parameter is correlated with another. The top panel is the table for a K-type star (δ Eri) and the bottom panel is a table for a F-type star (HD49933). The vertical and horizontal axes for both depict the 8 spectroscopic parameters from SAPP's spectroscopy module.

1977; Casagrande et al. 2006; González Hernández & Bonifacio 2009). The IRFM does not depend much on the physics of stellar model atmospheres employed (see e.g., Casagrande et al. 2006, 2010a, for a discussion of H^- opacity and the use of MARCS vs ATLAS9 models across FGK dwarfs, and Chiavassa et al. 2018 for an analysis of the use of 3D vs 1D models). An estimate of $\log g$ and [Fe/H] is also required, but has minimal impact on the methodology (see e.g, Casagrande et al. 2006; González Hernández & Bonifacio 2009, for a discussion)

However, the adopted interstellar reddening and absolute flux calibration can easily introduce systematic errors of order $\sim$ 100 K (Casagrande et al. 2006; Ruchti et al. 2013). In the context of this work, the use of IRFM is limited to stars with reliable 2MASS photometry, which is about half of those in Table 2.1 due to their brightness and 2MASS saturation. For some of the remaining stars with good photometry in fewer bands, we tested the colour-$T_{\rm eff}$ relations derived from the same implementation of the IRFM (Casagrande et al. 2020). These calibrations are available in up to 12 different colour combinations, with extra quality cuts based on photometry and realistic errors from a Monte Carlo approach[5]. The sensitivity of these relations to the adopted input parameters varies depending on the colour indices.

[5] https://github.com/casaluca/colte

In Sec. 2.4.2 we compare the results of $T_{\rm eff}^{\rm IRFM}$ with our spectroscopic $T_{\rm eff}$ values. This allows us to test the precision with which we can determine the $T_{\rm eff}$ by means of the IRFM method. This is important because we expect that this method, along with the Surface-Brightness Colour relationships (SBCR), will be the source of constraints on $T_{\rm eff}$ for those PLATO targets that do not have spectra.

2.3.7 Surface-brightness colour relationships

Surface-Brightness Colour relationships (SBCR) allow one to easily and independently estimate the limb-darkened angular diameter of the star. Combining the latter with the distance to the star, the linear radius can be computed. Furthermore, the combination with the bolometric flux yields the effective temperature.

Many SBCRs exist in the literature, but all of them are empirical and are calibrated on interferometric measurements (see Nardetto 2018 and Salsi et al. 2020 for a short review) or on Galactic eclipsing binaries (Graczyk et al. 2017, 2019). For example, Pietrzyński et al. (2019) derived the distance to the Large Magellanic Cloud with a 1 % precision using eclipsing binaries as distance indicators. In order to achieve such precision, they used a dedicated SBCR based on the observations of 48 red clump stars with the PIONIER/VLTI instrument (Gallenne et al. 2018). Assuming the expected 1% precision and accuracy of angular diameters expected from CHARA/SPICA (see Sect. 2.6), we estimate that the method will provide the precision of 50 to 100K in $T_{\rm eff}$ and 1 to 2% in radii.

The main advantage of the method is its simplicity: only two magnitudes (usually V and K) are required and it is not very sensitive to reddening, because the surface brightness and the colors have a similar sensitivity to extinction. For example, a difference of 0.2 mag in the visual extinction translates into a difference of 2% on the radius and 60 K on the temperature. For comparison, a 2% error on $F_{\rm bol}$ translates into an error of 30 K on the temperature. The main limitation of the method in the context of PLATO is likely its sensitivity to the uncertainty of the K magnitude. A 0.03 mag error in the K band magnitude causes an 80 K uncertainty in $T_{\rm eff}$ and a 2 % uncertainty on the radius. The results also depend on the spectral type and luminosity class (Salsi et al. 2020). Additionally, the method cannot be used for stars that show a significant activity level, have a companion(s), are flattened due to rotation

(Challouf et al. 2014, 2015), show signatures of wind and/or circumstellar shells.

In this work, we employ the SBCR relationships from Salsi et al. (2021), which were derived for F5-K7 IV/V stars using the methodology described in Salsi et al. (2020). The relationships are based on a careful selection of the interferometric data, suitable sample selection (no activity), and a homogeneous set of 2MASS photometry.

In Sect. 2.4.2, we compare our SBCR estimates obtained with these relationships with the reference values. The bolometric fluxes, which are needed in the SBCR method to determine $T_{\rm eff}$ from the linear radius, are taken from Heiter et al. (2015). However, it is expected that SAPP will provide bolometric fluxes as an output, from the photometric module.

2.3.8 Stellar evolution models

The SAPP code also includes a detailed grid of GARSTEC stellar evolution models (Weiss & Schlattl 2008), which covers the mass range from 0.6 to 5.0 $M_\odot$ with a step of 0.02 $M_\odot$ and metallicity from -2.50 to 0.60 with a step of 0.05 dex.

In short, the models were computed as follows. Stellar atmospheres are based on the T-τ VAL-C model (Vernazza et al. 1981), implemented with the analytic fit given in Sonoi et al. (2019). This relation leads to stellar models that reproduce well the $T_{\rm eff}$ scale of RGB stars in the APOKASC sample (Serenelli et al. 2017; Pinsonneault et al. 2018). Convective overshooting is treated in GARSTEC as a diffusion process parametrised with a coefficient f, which is fixed to 0.02 at all convective boundaries. This is roughly equivalent to an overshooting region extending over $0.2H_P$, with H_P being the pressure scale height at the convective boundary. For small convective cores, f is decreased linearly from 0.02 down to 0 for stellar masses from 1.4 down to 1.1 $M_\odot$. This prescription has been found to describe well results from binary stars (Higl et al. 2018) and mid-age open clusters (Semenova et al. 2020). No convective core overshooting in the main sequence is used below 1.1 $M_\odot$. Mass loss is modelled with a Reimers law and $\eta = 0.2$. Microscopic diffusion, without taking into account radiative levitation, is included according to Thoul et al. (1994). Its efficiency is suppressed linearly with stellar mass in the range $1.25 - 1.35$ $M_\odot$ and it is not included for higher masses. The

reason is that microscopic diffusion and radiative levitation in the presence of very thin convective envelopes lead to theoretically large changes in surface abundances not supported by observations, likely due to the presence of a yet physically unidentified macroscopic mixing process. For lower masses, however, extra-mixing below the convective envelope is included following the prescription described in VandenBerg et al. (2012), with a metallicity dependent efficiency adjusted to reproduce the solar lithium depletion and the depletion of lithium typical of the Spite plateau (e.g. Spite & Spite 1982; Sbordone et al. 2010) stars.

The relation between the abundances of metals and helium is assumed to follow a linear relation calibrated using the Standard Big Bang Nucleosynthesis (SBBN) helium value $Y_P = 0.2485$ (Steigman 2007) and a solar model calibration, which lead to a slope on the enrichement law $\Delta = 1.14$ (Serenelli et al. 2017). More recent determinations of Y_P lead to slightly lower values, ($Y_P = 0.2470 \pm 0.0002$ and $Y_P = 0.2446 \pm 0.0041$, consistent with each other, for SBNN and non-SBBN respectively Fields et al. 2020). The impact on the slope of the enrichment law is about 7%, equivalent to that produced by a [Fe/H] error of 0.025 dex.

In addition, the models include synthetic photometry computed using ATLAS12/SYNTHE bolometric corrections[6] for different passbands: UBVRI, 2MASS, Kepler, Gaia, Tess, Hipparcos, Tycho and PanStarrs. Bolometric corrections have so far been implemented corresponding to A_v=0, so extinction has been applied a posteriori. This leads to errors of approximately a few hundredths of magnitude for Av $<$ 2 mag.

2.3.9 Priors

Initial Mass Function

The Initial Mass Function (henceforth IMF) is an empirical function that describes the initial distribution of masses for a given population of stars. It was first derived for stars in the Solar neighborhood by Salpeter (1955). The study obtained the functional form,

$$\zeta(M) = \zeta_0 \, M^{-2.35} \tag{2.20}$$

[6] http://waps.cfa.harvard.edu/MIST/model_grids.html#bolometric

where ζ_0 is a constant which sets the local stellar density. Using the IMF one can determine the number of stars which form within certain mass limits. The common properties from the IMF is that most of the stars that form are low mass and most of the mass in stars reside in low mass stars i.e. the most common stars which form aren't high mass. However, following a burst of star formation, the luminosity from the star forming region is dominated by high mass stars (Salpeter 1955). This functional form of the IMF is well defined for Masses above 0.5 $M_\odot$ (Offner et al. 2014; Kroupa 2001), below this the function should flatten. Although, the exact form of low mass IMF remains uncertain.

The origin of the IMF is an unsolved astrophysical problem in star formation theory. On one hand, most theorists believe that the IMF is not necessarily the same everywhere in the universe, as different amounts of metals will affect fragmentation and so it is entirely possible for a significant number of high mass stars to form. On the other hand, observationally there is little to no evidence that the IMF varies in our Galaxy or in nearby galaxies (Offner et al. 2014).

To use this as a prior for our calculations, for simplicity unity is chosen for ζ_0.

The input mass used for this prior to be applied will derive from the stellar evolution models, these track the mass evolution of the star and so applying the IMF will have a small constraint on the age but a significant constrain on Radius. All of the stars in our sample are within the local Solar neighbourhood arguably and so using the simpler IMF is justified.

2.3.10 Numerical approach

The exact procedure is as follows.

In this first step, $T_{\rm eff}$, $\log g$, and [Fe/H] are fixed to the best fit spectroscopic value determined using the gradient descent method. This is because this method is fast and it does not require probing the entire parameter space. In the second step, the SAPP collects stellar evolution tracks which have $T_{\rm eff}$, $\log g$, [Fe/H] centred on the first-guess parameters within a certain range defined by the user. For simplicity, we limit the sub-domain range to $\pm$ 300 K in $T_{\rm eff}$, $\pm$ 0.5 dex in $\log g$, $\pm$ 0.6 dex in [Fe/H]. Alongside these parameters collected, mass, radius, age, and luminosity are also tabulated. Figure 2.10

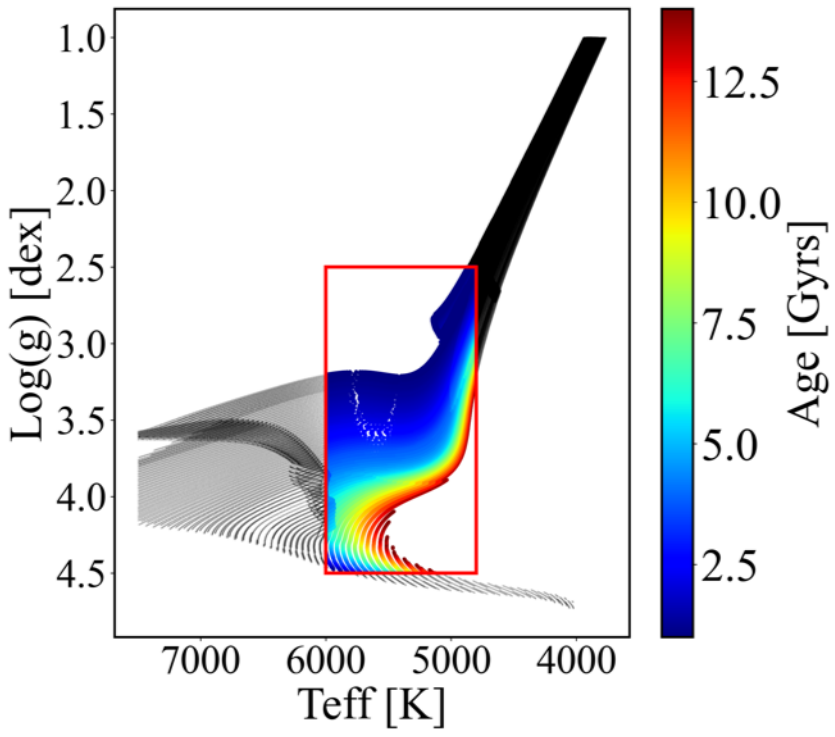

Figure 2.10: Kiel diagram of GARSTEC stellar evolution tracks used in SAPP coloured in age within the red box defined by a range of $T_{\rm eff}$, $\log g$, and [Fe/H].

depicts an example selection of tracks based on a conservative range.

Second, for each point in the sub-domain of the stellar evolution models, *i*,the spectroscopic probability is calculated using equations 2.18,2.19. Figure 2.11 shows the 3D parameter space of Procyon's spectroscopic PDF sampled directly from the 8D space (left) and re-constructed using the best-fit parameters, uncertainties and covariance matrix (right).

Finally, this spectroscopic PDF defined on the sub-domain of stellar evolution models is folded with the PDFs computed from photometric, astrometric, and asteroseismic data. This procedure returns the full posterior PDF.

The final estimates of all output parameters ($T_{\rm eff}$, $\log g$, [Fe/H], M, age, R, L) are calculated by fitting a Gaussian to the posterior PDF with mean μ and standard deviation σ. In other studies, Schönrich & Bergemann (2014), the expectation values and their moments were used However, our extensive inspection of the posterior PDFs showed that they are rather symmetric and can all be well approximated by a Gaussian.

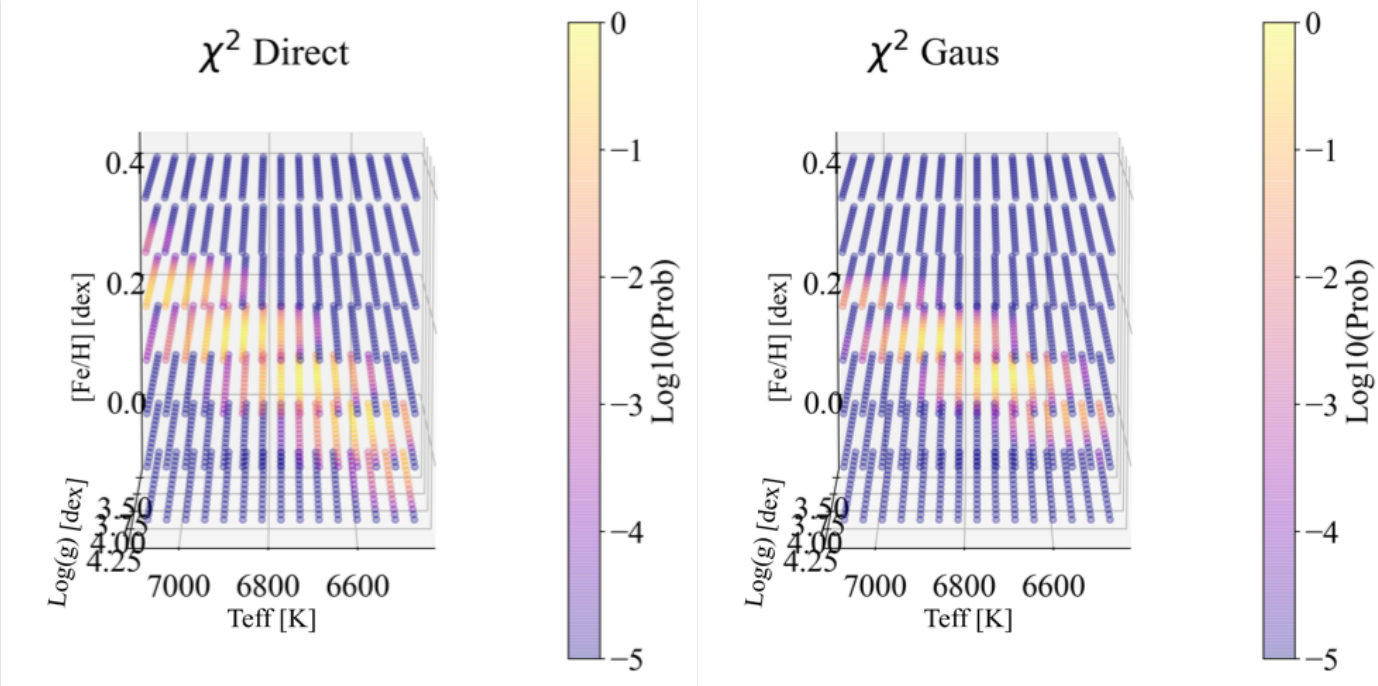

Figure 2.11: 3D parameter space in $T_{\rm eff}$, $\log g$, [Fe/H] mapped onto a regular grid with colour scale as log likelihood probability $P(O_{spec}|\mathbf{X})$ of Procyon spectra. Left panel shows spectroscopic PDF directly sampled from 8D parameter space (keeping $v_{\sin i}$, $v_{\rm mic}$ and abundances fixed). The Right panel shows spectroscopic PDF re-constructed using best-fit parameters, uncertainties and the co-variance matrix.

2.4 Results

The results of our analysis of the benchmark stars will be discussed in detail below. We will begin with quantifying the accuracy and precision of our estimates of $T_{\rm eff}$, $\log g$, and [Fe/H] obtained using different spectroscopic approaches and different types of observational data (Sect. 2.4.1). We will then proceed to the analysis of using IRFM and SBCR to calculate $T_{\rm eff}$ and radius (Sect. 2.4.2). The influence of seismic priors on $\log g$ and so on the analysis of other stellar parameters will be the subject of Sect. 2.4.3. The results for masses, radii, and ages of stars obtained using the full Bayesian solution will be presented and discussed in Sect. 2.4.4. The impact of including covariance from spectroscopy is detailed in Sect. 2.4.5. Finally, the analysis of medium resolution spectra is shown in Sect. 2.4.6.

Figure 2.12 depicts three spectra (black dots) of α Cen B (one of the reference targets) from different telescopes compared to best fit spectra models from SAPP (magenta lines). A medium resolution spectra (HR10) with R = 20, 000 and two high-resolution spectra (UVES, HARPS) with original R = 47, 000 and 118, 000 respectively. The high resolution spectra have been degraded to that of HR10 in order to demonstrate the performance of fitting different quality spectra of the same star. The original resolutions are annotated above each spectra as well as a sample of diagnostic lines which populate the HR10 wavelength range. This is just for an illustration, but the agreement for all other stars in the sample is equally good. The agreement between the observed data and the models is very good, which suggests that the SAPP in combination with available theoretical models can be used with confidence to analyse spectra of FGK-type dwarfs and sub-giants.

2.4.1 Constrained versus unconstrained spectroscopic calculations

We begin with the analysis of the influence of the error model (see Sect. 2.3.5) on the spectroscopic calculations. Hereafter, we refer to the results obtained using the error model as "constrained" analysis, and those obtained without the error model as an "un-constrained" analysis.

We find that the accuracy of stellar parameters, $T_{\rm eff}$, $\log g$, and [Fe/H], is significantly improved, if the error model is employed with respect to the reference stars. The scatter of the SAPP $T_{\rm eff}$ estimates decreases from 101 K (unconstrained analysis) to 42 K (constrained analysis) and the bias de-

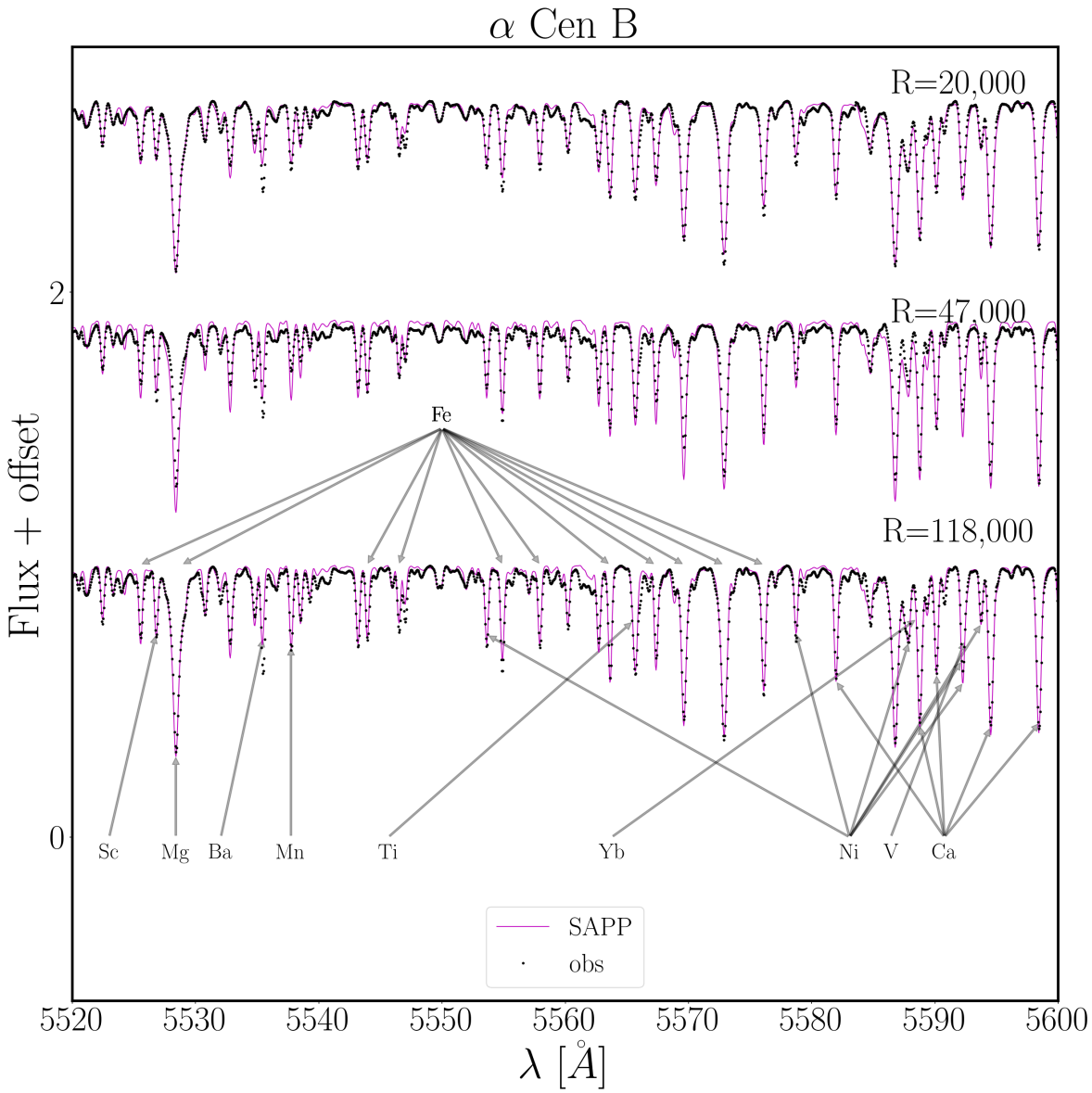

Figure 2.12: Normalised Flux versus wavelength in angstroms. The observed spectra of α Cen B (black dots) is overlaid with SAPP's best fit model from the spectroscopy module (magenta solid line). This contains HARPS, UVES and HR10 spectra with original resolving powers R$\sim$ 118 000, 47 000 and 20 000 respectively. The UVES and HARPS spectra have been convolved down to that of HR10.

creases from 109 K (unconstrained analysis) to -1 K (constrained analysis). Even more impressive is the improvement in $\log g$ estimates. The systematic $\log g$ bias decreases from -0.16 dex (unconstrained analysis) to -0.04 dex (constrained analysis) and the scatter reduces enormously, from 0.13 dex to 0.02 dex, which makes our spectroscopic results competitive with other techniques, such as asteroseismology. As Fig. 2.13 shows, in the unconstrained analysis the residuals are large and positive. The constrained analysis, in con-

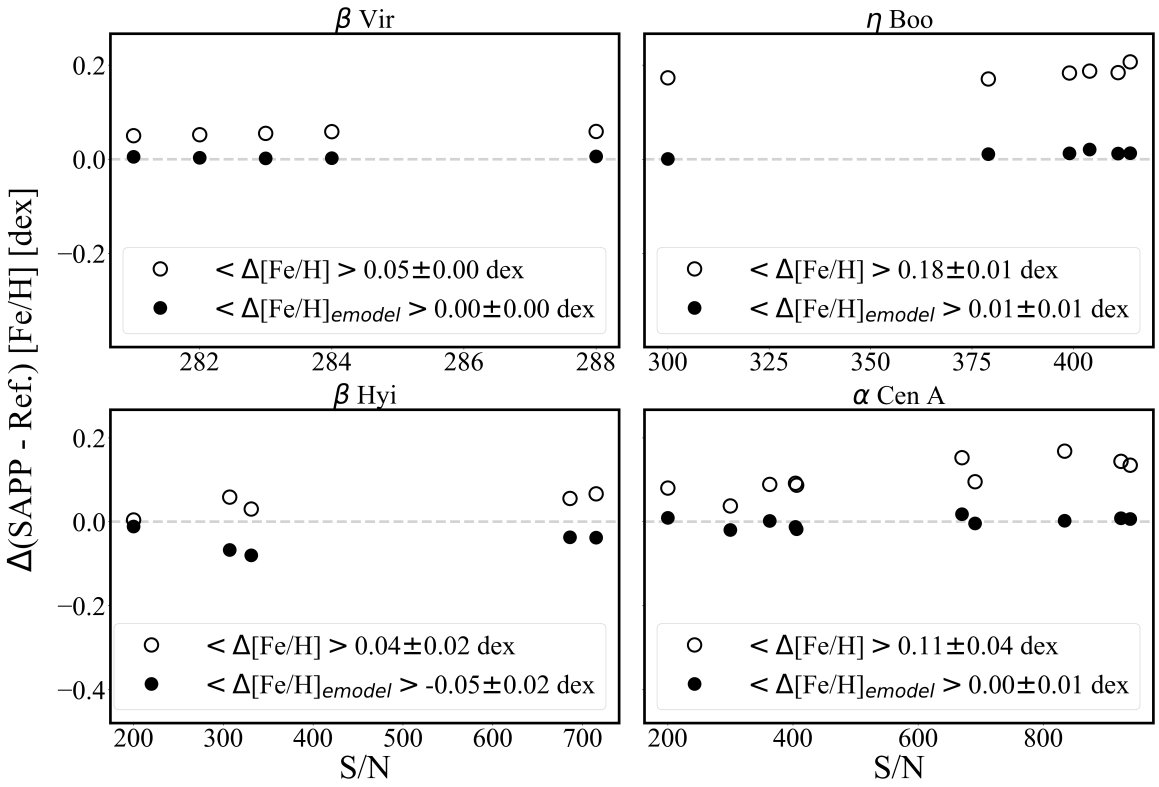

Figure 2.13: Residuals between SAPP parameters and reference versus the signal-to-noise ratio of four stars: β Vir, η Boo, β Hyi, and α Cen A. Open circles represent using purely spectroscopic module (without error model), these have an average and 1σ in the legend named $\langle\Delta$[Fe/H]$\rangle$. Filled circles represent using spectroscopic module with the error model, these have an average and 1σ in the legend named $\langle\Delta$[Fe/H]$_{emodel}\rangle$.

trast, is much more successful, because it removes all systematic effects and returns metallicities with the precision of 0.02 dex,this is likely due to the error model reducing the impact of features within the spectrum which are consistently causing the [Fe/H] to be initially overestimated. Not surprisingly, the constrained analysis also improves the results for the detailed chemical composition of stars. The abundances of Ti, Mg and Mn are in excellent agreement with the reference values, with mean differences of 0.02 ± 0.04 dex, 0.04 ± 0.04 dex, and -0.04 ± 0.03 dex, respectively.

It should be stressed, however, that the literature values of[Fe/H] and any other element abundances cannot be treated as 'reference' quantities, because there is no model-independent (fundamental) way to determine the detailed chemical composition star. All methods depend on models of stellar atmospheres, atomic, and molecular physics, and, therefore, on the level of physical complexity of the systems. Therefore, most differences between our values and the reference metallicities stem from the different radiative transfer

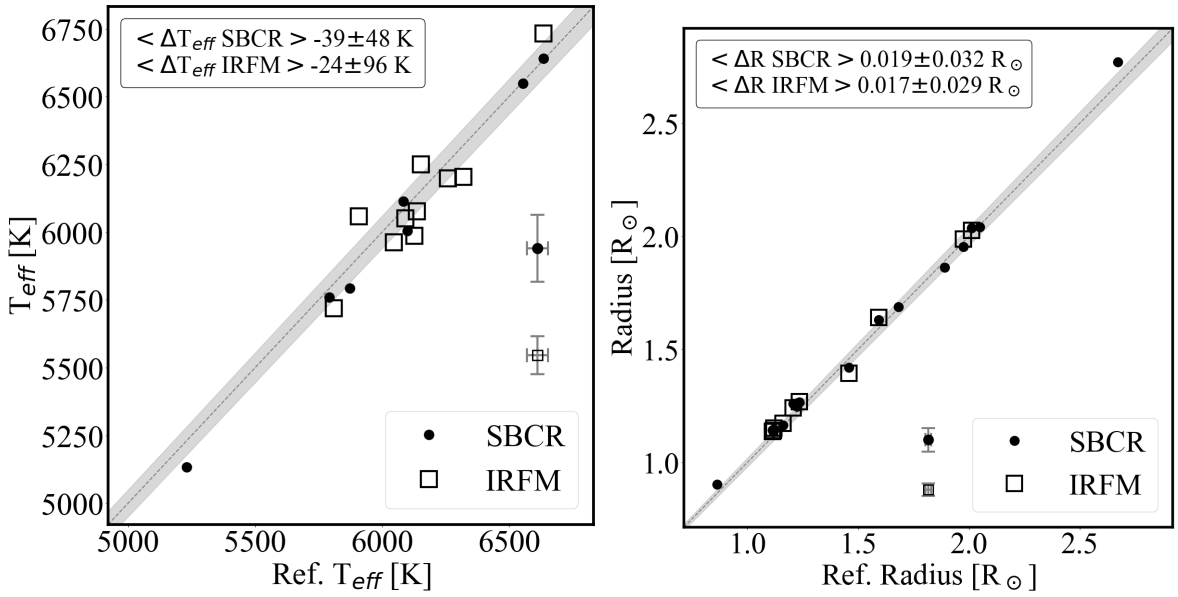

Figure 2.14: Comparison of effective temperatures (top panel) and radii (bottom panel) derived from the SBCR (solid circles) and IRFM (open squares) method to Reference values. The dark grey line corresponds to the 1:1 line, the light grey shaded region represents our adopted threshold of 2%. The average uncertainty for IRFM, SBCR (vertical) and Reference (horizontal) is annotated in the middle right for $T_{\rm eff}$ and bottom right for radii. The annotation in the upper left represents the average difference between SBCR, IRFM and Reference with 1 σ scatter about said average respectively.

methods and input physics employed in the spectroscopic calculations.

2.4.2 IRFM and SBCR modules

In this section, we explore whether constraints on $T_{\rm eff}$ from the IRFM and SBCR methods could help improve the estimation of the effective temperatures.

Figure 2.14 (top panel) shows our estimates of $T_{\rm eff}$ obtained using the IRFM and SBCR method in comparison with the reference $T_{\rm eff}$ measurements. The results based on both methods are sensitive to the quality of photometry and to extinction, therefore we limit this comparative analysis to stars with the 2MASS flags "A" or "B", which corresponds to the photometric errors below 0.05 mag in the J, H, and K_s bands. Generally, we find that both methods provide an excellent constraint on the $T_{\rm eff}$ of a star, with the average bias of only ~ -32 K and the scatter of ~ 73 K around the reference values. The uncertainties of the IRFM estimates are of the order ~ 70 K. As to SBCR, the uncertainty on the effective temperatures is ~ 123 K, but it ranges from 98 to 138 K depending on the quality of photometry.

Figure 2.14 (bottom panel) compares the resulting SBCR and IRFM radii of stars with the reference values. The uncertainties indicated in the figure are the quadratic sum of the individual uncertainties. The SBCR uncertainties, of the order ~ 0.052 $R_\odot$ are dominated by the RMS error of the method, with the precision of $\sim$ 3.1 to 4.5%. The IRFM radii are slightly more precise, with $\sigma \sim 0.027 R_\odot$.

We conclude that both methods, SBCR and IRFM, require accurate and precise 2MASS photometry (with errors less than 0.05 mag) in order to achieve the PLATO space mission requirements. Also extinction may influence the results. Currently, both methods may be used as auxiliary methods to constrain $T_{\rm eff}$ and radii, foremost as priors on spectroscopy. However, their use as standalone modules will require an improvement in the parameter coverage and reference parameters of the calibration samples. In particular, we anticipate that with the data from the upcoming CHARA/SPICA facility, the SBCR method will be improved significantly to reach the desired precision of $1-2\%$ on the radii.

2.4.3 Influence of seismic priors on stellar parameters

In the subsequent analysis, we investigate whether the use of asteroseismic data improves the constraints on stellar parameters, compared to the approach when only stellar spectra are used. So far, most studies employing asteroseismic constraints on $\log g$ have reported an improvement in the accuracy of results (Bruntt et al. 2012; Buchhave & Latham 2015; Nissen et al. 2017).

We use two asteroseismic quantities: $\nu_{\rm max}$ – the frequency of the maximum oscillation power – and $\Delta\nu$ – the large frequency separation (e.g. Serenelli et al. 2017). These seismic data are used as a prior in two methods. The first approach is to estimate a $\log g$ value from the asteroseismic PDF, which utilizes both quantities and then fix it in the spectroscopic analysis. We note that instead of fixing the surface gravity, a prior on $\log g$ can be imposed, however, for the benchmark stars this alternative approach yields the same result. This is due to the very small, of the order 0.01 to 0.02 dex, uncertainties on the seismic $\log g$ values.

We also explore a different approach, in which the final solution is obtained using an iterative algorithm, with $\log g$ constrained via the empirical $\nu_{\rm max} = f(T_{\rm eff}, \log g)$ relationship (e.g. Belkacem et al. 2012). In short, using the

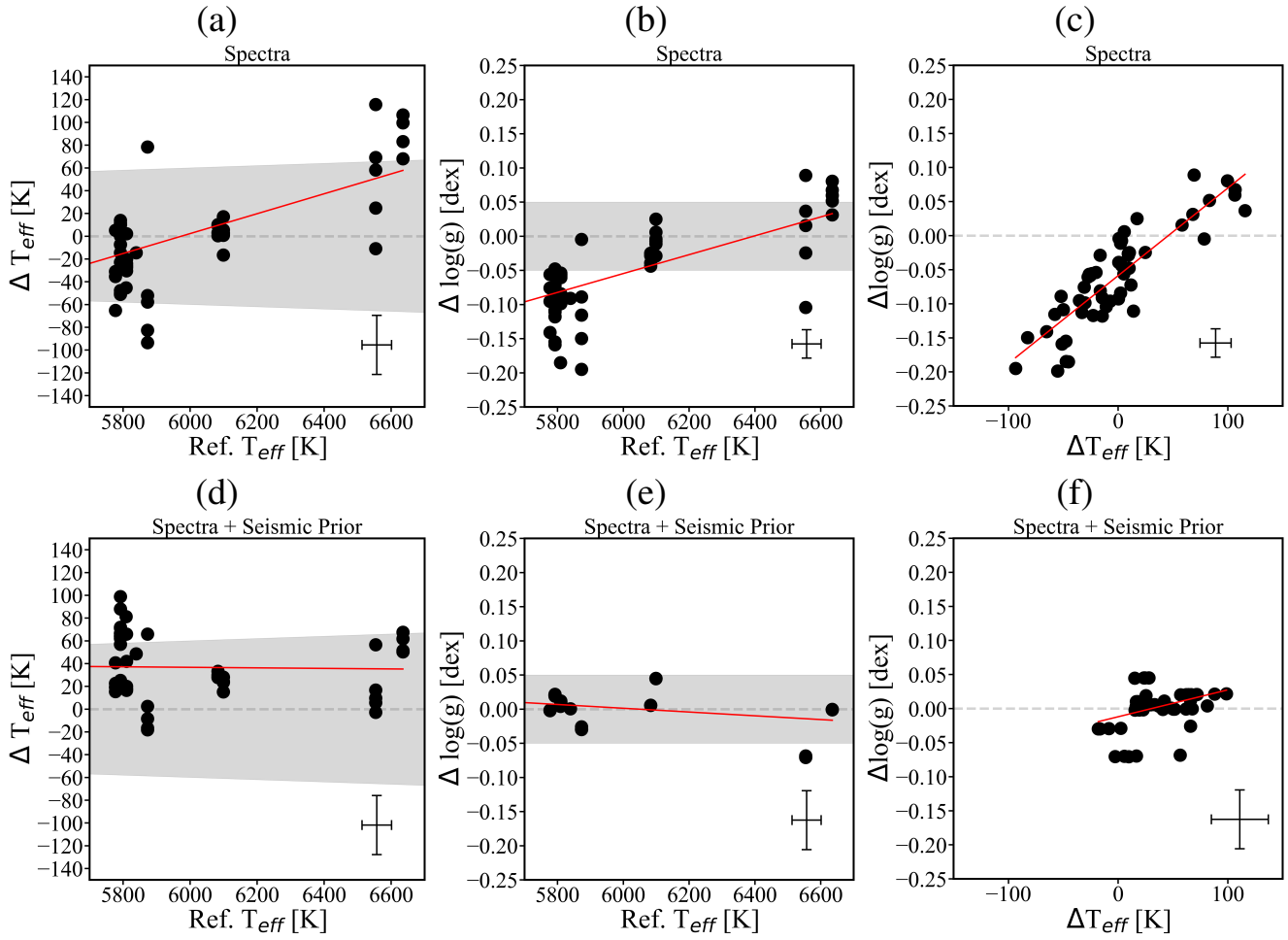

Figure 2.15: SAPP spectroscopic parameters $T_{\rm eff}$ and $\log g$ of the benchmark stars which have interferometric $T_{\rm eff}$ reference values above 5500 K (this includes two KIC stars 16 Cyg A and B). The vertical axis represents the residuals between $T_{\rm eff}$, $\log g$ and their corresponding reference values. The horizontal axis represents the reference parameters. The red line is a linear regression of the data points. The top panel contains results produced by SAPP's constrained spectroscopy module, and the bottom panel contains results produced by SAPP's constrained spectroscopy module with ν_{max} prior applied. The grey shaded region is our tolerance of 1% for $T_{\rm eff}$ and 0.05 dex for $\log g$. The average uncertainty in each panel is located in the bottom right. For each star, several spectra were analysed (see Sect. 3.2)

.

observed stellar and solar ν_{max} values, we input an initial guess of $T_{\rm eff}$ from spectroscopy, the resulting $\log g$ value from the equation 2.14 is then fixed in the spectroscopic analysis. The re-calculated set of parameters give a new estimate of $T_{\rm eff}$, which is used in the same equation, and the loop continues until the $T_{\rm eff}$ estimate does not change by more than 10 K. The choice of this convergence criterion is not critical at this stage and the convergence is usually very fast.

Figure 2.16 shows the iterative process for spectra of the Sun from Ceres taken by HARPS. Whereby the process determines a new $\log g$ given a spectral $T_{\rm eff}$ and asteroseismic $\nu_{\rm max}$ using equation 2.14. Once a $\log g$ is calculated, it is fixed and the spectroscopy module is re-run, therefore determining a new $T_{\rm eff}$ which is used in the same equation. The change in effective temperature is tracked and represents the vertical axis, the number of iterations represents the horizontal axis.

Such an approach has been adopted, for instance, by Lund et al. (2019). Figure 2.15 shows our results obtained without and with a $\log g$ prior, using the iterative solution with $\log g$.

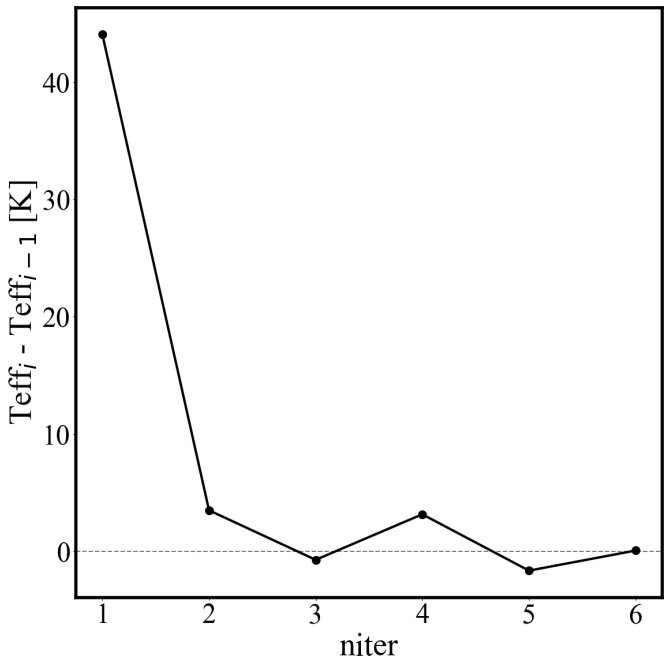

Figure 2.16: Difference between effective temperature estimations per iteration versus number of iterations. This is the iterative method described in section 2.4.3 for the Sun, specifically Ceres HARPS spectra.

Overall, it is clear that the use of seismic prior on $\nu_{\rm max}$ improves the accuracy of $T_{\rm eff}$ and $\log g$ estimates (compare panels (a)-(d) and (b)-(e)), resolving

the notorious problem of systematically under- or over-estimated temperatures and surface gravities (Mortier et al. 2014; Tsantaki et al. 2019). The iterative solution improves not only the accuracy (central values), but also the precision of the results: the scatter of $T_{\rm eff}$ residuals is reduced by a factor of two, from $\pm$42 K to $\pm$21 K. The uncertainties of individual values, however, increase slightly when a seismic prior is applied, which is due to the error in ν_{max} being taken into account. Without the seismic prior, the uncertainties are purely statistical in nature. The most obvious improvement concerns the stars with $T_{\rm eff} \gtrapprox 6200$ K: Procyon and HD 49933. For these F-type stars, the spectroscopic analysis without any prior returns a very problematic (and well-known) systematic bias in $T_{\rm eff}$ and $\log g$, which manifests itself in the unfortunate correlation between the residuals of the both parameters (Fig. 2.15, panel c). In other words, the $T_{\rm eff}$ over-estimated by 100 K also implies that the $\log g$ estimate is $\sim +0.1$ dex too high. The causal connection between the residual of $T_{\rm eff}$ and that of $\log g$ cannot be established, as both parameters are highly correlated (Fig. 2.9). Remarkably, including the seismic priors resolves the problem: the $T_{\rm eff}$ and $\log g$ values are now in a good agreement with the reference values, with systematic bias on the order of 40 K between the two quantities.

Accurate surface gravity estimates are essential to determine chemical abundances from gravity-sensitive spectral lines, such as Mg triplet lines at 5100 , Ca near-IR triplet lines, and the majority of diagnostic lines of singly-ionised elements (Gehren et al. 2004; Lind et al. 2012; Bergemann et al. 2017).

We therefore conclude that, similar to $T_{\rm eff}$, the seismic prior offers a clear improvement in surface gravity and helps to break the degeneracy between the influence of $\log g$ and $T_{\rm eff}$ for stars hotter than the Sun.

2.4.4 Bayesian solution

In this section, we describe the results obtained, when all stellar parameters are determined consistently using the Bayesian approach (Sect. 2.3.1), employing photometric (magnitudes), astrometric (parallaxes) , spectroscopic, and asteroseismic ($\Delta\nu$, ν_{max}) data. As emphasised in Sect. 2.1, we want to leverage the exquisite statistical capabilities of Bayesian inference methods and therefore we also include stellar structure models, which gives us the ability to determine radii, masses, and ages of stars in the consistent homogeneous framework. This also allows us to quantify the correlations between

various parameters and to explore the influence of uncertainties in the fundamental parameters of stars: their initial mass and detailed chemical composition.

Figure 2.17 depicts the PDFs for Procyon from different modes of SAPP with the vertical axes as $\log g$ and the horizontal axes as $T_{\rm eff}$. Each PDF shows the likelihood landscape sliced in the [Fe/H] dimension with respect to their maximum probability. The colour scale is the logarithm of the corresponding probability, over-plotted is an evolution track with M = 1.5 $M_{\odot}$ and Z = $Z_{\odot}$, the best-fit value is plotted as a white cross. The differences in Figs. 2.17d,e, and f are subtle, (d) represents the combination of the Spectroscopy PDF and Asteroseismology PDF, this is analogue to our constrained spectroscopy + ν_{max} prior results. Fig. 2.17 (e) represents the PDF resulting from the combination of Spectroscopy and Photometry with parallax included, and (f) represents the PDF resulting from the full Bayesian scheme. The probability range of 10^{-50} to 1 allows us to see the detail of the likelihood landscape and how it changes with various combinations.

Our final results for the Bayesian scheme are provided in Table 2.2 and they are compared with the reference quantities in Figure 2.18. The average uncertainty for each panel is located in the bottom right. The systematic uncertainties of SAPP are determined from the average differences calculated and shown in the annotations of each sub-figure. Therefore, the final values presented in table 2.2 have the statistical and systematic uncertainties combined. For the stars which have multiple observation spectra, the final values are averaged and the uncertainties are propagated thoroughly. Clearly, our results for all stellar parameters are in excellent agreement with other estimates. The $T_{\rm eff}$ estimates are accurate to $27(\text{syst.}) \pm 37(\text{stat.})$ K (~ 0.5 %), whereas the error on $\log g$ and [Fe/H] does not exceed $0.00(\text{syst.}) \pm 0.01(\text{stat.})$ dex and $0.02(\text{syst.}) \pm 0.02(\text{stat.})$ dex, respectively. Also the estimates of radii, masses, and ages of the benchmark stars are consistent with the reference values. Radii and masses are best determined, with the statistical uncertainty of only 0.03 $R_{\odot}$ and 0.05 $M_{\odot}$ respectively. Ages are determined with a precision of 0.63 Gyr and a small bias of ~ -0.14 Gyr. It shall be stressed, however, that ages are highly model-dependent quantities, and their determination, in turn, relies on the quality of atmospheric parameters ($T_{\rm eff}$, [Fe/H], α-enhancement...). Also the reference values are highly heterogeneous, and were determined by different methods and models. Therefore a disagreement (however small) is not surprising and may simply indicate that different types

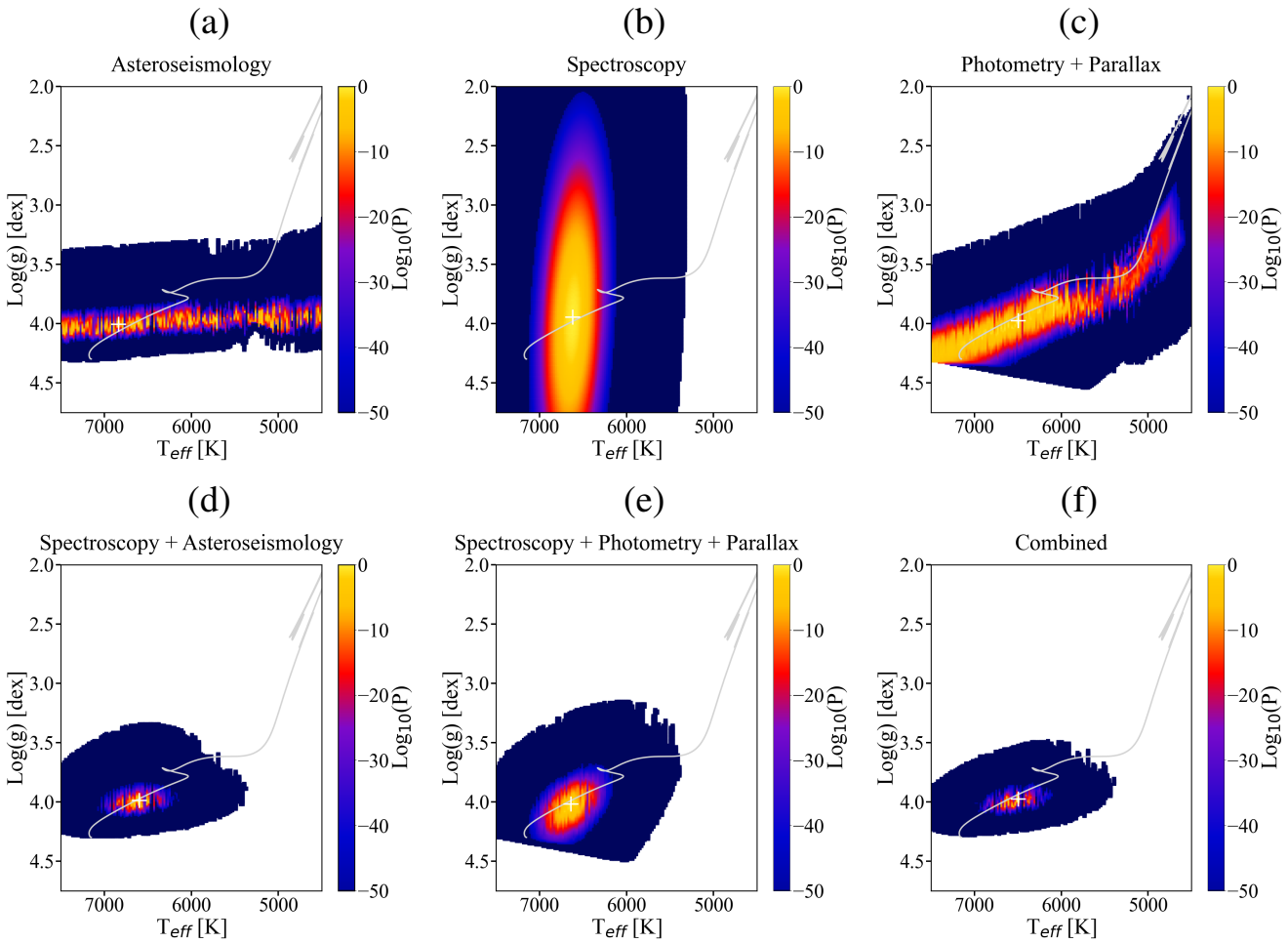

Figure 2.17: Five sub-figures depicting a PDF calculated for Procyon from different modes of SAPP a) Asteroseismology, b) Spectroscopy c) Photometry and Parallax, d) Spectroscopy and Asteroseismology, e) Spectroscopy and Photometry (with parallax) and f) Combined (Bayesian scheme). The horizontal axes is effective temperature, the vertical axes is surface gravity and the colour bar is the logarithm of probability. Each sub-figure PDF is sliced in [Fe/H] dimension. The grey solid line represents a stellar evolution track with 1.5 $M_{\odot}$ and Z = $Z_{\odot}$ (the Pre-Main Sequence is not included). The white cross represents the best fit value for the given PDF.

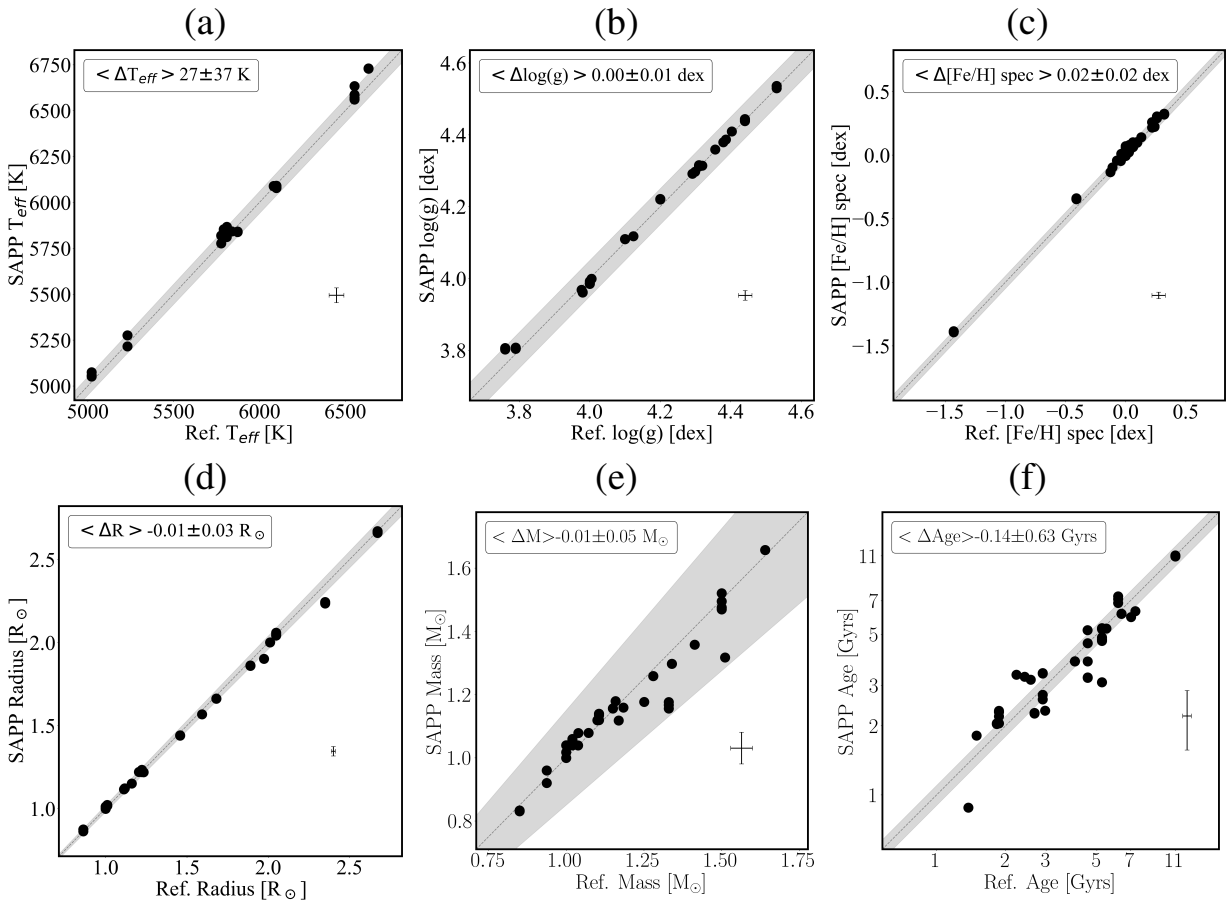

Figure 2.18: SAPP stellar parameters from the full Bayesian scheme versus the reference parameters. The annotations represent the average difference between the SAPP parameters with covariance and the reference parameters respectively. The uncertainty represents the 1 σ scatter about said average. The gray shaded region represents the desirable uncertainties of stellar parameters for PLATO: 1% for $T_{\rm eff}$, 0.05 dex for $\log g$ and [Fe/H], 15 % for mass, 10 % for age, 2 % for radius. The vertical error bars represent the average 1 σ uncertainties.

of stellar evolution models (or isochrones) and/or different input values for atmospheric parameters of stars were employed in the literature studies that we use for comparison with our results.

Comparing our final Bayesian results with the literature estimates (e.g. Sahlholdt et al. 2019; Das & Sanders 2019; Howes et al. 2019), we can conclude that the SAPP code provides robust estimates of fundamental stellar parameters, comparable or even superior to other methods. In Das & Sanders (2019), the precision of parameters is 10% on mass and 10-25% on age. Sahlholdt et al. (2019) find more conservative uncertainties, of the order $\sim 15-40\%$ on age. Howes et al. (2019) did not use asteroseismic information, and their estimates are strongly dependent on the evolutionary stage of a star, with typical uncertainties of 15% on age at the turn-off and RGB, but reaching up to 50% on the main-sequence and sub-giant branch (see their Fig. 18). Our results are qualitatively similar to these estimates, if we were to limit the input data to observed spectra, photometry, and parallaxes, but the use of asteroseismology greatly improves the precision of M, R, and τ, allowing to constrain their values to a precision of a few (1 to 5%) percent for masses and radii, and 15% for ages. Whereas in PLATO (see section 2.5), these quantities will not be determined using the SAPP, our results suggest that the SAPP delivers robust and accurate estimates of atmospheric and fundamental parameter of stars, making the code useful for the characterisation of stars observed within other ongoing and forthcoming programs, such as WEAVE, 4MOST, and SDSS-V.

2.4.5 Spectroscopy parameter covariance impact on bayesian scheme

The current formulation of spectroscopy produces a PDF that can reliably be combined with other modules. In this section, we explore the influence of using the spectroscopic covariance (Eqn. 2.7 in Sect. 2.3.1) in the full Bayesian calculations.

We have also compared the results for stellar parameters computed with and without the inclusion of spectroscopic covariance. Figure 2.19 explores the difference between using the covariance matrix from spectroscopy and assuming independence between spectroscopic parameters in the Bayesian scheme. For each parameter, the difference is plotted against the reference value of each star with the average uncertainties annotated in the bottom right corner. The grey shaded region represents the desired tolerance of the final results.

Fig. 2.19 confirms that the differences between the results obtained using the two approaches are small. The only somewhat significant deviation can be seen in $T_{\rm eff}$ and τ, which scatter around $\sim \pm$ 40 K and 0.67 Gyrs, respectively. We do not detect any significantly large systematic bias associated with the assumption of independent likelihoods.

The inclusion of covariance is formally correct with respect to statistical analysis, as otherwise the assumption is that the core parameters and their errors are independent. It is also not a significant problem in terms of calculation overheads, as the covariance matrix is always available as a by-product of spectroscopic calculations in the SAPP (Sect. 2.3.5). On the other hand, it is clear that the influence of using the covariance is small in the parameter space of FGK-type stars. We can therefore conclude that it is not critical to include the spectroscopic covariance in the full Bayesian analysis, as long as one does not require the precision of better than 1 percent in the astrophysical characterisation of stars.

2.4.6 Analysis of medium-resolution spectra

Gaia-ESO benchmark stars

We present our results obtained from the analysis of medium-resolution HR10 spectra of the Gaia-ESO benchmark stars and compare them with the independently-determined stellar parameters (see Sect. 2.2.2). The GIRAFFE HR10 spectra cover a narrow wavelength range from 5300 to 5600 at the resolving power of 20 000. The median S/N is in the range from 70 to over 2 000. The HR10 spectra have lower sampling than the degraded UVES and HARPS spectra analysed in Sect. 2.4.4, this allows the difference of instrument effects to be explored. These stars also include one FGK sub-giant (HD 140283), two red giants (ξ Hya, HD 122563), an F dwarf (HD 84937), and two G dwarfs (μ Ara, τ Cet). These targets are important because red giants highlight the extent of SAPP's applicability towards metal-poor stars outside of PLATO's core program. In Fig. 2.20 a total of 17 benchmark stars are analysed, where the SAPP estimates of $T_{\rm eff}$, $\log g$, [Fe/H] are compared to the reference values, respectively. The average uncertainty values are shown in the bottom right corner. The upper panel depicts SAPP data derived without asteroseismology data, and the lower panel with asteroseismology. The red data points represent stars which have no asteroseismic information, therefore are identical in both panels.

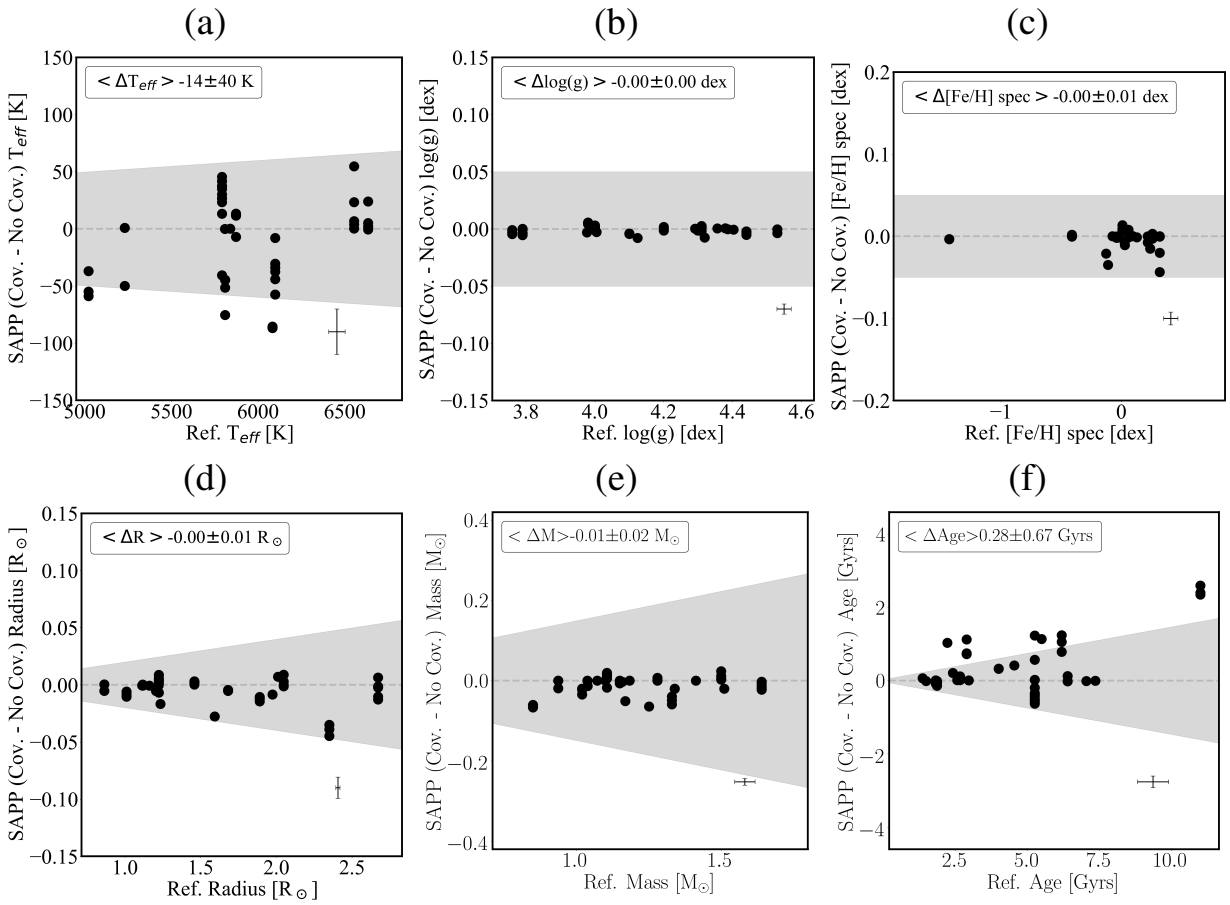

Figure 2.19: The differences between SAPP best-fit parameters from Bayesian scheme calculated with and without covariance matrix from spectroscopy (vertical axes) versus the reference parameters presented in Table 2.1 (horizontal axes). The uncertainty represents the 1 σ deviation. The gray shaded region represents the desired errors: 1% for $T_{\rm eff}$, 0.05 dex for $\log g$ and [Fe/H], 15 % for mass, 10 % for age, 2 % for radius.

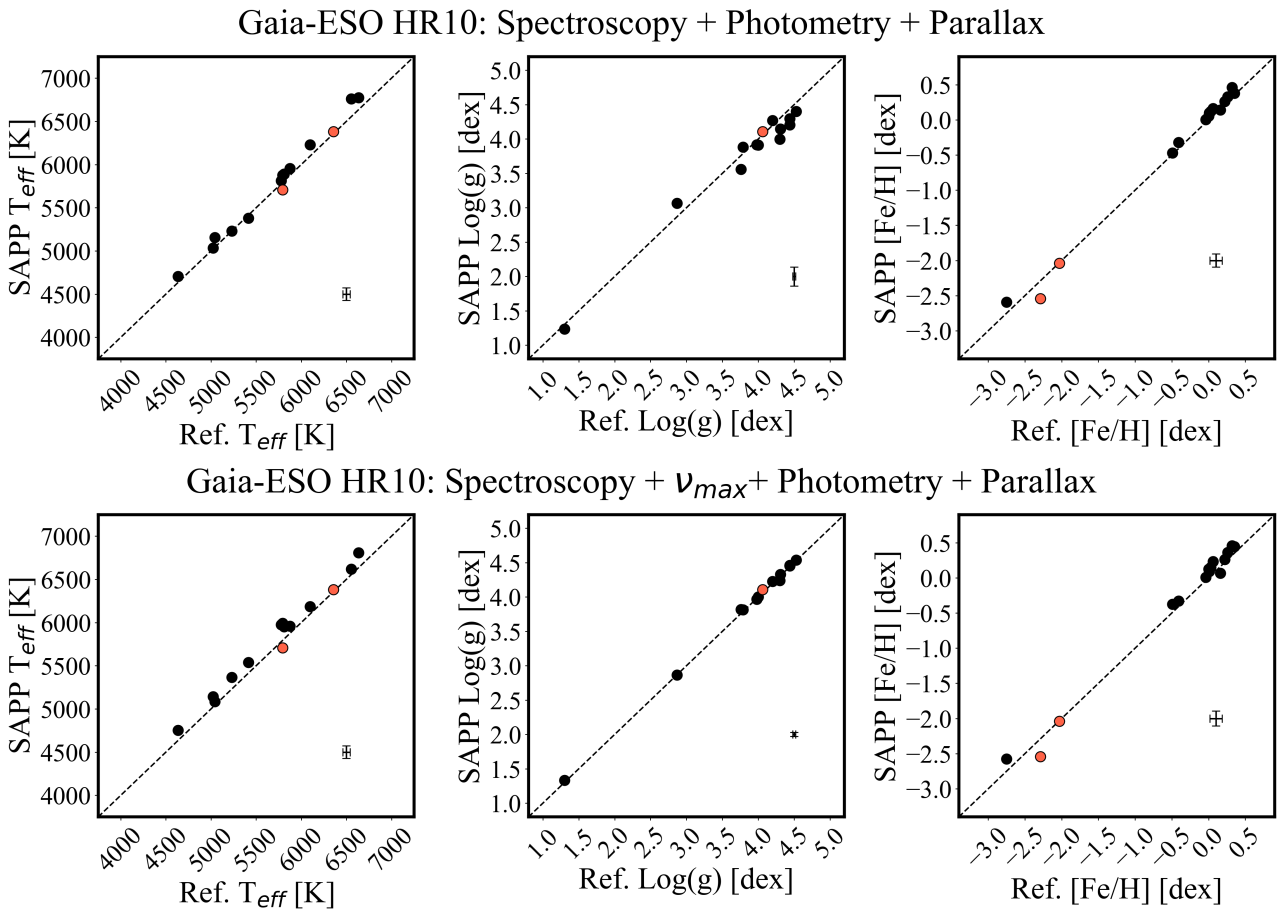

Figure 2.20: SAPP best-fit parameters of Gaia-ESO HR10 spectra from Bayesian scheme, with resolution R = 20,000 and coverage $\lambda \subset$[5300,5600] . In total there are 17 benchmark stars depicting a different parameter ($T_{\rm eff}$ $\log g$, [Fe/H] and [Mg/Fe]) derived from SAPP (vertical axes) versus the given reference parameter (horizontal axes). The panels represents data determined using the Bayesian scheme without asteroseismology (upper) and with asteroseismology (lower). The red data points represent stars without any asteroseismic parameters.

We find that the analysis of medium-resolution stellar spectra with the SAPP also yields reliable results. If asteroseismic constraints are used, we obtain the average $T_{\rm eff}$ bias of about ~ 101 K and a dispersion of 76 K, very precise $\log g$ estimates on the order of 0.012 dex, and metallicities accurate to ≈ 0.05 dex. Also the Mg abundances can be determined with the uncertainty of $\approx\ 0.01 \pm 0.08$ dex. Interestingly, the $T_{\rm eff}$ value obtained from the HR10 spectra alone are superior to those obtained using $\nu_{\rm max}$. This could possibly be the consequence on non-trivial relationships between the physics adopted in the spectroscopic module (Sect. 3.4.1), which is based on MAFAGS-OS atmospheric models. The model atmospheres adopt the mixing length that is empirically constrained to reproduce observed Balmer line profiles (given a pre-defined $T_{\rm eff}$ scale), and may, therefore by coincidence, compensate for the deficits of the model atmospheres, yet at the expense of surface gravity accuracy. Nonetheless, our results in both cases reinforce the evidence that medium-resolution optical spectra, with $R \approx 20,000$, are well suited for the analysis of fundamental parameters and composition of PLATO stars. Spectra of such quality will be obtained in future with 4MOST (Bensby et al. 2019; de Jong et al. 2019) and WEAVE medium-resolution spectrographs (Dalton et al. 2014). Therefore it can be foreseen that the characterisation of PLATO targets can indeed be done at the required level of accuracy and precision, if 4MOST and WEAVE medium-resolution spectra are available.

Gaia-ESO open and globular clusters

In Figures 2.21 and 2.22 we present the results from our analysis of six open and globular clusters[7], for which Gaia-ESO HR10 spectra are available in the public Gaia-ESO data release[8]. None of the clusters were processed using the Asteroseismic module in SAPP, therefore only photometric, astrometric and spectroscopic data was analysed in this section. In Fig. 2.21, we also show several isochrones (derived from the GARSTEC stellar evolution tracks described in Sect. 2.3.8) with varying ages and similar metallicity respectively. These isochrones were not fit to the data, and are only displayed to guide the eye. The unique value of clusters is not just because they, to a first order, represent mono-age and mono-metallic stellar populations (Magrini et al. 2017; Bastian & Lardo 2018), but also because homogeneous observations of

[7]Cluster RV values from Gaia EDR3 were used to differentiate non-cluster members; here we adopted a typical threshold of 5σ in RV for all clusters, except NGC 6352, for which the threshold value of 3 $\rm kms^{-1}$ was assumed

[8]http://archive.eso.org/scienceportal/home?data_collection=GAIAESO&publ_date=2020-12-09

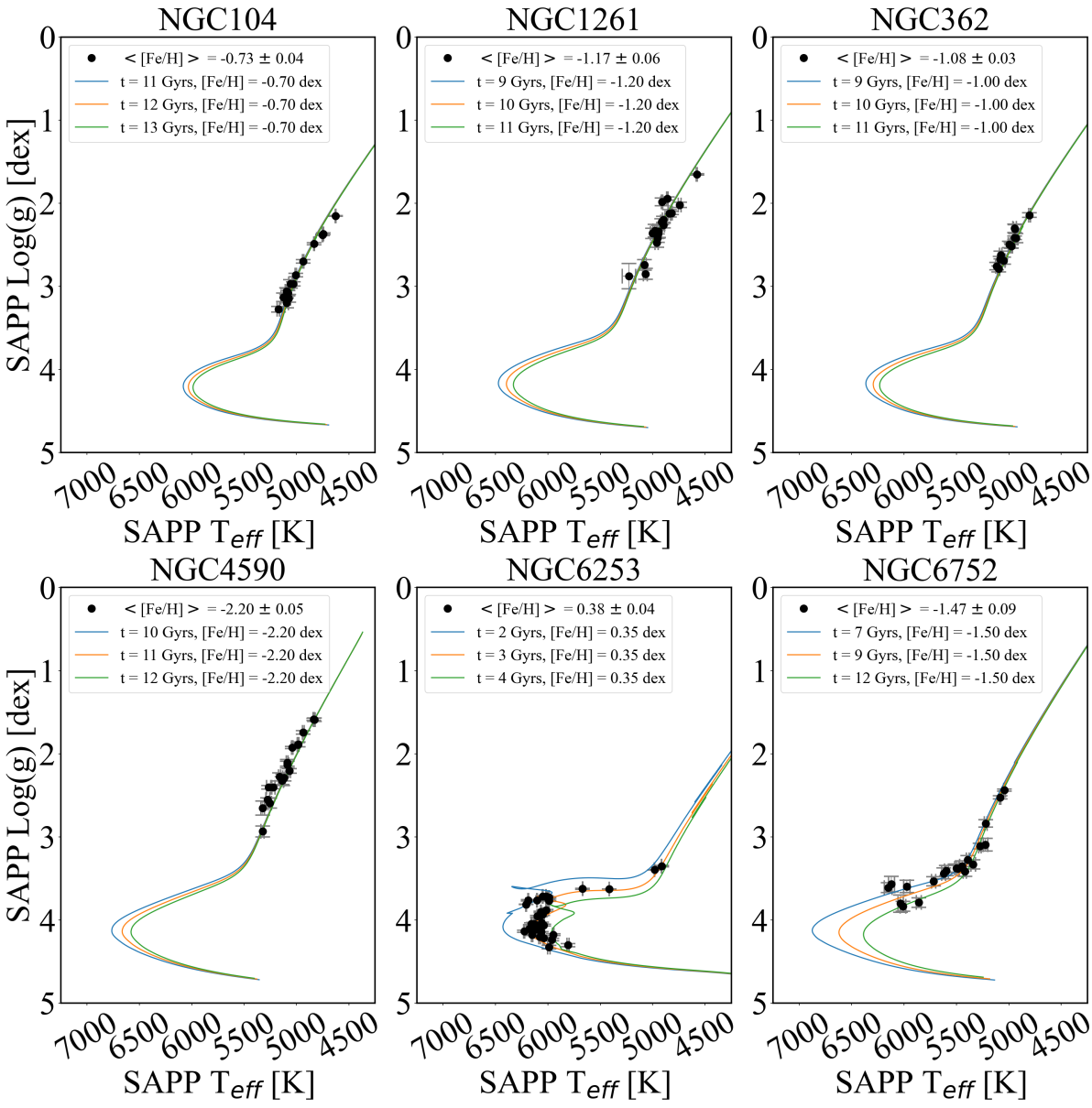

Figure 2.21: $T_{\rm eff}$-log g diagram of the Gaia-ESO clusters. Only data analysed in this work with the SAPP are shown. In each panel, the black solid circles are a star with corresponding error bars in $T_{\rm eff}$ and log g. There are three isochrones varying in age (blue youngest, orange median, green oldest) which have a metallicity close to the average [Fe/H] of the cluster.

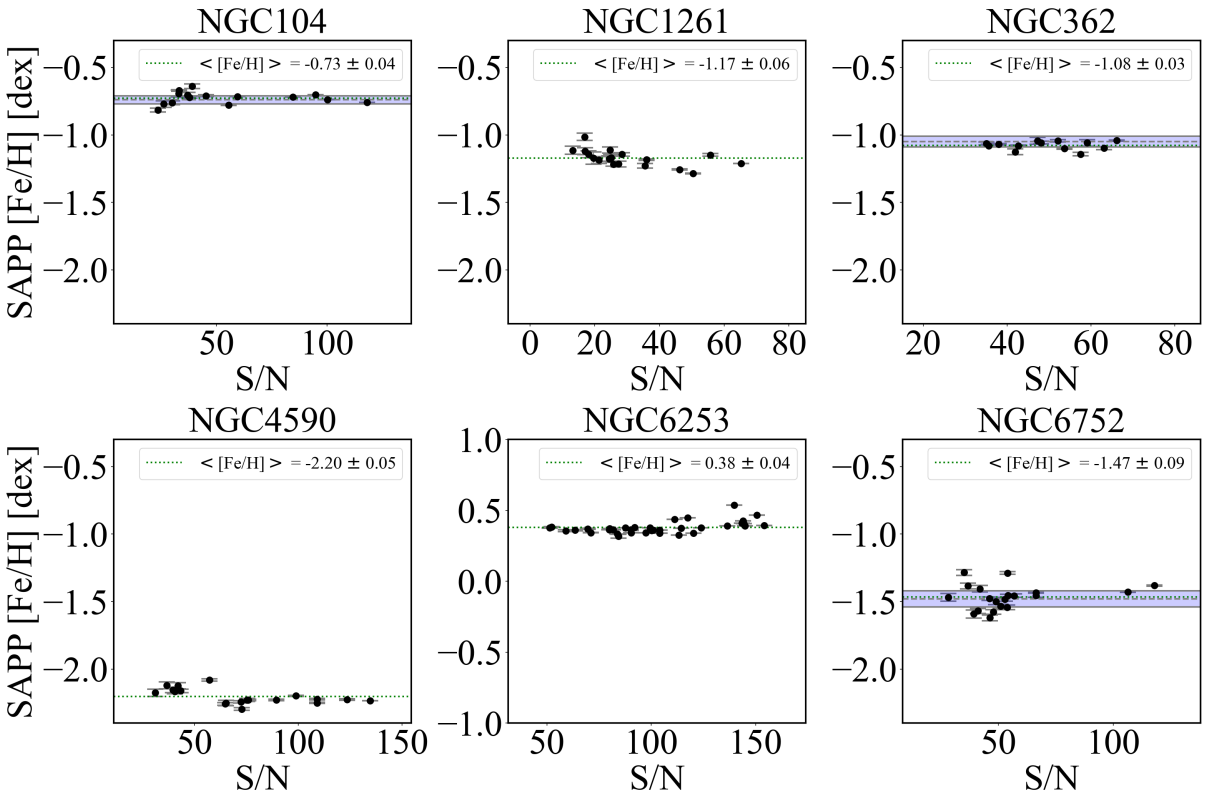

Figure 2.22: SAPP metallicities [Fe/H] of stars in clusters versus the spectral SNR. In each panel, the average (NLTE) [Fe/H] and 1σ scatter is annotated, the former being shown as the green dotted line. The grey dashed line and corresponding blue shaded region represents NLTE [Fe/H] estimates and their errors from Kovalev et al. (2019) respectively.

stars at different evolutionary stages are available. For NGC 6253 and NGC 6752, we can directly test the metallicities in red giants against our estimates obtained for main-sequence and sub-giant stars. Additionally, literature values of metallicity are available for the turnoff or sub-giant stars in NGC 104 (Carretta et al. 2004) and NGC 6253 (Maderak et al. 2015), and we use these estimates to validate our results.

Generally, the results for all six Gaia-ESO clusters are very robust (Fig. 2.21), with the $T_{\rm eff}$ and $\log g$ values being in good agreement with the isochrones. Also the intracluster metallicity variation (Fig. 2.22) is very small, consistent with expectations from previous literature estimates of metallicity. In particular, three of the clusters with NLTE metallicites were analysed in Kovalev et al. (2019) and their corresponding average [Fe/H] agree very well with our study. Furthermore, our metallicity estimates for NGC 104 and NGC 6253 are consistent with values based on non-RGB stars from Carretta et al. (2004) and Maderak et al. (2015), who obtain [Fe/H] $= -0.67 \pm 0.01 \pm 0.04$ dex and [Fe/H] $= +0.445 \pm 0.014$ dex, respectively. However, it should be noted that NLTE effects are particularly large in the atmospheres of red giants at low [Fe/H] typical of globular clusters (Kovalev et al. 2019), and most literature estimates use 1D LTE models, which is why a comparison with other studies is not meaningful. There is no systematic bias or correlation of metallicity with stellar parameters ($T_{\rm eff}$ or $\log g$) or the SNR. That suggests that our abundances are robust and do not depend on the quality of the data, at least for stellar spectra with SNR > 20. The typical [Fe/H] dispersion is about 0.03 dex (NGC 362, NGC 104, NGC 6253) to 0.06 dex (NGC 1261). Only for NGC 6752, the dispersion is a bit larger, $\sigma[{\rm Fe/H}] \approx 0.09$ dex. Whether some of this dispersion is caused by the presence of sub-giants is not clear yet (e.g. Geller et al. 2017; Giesers et al. 2019).

2.5 BO-SAPP and DO-SAPP

In the context of PLATO, the SAPP will operate in two modes: the version that will run During Operations (DO-SAPP) and the version that will be used before the mission to provide an initial characterization of all targets (Before Operations, BO-SAPP). Spectroscopy will be activated in both modes. However because of scientific and runtime considerations, it is the only module that will be activated in DO-SAPP, which overall minimizes SAPPs complexity. Thus, DO-SAPP will only rely on stellar spectra and $\log g$ priors available

from the seismic analysis of PLATO light-curves or from the granulation signal. Also, PLATO Follow-Up (FU) spectra and PLATO photometry will be used, if necessary. Unlike the current implementation of the SAPP, which uses the MAFAGS-OS model atmospheres, PLATO modules will use the MARCS 1D and Stagger 3D models combined with a newly developed NLTE version of the Turbospectrum code (Plez 2012) as inputs.

In BO-SAPP, all modules combine together into SAPP's Bayesian framework to produce best-fit parameters $T_{\rm eff}$, $\log g$, [Fe/H], chemical abundances, V_{mic}, Luminosity, etc. Currently, the code makes use of photometry, spectra, and parallaxes, whereas IRFM and SBCR techniques are used to constrain $T_{\rm eff}$ independently and to validate the spectro-photometric results. We furthermore plan to include the interferometry data.Stellar evolution models will not be used, to minimise overlap with other modules of the PLATO Stellar Analysis System (SAS) system. Furthermore, we anticipate that once the Gaia RVS spectra are available, these will be used to complement spectra from instrument archives and surveys. The details of combining different observed spectra, such as, e.g. Gaia RVS, SDSS-V, and 4MOST data, will be presented in a separate study, however, the main advantage of the SAPP is that *same* physical models and the same statistical approach will be used for the analysis of all different kinds of spectroscopic observations to maximise the consistency of the results. Photometric data will be sourced from 2MASS, SPHEREx, and other surveys.

SAPP's parameters will be used by different PLATO work-groups to determine radii, mass, and ages of stars, as well as astrophysical parameters of their orbiting planets. Therefore, very stringent requirements are posed on the accuracy of the atmospheric characterization. For example, a 2% error in $T_{\rm eff}$ translates into a 3 percent error in radius and a 5 % error in mass for a typical FGK-type un-evolved star (Serenelli et al. 2017). Owing to the complexity of PLATO algorithms and the details of work organisation within different PLATO packages, the exact scope of both branches of the SAPP pipeline may change slightly in future.

2.6 Future developments

The future improvements of the code will involve the transition to 3D convective stellar model atmospheres, but also updates to the SBCR relationship, and a module to analyse M-dwarfs based on optical and infra-red spectra. 3D

models are needed, because they provide a physically-realistic description of convective and radiative energy transport in late-type stars (e.g. Vögler et al. 2005; Nordlund et al. 2009; Freytag et al. 2012), and thereby remove the need for ad-hoc adjustable parameters (like the mixing-length, micro-turbulence, and macro-turbulence), which are used in 1D hydrostatic models. Besides, the most accurate solar photospheric abundances require 3D NLTE modelling from first principles (e.g. Lind et al. 2017; Bergemann et al. 2019; Amarsi et al. 2019; Gallagher et al. 2020).

In terms of 3D modelling, the Stagger grid (Magic et al. 2013a,b) will be used in the PLATO consortium to obtain the non-seismic stellar parameter determination, asteroseismic surface effect corrections, limb darkening, and stellar convective noise. The existing STAGGER grid has currently about 200 models with $T_{\rm eff}$ from 3500 to 7000 K (step 500 K), $\log g$ from 1.5 to 5 dex (step of 0.5 dex), metallicity from -4 to $+0.5$ dex. The grid contains also models for specific benchmark stars which are out of the nodes of the grid. The grid is currently being refined to 250 K step in $T_{\rm eff}$ and the models are run for longer time sequences to have better relaxation and more snapshots per model, i.e. more reliable time average. These models will be used to compute 3D NLTE synthetic grids computed using MULTI3D (Bergemann et al. 2021) with NLTE-Turbospectrum (Gerber et al. in prep.), and they will supersede the currently used 1D NLTE grids based on the MAFAGS-OS models (Sect. 2.3.5).

Further, we are planning to improve the calibration relationships for the SBCR module (Sec. 2.3.7). We are planning to use the data collected with the CHARA/SPICA instrument[9] (Mourard et al. 2017; Pannetier et al. 2020). With the 300m baselines of the CHARA array (ten Brummelaar et al. 2005) and the optical regime of the SPICA instrument (6500 - 8500), an angular resolution of 0.2 mas could be reached, yielding angular diameters with a precision of about 1% for several hundreds of FGK-type stars.

2.7 Conclusions

In this study, we present the SAPP pipeline for the astrophysical characterisation of FGK-type stars. The code is based on the method of Bayesian inference and it is capable of combining various sources of observational information, including but not limited to spectroscopy, photometry, parallaxes,

[9]First light expected in 2022.

and asteroseismology, along with their uncertainties. Thus, the code avoids the assumption of Gaussian uncertainties and uncorrelated variables, which is commonly used in astronomical literature.

We tested the pipeline on a sample of well-studied FGK-type stars, most of them included in the set of Gaia benchmark stars (Jofré et al. 2018), and we complemented them with a metal-poor TESS sub-giant ν Ind (Chaplin et al. 2020) and with stars from the Kepler legacy sample (Nissen et al. 2017). High- and medium-resolution spectra ($R > 40,000$ and $R = 20,000$ respectively) with high-S/N (S/N > 300) spectra for these stars are available from the ESO archives. The combined sample includes 27 FGK-type stars that cover a broad range in $T_{\rm eff}$, $\log g$, and metallicity. The majority of our benchmarks are main-sequence stars, but there are several sub-giants. The reference parameters of these targets were adopted from recent literature studies that employed asteroseismology, interferometric angular diameters, and spectrophotometry.

We find that spectroscopic data provides most the reliable information about atmospheric parameters of stars. From spectra alone, we can determine $T_{\rm eff}$, $\log g$, metallicity, and individual abundances of α- and iron-group elements with a precision of a 50 to 100 K ($T_{\rm eff}$) and 0.05 to 0.1 dex in other parameters. These parameters can be recovered from the medium-resolution (R $= 20,000$) spectra with narrow wavelength coverage in the optical. Higher-resolution or wide-band spectra would be needed to obtain reliable abundances of carbon, oxygen or rare chemical elements, such as Li or neutron-capture species.

We also find that the asteroseismic prior offers a clear improvement in the accuracy and precision of $T_{\rm eff}$ and $\log g$ estimates. This can be achieved by either using the asteroseismic scaling relationships and iterating with the spectroscopic module, or by using asteroseismic constraints as an independent likelihood in the PDF. The combined approach allows us to achieve 1% accuracy in the estimate of $T_{\rm eff}$ for all stellar types relevant to PLATO (FGK-type). M-type stars are relevant to the context of PLATO, however will be tested in future studies. The strictly spectroscopic analysis without a seismic prior yields highly biased parameters for hotter stars, with $T_{\rm eff}$ and $\log g$ estimates severely over-estimated. This bias is the consequence of the progressive loss of important lines of neutral species, which makes it difficult to break the degeneracies between $\log g$ and $T_{\rm eff}$. The SBCR and IRFM modules provide useful constraints on $T_{\rm eff}$, however, they are currently not competitive

with spectroscopy, as the precision of both methods is not better than 100 K in $T_{\rm eff}$. On the other hand, both modules deliver robust estimates of stellar radii, with the accuracy of 3 to 5% in our parameter space. With the upcoming CHARA/SPICA data we expect that the SBCR method can be improved further to reach the precision of 1 to 2% in radii.

Comparing our results computed using the SAPP pipeline with the independent values, we find that $T_{\rm eff}$ and $\log g$ estimates are recovered to better than 1%, assuming the validity of the absolute scale of the interferometric $T_{\rm eff}$ and asteroseismic $\log g$ estimates. Our NLTE estimates of metallicity ([Fe/H]), Mg, Ti, and Mn abundances agree with the NLTE estimates based on very high-resolution (HARPS, UVES) spectra to better than 0.04 dex. This precision and accuracy will help PLATO to attain its goals of 2 % in R, 15 % in mass and 10 % in age (Goupil 2017; Serenelli et al. 2017). Analysis of medium-resolution HR10 spectra of stars with asteroseismic data showed that we obtain reliable results within 5% for $T_{\rm eff}$ and $\log g$ within 1%. NLTE [Fe/H] are accurate to within 0.1 dex with [Mg/Fe] accurate to -0.03$\pm$0.07 dex. SAPP was tested on spectra of stars in six open and globular clusters for an independent assessment of the pipeline. Out of the six, three have been analysed by Kovalev et al. (2019) for the determination of NLTE [Fe/H] and abundances, which agree very well with our study. Our results of the six clusters in general are robust and present little scatter with respect to stellar atmospheric parameters ($T_{\rm eff}$, $\log g$, [Fe/H]). Spectra of this resolution and quality are expected from future facilities, such as 4MOST (e.g Bensby et al. 2019; de Jong et al. 2019) and WEAVE (e.g. Dalton et al. 2014).

Finally, we note that although in this work our focus is on PLATO, the SAPP pipeline is versatile enough to provide astrophysical parameters for other types of stars, such as red giants, M dwarfs, etc. Kovalev et al. (2019) presented comprehensive tests and validation of the NLTE spectroscopic module on high- and medium-resolution spectra of evolved and un-evolved stars across a broad range of metallicities $-2.5 \lesssim$ [Fe/H] $\lesssim +0.3$, effective temperatures $4000 \lesssim T_{\rm eff} \lesssim 7000$ K, and surface gravities $1.2 \lesssim \log g \lesssim 4.6$ dex. The advantages of combining spectra, photometry, astrometry, and stellar models to derive ages and masses of evolved stars were carefully explored by Serenelli et al. (2013) and Schönrich & Bergemann (2014). We therefore conclude that the SAPP code delivers robust estimates of stellar astrophysical parameters, which makes the code useful for the analysis of low-mass stars observed with different large-scale spectroscopic surveys, such as 4MOST

and WEAVE (e.g. Dalton et al. 2014; Bensby et al. 2019).

Table 2.2: Final estimated parameters of benchmark stars

Star ID	$T_{\rm eff}$ K	$\log g$ dex	[Fe/H] dex	Mass $M_\odot$	Age Gyrs	Radius $R_\odot$	Luminosity $L_\odot$	[Mg/Fe] dex	[Ti/Fe] dex	[Mn/Fe] dex
18 Sco	5833 ± 37	4.44 ± 0.01	0.06 ± 0.02	1.04 ± 0.05	3.21 ± 0.63	1.02 ± 0.03	1.08 ± 0.16	-0.01 ± 0.03	0.03 ± 0.02	-0.02 ± 0.03
α Cen A	5852 ± 37	4.31 ± 0.01	0.30 ± 0.02	1.14 ± 0.05	4.73 ± 0.63	1.23 ± 0.03	1.60 ± 0.16	-0.04 ± 0.03	-0.03 ± 0.02	-0.02 ± 0.03
α Cen B	5246 ± 37	4.53 ± 0.01	0.24 ± 0.02	0.94 ± 0.05	4.18 ± 0.64	0.87 ± 0.03	0.51 ± 0.16	0.09 ± 0.03	0.08 ± 0.02	-0.00 ± 0.03
β Hyi	5840 ± 37	3.96 ± 0.01	-0.04 ± 0.02	1.16 ± 0.05	6.15 ± 0.63	1.86 ± 0.03	3.62 ± 0.16	0.01 ± 0.03	-0.03 ± 0.02	-0.11 ± 0.03
β Vir	6089 ± 37	4.11 ± 0.01	0.22 ± 0.02	1.30 ± 0.05	3.81 ± 0.63	1.66 ± 0.03	3.41 ± 0.16	-0.13 ± 0.03	-0.13 ± 0.02	-0.16 ± 0.03
δ Eri	5061 ± 37	3.80 ± 0.01	0.10 ± 0.02	1.17 ± 0.05	7.10 ± 0.64	2.24 ± 0.03	2.96 ± 0.16	0.14 ± 0.03	-0.01 ± 0.02	-0.08 ± 0.03
η Boo	6082 ± 37	3.80 ± 0.01	0.32 ± 0.02	1.66 ± 0.05	2.27 ± 0.63	2.67 ± 0.03	8.75 ± 0.16	0.04 ± 0.03	-0.09 ± 0.02	-0.06 ± 0.03
HD 49933	6730 ± 37	4.22 ± 0.01	-0.34 ± 0.02	1.26 ± 0.05	2.04 ± 0.63	1.44 ± 0.03	3.82 ± 0.16	0.06 ± 0.03	0.00 ± 0.02	-0.17 ± 0.03
Procyon	6583 ± 47	3.99 ± 0.01	0.04 ± 0.03	1.49 ± 0.05	2.23 ± 0.63	2.05 ± 0.03	7.09 ± 0.24	0.02 ± 0.04	-0.06 ± 0.02	-0.16 ± 0.03
Sun	5803 ± 37	4.44 ± 0.01	0.02 ± 0.02	1.02 ± 0.05	3.89 ± 0.63	1.01 ± 0.03	1.03 ± 0.16	-0.01 ± 0.03	0.01 ± 0.02	-0.03 ± 0.03
KIC 10162436	6289 ± 37	3.97 ± 0.01	-0.04 ± 0.02	1.36 ± 0.05	3.17 ± 0.63	2.00 ± 0.03	5.63 ± 0.16	-0.03 ± 0.03	0.02 ± 0.02	-0.05 ± 0.03
KIC 10644253	6111 ± 37	4.41 ± 0.01	0.14 ± 0.02	1.18 ± 0.05	0.88 ± 0.63	1.12 ± 0.03	1.58 ± 0.16	-0.03 ± 0.03	0.02 ± 0.02	-0.02 ± 0.03
KIC 12069424	5842 ± 37	4.29 ± 0.01	0.10 ± 0.02	1.08 ± 0.05	6.31 ± 0.63	1.23 ± 0.03	1.58 ± 0.16	0.03 ± 0.03	0.03 ± 0.02	-0.02 ± 0.03
KIC 12069449	5811 ± 37	4.36 ± 0.01	0.06 ± 0.02	1.04 ± 0.05	5.95 ± 0.63	1.12 ± 0.03	1.28 ± 0.16	0.03 ± 0.03	0.04 ± 0.02	-0.00 ± 0.03
KIC 12258514	6026 ± 37	4.12 ± 0.01	0.02 ± 0.02	1.18 ± 0.05	5.30 ± 0.63	1.57 ± 0.03	2.91 ± 0.16	-0.01 ± 0.03	0.01 ± 0.02	-0.02 ± 0.03
KIC 3427720	6086 ± 37	4.39 ± 0.01	0.00 ± 0.02	1.12 ± 0.05	2.33 ± 0.63	1.12 ± 0.03	1.55 ± 0.16	0.00 ± 0.03	0.02 ± 0.02	-0.02 ± 0.03
KIC 6106415	6002 ± 37	4.30 ± 0.01	0.01 ± 0.02	1.08 ± 0.05	5.21 ± 0.63	1.22 ± 0.03	1.74 ± 0.16	-0.07 ± 0.03	0.02 ± 0.02	-0.07 ± 0.03
KIC 6225718	6207 ± 37	4.31 ± 0.01	-0.10 ± 0.02	1.12 ± 0.05	3.34 ± 0.63	1.22 ± 0.03	1.98 ± 0.16	-0.04 ± 0.03	0.02 ± 0.02	-0.11 ± 0.03
KIC 7940546	6305 ± 37	4.00 ± 0.01	-0.13 ± 0.02	1.32 ± 0.05	3.27 ± 0.63	1.90 ± 0.03	5.14 ± 0.16	-0.01 ± 0.03	0.01 ± 0.02	-0.10 ± 0.03
KIC 9139151	6130 ± 37	4.38 ± 0.01	0.10 ± 0.02	1.16 ± 0.05	1.81 ± 0.63	1.15 ± 0.03	1.68 ± 0.16	-0.07 ± 0.03	0.01 ± 0.02	-0.04 ± 0.03
ν Ind	5361 ± 37	3.44 ± 0.01	-1.39 ± 0.02	0.83 ± 0.05	10.98 ± 0.64	2.87 ± 0.03	6.12 ± 0.17	0.27 ± 0.03	0.27 ± 0.02	-0.30 ± 0.03

The results of our full Bayesian analysis for the primary parameters $T_{\rm eff}$, $\log g$, and [Fe/H]. The Star IDs correspond exactly to the stars in table 2.1. For each parameter, the uncertainty corresponds to the total error, computed by combining the statistical and systematic uncertainty in quadrature.

Chapter 3

Chemo-dynamical overview of the Milky Way disc through Gaia-ESO

Abstract

Aims. Our goal is to investigate the chemical, temporal, and kinematical structure of the α-poor and α-rich populations in the Galactic disc.
Methods. We employ the medium-resolution spectra from the Gaia-ESO large spectroscopic survey, as well as Gaia EDR3 astrometry and photometry. The stellar parameters and chemical abundances are determined using Non-Local Thermodynamic Equilibrium (NLTE) models of synthetic spectra. Ages are computed for a large sample of subgiants using `Garstec` evolutionary tracks.
Results. We find evidence of a kinematically cold metal poor alpha poor disc in the $[\alpha/\mathrm{Fe}]$ distributions in the local volume. Of which a sub-sample of older stars exist from this disc within a temporal overlap which could be explained by co-evolution of the thick and thin disc. These distributions are characterised by well defined trends in the space of age- and kinematic (V_{ϕ})[1].

3.1 Introduction

Over the past decade, tremendous progress has been made in understanding the structural properties of our galaxy. A combination of data from large-scale photometric, spectroscopic, and astrometric stellar surveys, such as the Gaia-ESO, LAMOST, GALAH, APOGEE allowed robust constraints on the temporal variability of chemical enrichment across the Galactic disc, bulge,

[1]This chapter has been adopted from my second submitted paper which is in referee process, the first submitted version: https://ui.adsabs.harvard.edu/abs/2022arXiv220610949G/abstract

and the halo (e.g. Bland-Hawthorn & Gerhard 2016b; Barbuy et al. 2018; Helmi 2020). Complemented with accurate positions and kinematics of stars from the Gaia space mission (Gaia Collaboration et al. 2016, 2018, 2020), it has become possible to constrain the detailed chemo-dynamical evolution of these stellar populations and to gain new insights into their origins.

Still, the structure and evolution of the Galactic disc remains one of the most complex problems in studies of Galaxy formation. Since the discovery of the thick disc (Gilmore & Reid 1983), much work focused on the bi-modality in the space of chemical abundances (e.g. Bensby et al. 2005; Reddy et al. 2006; Recio-Blanco et al. 2014; Duong et al. 2018). Many studies based on stars in the solar neighbourhood and beyond pointed out the existence of two populations, $[\alpha/\mathrm{Fe}]$-rich and $[\alpha/\mathrm{Fe}]$-poor, partly overlapping in metallicity (e.g. Fuhrmann 1998; Nidever et al. 2014), age (e.g. Bensby et al. 2014; Feuillet et al. 2019), and kinematics (e.g. Ruchti et al. 2011; Lee et al. 2011; Kordopatis et al. 2011; Hayden et al. 2015). These stellar populations have been deemed as the "thin" and the "thick" disc, and their morphological parameters have since then been subject of a major interest (Bland-Hawthorn & Gerhard 2016b). First, it has been shown different physical processes may influence the formation and evolution of sub-structure in the disc, including multiple infall (e.g. Chiappini et al. 1997; Spitoni et al. 2019), radial migration (e.g. Schönrich & Binney 2009b,d; Loebman et al. 2011; Minchev et al. 2013) and radial mixing caused by satellites (Quillen et al. 2009), growth induced by mergers (e.g. Villalobos & Helmi 2008; Read et al. 2008; Villalobos et al. 2010), gas-rich accretion and mergers (e.g. Brook et al. 2004; Stewart et al. 2009; Grand et al. 2018; Buck 2020), local gas instabilities associated with turbulence (Bournaud et al. 2009), dynamical interaction with cold dark matter sub-halos (Hayashi & Chiba 2006; Kazantzidis et al. 2009), galactic winds (Moster et al. 2012), and early outflows (Khoperskov et al. 2021). It has also been demonstrated that the chemical bi-modality is a relatively rare phenomenon in L^* galaxy discs (Mackereth et al. 2018; Gebek & Matthee 2021). More recent studies address in more detail the spatial variability of the bi-modality (Hayden et al. 2015; Bovy et al. 2016; Nandakumar et al. 2020), finding that $[\alpha/\mathrm{Fe}]$-rich component is more centrally concentrated, whereas the $[\alpha/\mathrm{Fe}]$-poor component has a larger radial extent (Haywood et al. 2019; Sahlholdt et al. 2022). Both stellar populations appear to be well-mixed dynamically, which implies that a robust decomposition of the two based on their phase-space is not possible. Therefore, the question of whether the popula-

tions are indeed distinct stellar components with a separate formation history still remains open.

The main difficulty in this work, so far, has been the limited observational information - not in a sense of data quantity, but in the sense of chemo-dynamical parameter coverage -, combined with a complex selection function of different observational surveys (e.g. Bergemann et al. 2014; Stonkutė et al. 2016; Nandakumar et al. 2017). The observing strategy of the GALAH survey is such that the majority of stars belong to the thin disc (Duong et al. 2018), and the population statistics of objects with chemical properties of the thick disc is very incomplete. The APOGEE survey is also magnitude-limited, therefore the samples are biased to relatively metal-rich stars in the range $-0.5 \lesssim$ [Fe/H] $\lesssim 0.3$ (Hayden et al. 2015), also the ages are less reliable at [Fe/H] < -0.5 because of the paucity of metal-poor stars in the training samples (Lian et al. 2020). The LAMOST stellar survey of the Galaxy has a deeper spatial coverage compared to GALAH and APOGEE (Xiang et al. 2019), however, the accuracy of chemical composition is limited and does not allow to resolve the sub-structure in the chemical abundance plane and to identify small gradients associated with different formation scenarios and chemical enrichment sites.

In this work, we perform of a detailed analysis of the chemical, temporal, and kinematical distribution functions using the spectroscopic data from the Gaia-ESO large spectroscopic survey, astrometry from the Gaia early Data Release (EDR3), and stellar ages. Similar work was presented by Feuillet et al. (2019) and Lian et al. (2020) using the infra-red spectra from the APOGEE survey. In our work, we furthermore make an attempt to quantify the temporal evolution of the α-poor and α-rich populations, using a large sample of subgiants with accurate age estimates.

The paper is organised as follows, in Sect. 3.2 we discuss the observational sample. Sect. 3.3 outlines the approach used for the determination of stellar parameters and chemical abundances. In Sect. 3.5, we briefly state how the ages are determined. The results are presented in Sect. 3.7, where we focus on the distributions of chemical abundances, combined with kinematics and ages. Further, we discuss the results in the context of previous observational and theoretical findings, and we close the paper with conclusions in Sect. 3.8.

3.2 Observed data

In this work, we rely on targets observed within the Gaia-ESO large spectroscopic survey (Gilmore et al. 2012a; Randich et al. 2013). In the latest public data release (DR4), spectra for over 10^5 are available, and we use all spectra taken with the HR10 setting of Giraffe spectrograph[2]. The HR10 data are available for 55,761 stars. The signal-to-noise (SNR) distribution of the sample is very broad and ranges from 2 to a few 100 per pixel.

Fig. 3.1 shows the targets in the photometric colour-magnitude (CMD), J versus J - K_s, plane, where J and K_s are VISTA photometric filters (McMahon et al. 2013). The apparent regular distribution is caused by the photometric selection of targets in the input Gaia-ESO catalogue. For the Giraffe catalogue, the following basic selection scheme was used: $0.00 \leq (J - K_s) \leq 0.45$ and $14.0 \leq J \leq 17.5$ for the blue box, and $0.40 \leq (J - K_s) \leq 0.70$ and $12.5 \leq J \leq 15.0$ for the red box. The boxes were defined to maximise the probability of observing targets in all Galactic components, the discs and the halo, therefore the target densities vary drastically, and to account for this effect, the boxes were slightly extended in order to optimise the fiber occupancy in each field. In particular, in the fields, where number of targets exceeded the number of fibers - as in low latitude fields -, additional selection criteria were used, such as shifting the boxes by the mean value of extinction in a given field 0.5 E(B - V). This procedure leads to a characteristic spread of the distribution along the x-axis, as seen in Fig. 3.1. The relative distribution is such that the majority of targets (80 %) are in the blue box, whereas stars in the red box account for about 20 % of the sample. The blue box targets include main-sequence, turnoff, and subgiant stars, and the red box was optimised for red clump stars, however because of the extension of the boxes a certain overlap exists. For the detailed description of the selection, we refer to Stonkutė et al. (2016). This selection implies that most targets in the Gaia-ESO HR10 sample are rather faint, $14 \gtrsim G_{mag} \lesssim 17$, compared to other surveys such as RAVE, APOGEE, or GALAH.

We complement these data with the proper motions, photometry, and extinction from the EDR3 Gaia catalogue (Gaia Collaboration et al. 2020). The cross-match between every Gaia-ESO spectrum and Gaia ED3 catalogue was performed on grounds of angular position within a 1.0 arcsec tolerance (cone search). Distances and their uncertainties were adopted from Bailer-Jones

[2]The NLTE grids employed in this work cover the corresponding wavelength regime

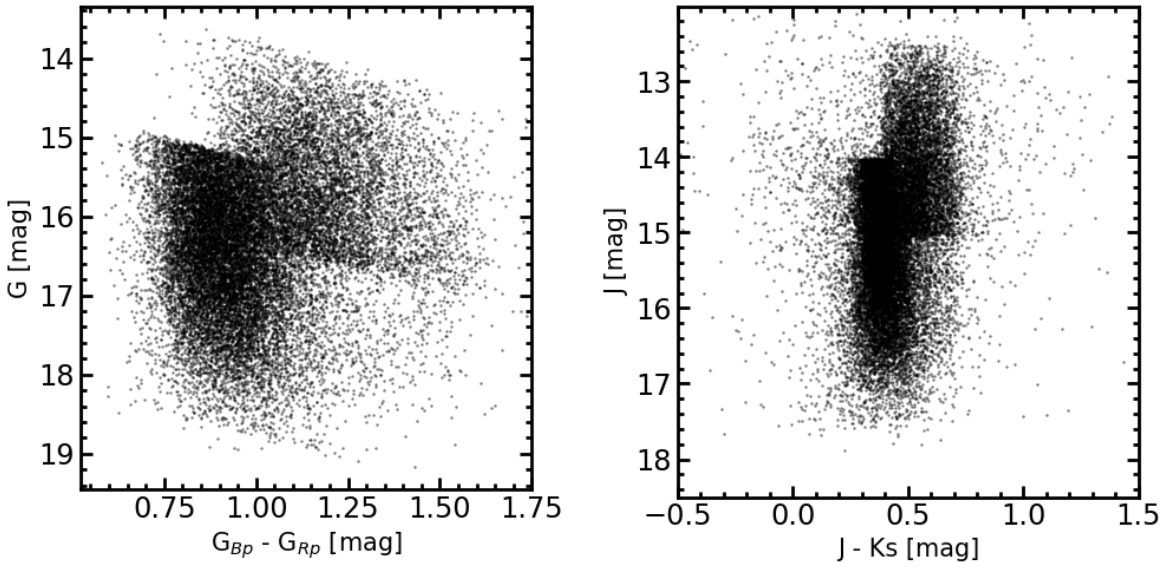

Figure 3.1: Photometry of the observed sample. Left panel shows the distribution in the Gaia magnitudes, G vs G_{Bp} - G_{Rp}. Right panel shows the distribution in the VHS magnitudes, J vs J - K_s (see Sect. 2).

et al. (2021). The spatial distribution of the sample is shown in Fig. 3.2. Most of these objects are confined closer to the plane with altitudes of up to 2 kpc and they probe a range of Galactocentric radii from $\sim$ 5 to 12 kpc. The 3D space velocities[3] for the sample are calculated using the Python package 'astropy' (Astropy Collaboration et al. 2013; Price-Whelan et al. 2018). The accuracy of the astrometric information is high enough to yield the velocities with the uncertainty of $\lesssim 5$ kms^{-1}.

[3]In this work, we use galactocentric cylindrical coordinate system. So that V_r, V_ϕ, V_z are the components of the full 3D space velocity pointing towards Galactic center R, in the direction of rotation ϕ, and vertically relative to the disc mid-plane, respectively.

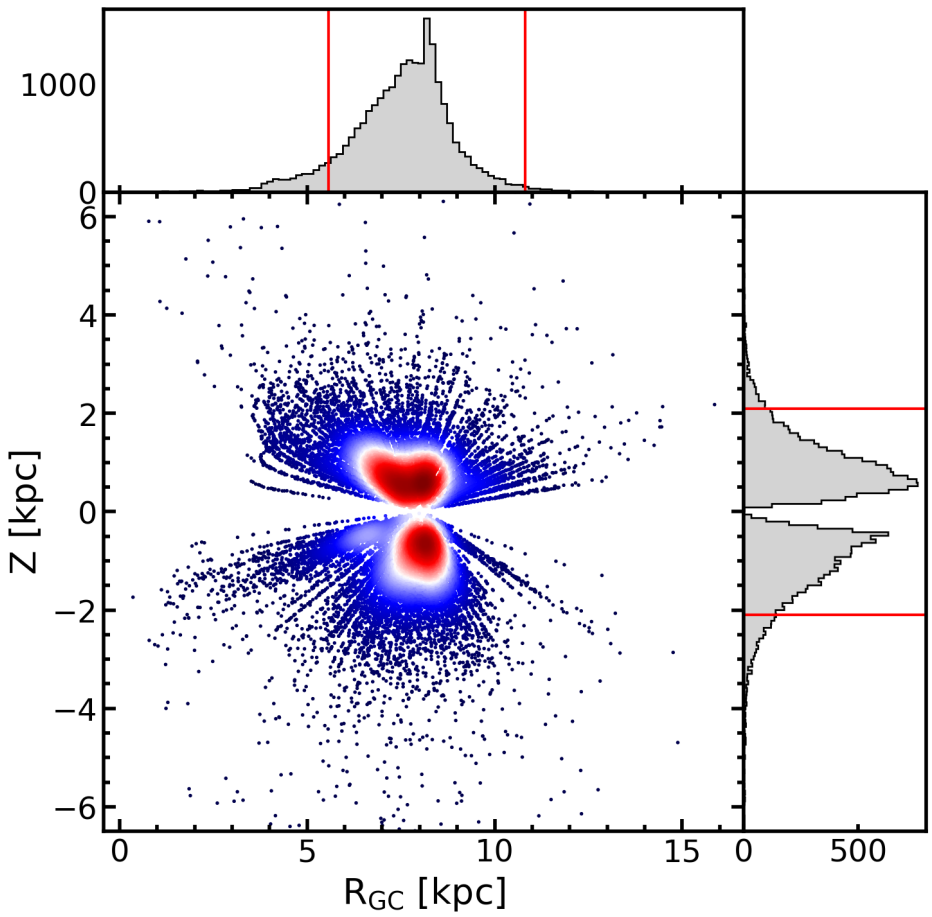

Figure 3.2: Spatial distribution of the observed sample. The vertical axis represents the height above the disc plane in kpc and the horizontal represents the Galactocentric radius in kpc. The colour scale shows normalised density from 0.07% (dark blue) to 100% (dark red).

3.3 Stellar parameters

The homogeneity, accuracy, and precision of stellar parameters is essential given by the scientific goals of this study. However, our analysis of the Gaia-ESO sixth internal data release (iDR6)[4] (Gilmore et al. 2012a; Randich et al. 2013) show artificial ridges and bifurcations in the space of stellar parameters and their uncertainties. It suffers from some loss of precision owing to the complex homogenisation and cross-calibration procedure employed. Therefore, this does not allow for a robust analysis of the distribution functions in the space of astrophysical parameters and ages.

We have therefore opted to re-analyse the spectra using the Bayesian SAPP pipeline described in Gent et al. (2022). This method was shown to provide atmospheric parameters, including $T_{\rm eff}$, $\log g$, [Fe/H], and abundances (Mg,

[4] https://www.gaia-eso.eu/

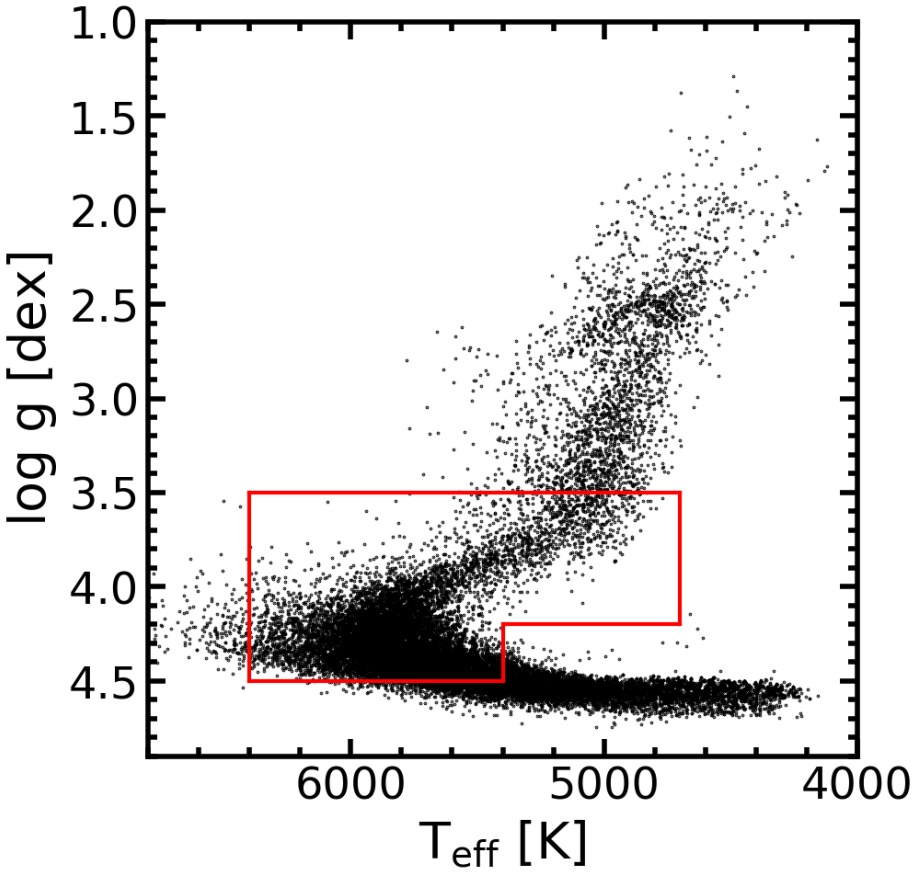

Figure 3.3: The distribution of the observed sample in the $T_{\rm eff}$-$\log g$ plane. The targets enclosed within the red box represent the sample used for the analysis of ages.

Ti, Mn), across a broad range of stellar parameters: $4000 \lesssim T_{\rm eff} \lesssim 7000$ K, $1.2 \lesssim \log g \lesssim 4.6$ dex, and $-2.5 \lesssim$ [Fe/H] $\lesssim +0.6$ dex. Extensive tests of the NLTE synthetic spectral grids and the Payne model (Ting et al. 2019) based on these can be found in Kovalev et al. (2019). The latter study also presented a detailed spectroscopic analysis of the benchmark stars, including main-sequence stars, subgiants, and red giants, and 742 stars probing the entire evolutionary sequence in 13 open and globular clusters. In Gent et al. (2022), the code was developed to carry out the full Bayesian analysis, by combining the probabilities obtained from the spectroscopy, photometry, astrometry, and asteroseismic data analysis modules.

The results of the SAPP analysis are shown in Fig. 3.3, where the entire Gaia-ESO HR10 sample with SNR > 20 is plotted in the $T_{\rm eff}$-$\log g$ plane. The characteristic uncertainties of stellar parameters are of the order 22 K for $T_{\rm eff}$, 0.043 dex for $\log g$, 0.025 dex for [Fe/H], 0.049 dex for [Mg/Fe], and 16% for age. These uncertainties represent the combined estimates derived from

the shape of the multi-dimensional posterior PDF, and thus, they account for the statistical uncertainties (those of the observed data) and for the systematic (differences between the individual PDFs derived from the photometric, astrometric, and spectroscopic data). For more details on the error analysis, we refer the reader to Gent et al. (2022).

3.4 Selection function

In order to assess the influence of the survey selection function on our data set, we followed the methodology of Bergemann et al. (2014) and Thompson et al. (2018). To ensure self-consistency in the analysis, the same evolutionary tracks were used (Sect. 3.5). Firstly, a complete population of stars has been generated assuming the Salpeter initial mass function (IMF), a constant star formation rate (SFR), and a uniform and age-independent metallicity [Fe/H] distribution. The distribution exhibits a trend, which reflects simply the IMF and the stellar evolution lifetime, that is shorter at lower [Fe/H] and same mass. We then remove stars outside the $T_{\rm eff}$-$\log g$ box used in our analysis (Sect. 3.3). In the second step, this Mock dataset is used to determine the completeness fraction by calculating the ratio of photometrically selected targets relative to the complete sample. This is done separately for the blue and red photometric boxes.

Figure 3.4 shows for a given distance of 1 kpc, the relative stellar density (left) and completeness (right) of the Mock stellar population from the red and blue selection boxes. The distance was chosen as representative of the bulk fraction of stars in the observed Gaia-ESO sample, but careful inspection of the simulated fractions suggests that the distribution is qualitatively similar at distances at 0.5 kpc or 2 kpc. It can be concluded that the distribution of stars in the age-metallicity plane suffers from a systematic bias, which is primarily caused by the colour cuts adopted in the Gaia-ESO survey. These cuts lead to a very pronounced depletion in the fraction of young stars with ages $\lesssim$ 7 Gyr, although the effect slightly depends on metallicity. The red box additionally skews the distribution towards old metal-rich stars, whereas the blue box is primarily sensitive to old metal-poor stars. This situation is rather similar to the completeness for the Gaia-ESO UVES sample described by Bergemann et al. (2014) and Thompson et al. (2018).

We conclude that the distribution of our Gaia-ESO HR10 sample is thus preferentially skewed towards older populations with slightly sub-solar metallici-

ties.

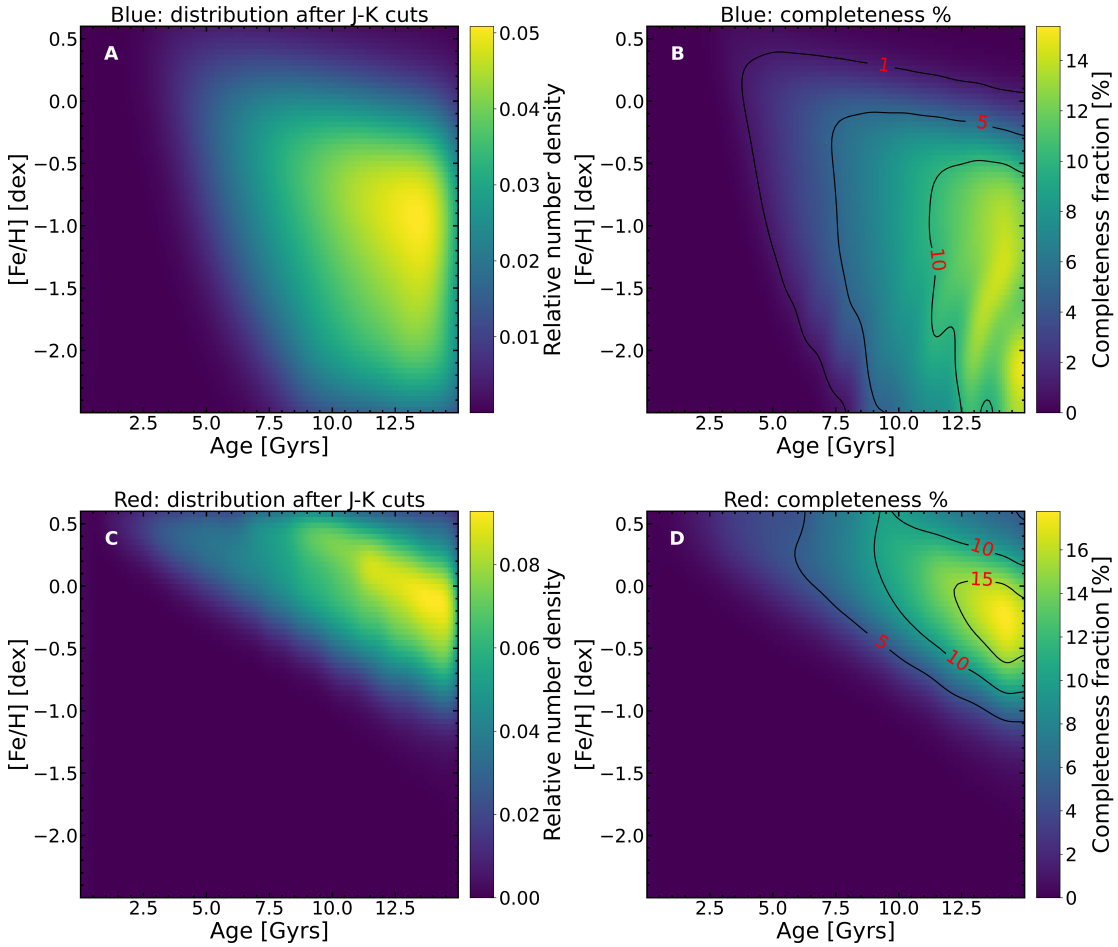

Figure 3.4: Synthetic stellar population to simulate the selection effect of Gaia-ESO survey and of the observed stellar sample. Here the results of the simulation at 1 kpc are shown for the blue box (top row) and red box (bottom row) as defined in Sect. 3.2. Right: the completeness fraction, defined as the ratio of stars with cut to the number of stars without cut, i.e. the larger the number the more stars are retained in the population after applying the colour cuts (Sect. 2). In case of no bias, the completeness fraction is unity 1.

3.5 Stellar ages

One important component of this study is the availability of ages. Ages are derived using the Bayesian pipeline BeSPP presented in Serenelli et al. (2013), which was also applied to the analysis of the first Gaia-ESO data release in Bergemann et al. (2014). The code relies on the GARSTEC grid of stellar evolutionary tracks (Weiss & Schlattl 2008) (also used in SAPP) that covers the mass range from 0.6 to 5.0 $M_{\odot}$ with a step of 0.02 $M_{\odot}$ and metallicity from -2.50 to $+0.60$ with a step of 0.05 dex. The average fractional uncer-

tainty of ages is approximately 11% (0.7 Gyrs) with 85 % of the stars with fractional uncertainties less than 15%.

The analysis of ages is limited to subgiants and upper main-sequence stars (including turn-off, TO), because of the strong degeneracy typically identified between tracks of different ages and metallicities for the lower MS and RGB phases. This selection is made by limiting the effective temperature and surface gravity to: 4700 - 6700 K, 3.5 - 4.5 dex for subgiants and turn-off stars, and 5400 - 6700 K, 3.5 - 4.2 dex for the upper main-sequence. We also include the stars with accurate abundances and ages analysed in Bergemann et al. (2014). These stars are part of the Gaia-ESO sample. We further limit our sample with a maximum of 0.1 dex in [Fe/H] error and 30% in age error. The uncertainties of stellar parameters however are small enough to ensure that our selection retains most of the subgiants in the sample and it minimises the contamination by lower main-sequence stars. Our stellar sample with ages thus contains 4 406 stars, all of have a complete kinematic characterisation. This sample we label as the "Chronos" sub-sample. The next section we describe the validation of our stellar parameters and ages to finalise the quality-controlled Chronos sub-sample.

3.6 Validation of stellar parameters and ages

The quality is stellar parameters is important within the scope of this paper. In Paper 1 (Gent et al. 2022), we presented a careful validation of our stellar analysis pipeline and its outputs (including metallicities, masses, and ages), using a sample of benchmark stars with independently determined stellar parameters, including interferometic $T_{\rm eff}$ and ages constrained by asteroseismology. We showed that a combination of spectroscopy, astrometry, and photometry in the Bayesian framework yields metallicites accurate to 0.02 dex and ages with the precision of ~ 0.6 and accuracy of ~ 1 Gyr, in line with results of similar earlier studies (e.g. Serenelli et al. 2013; Schönrich & Bergemann 2014). Whereas the focus of our work in Paper 1 was on main-sequence stars and subgiants, and the same type of observational information, that is the Gaia-ESO spectra, Gaia photometry and astrometry, was employed, the difference with respect to present study is the use of global asteroseismic quantities that are not available for the majority of stars in the present sample.

Therefore, here we present additional tests in order to investigate the properties of data errors in the parameter space that is relevant to our conclusions.

Table 3.1: Sensitivity of the Bayesian stellar parameters for the Chronos sub-sample:
In the first row we provide the results obtained using the IRFM $T_{\rm eff}$ instead of the spectro-photometric estimates.
In the second row, we tabulate the results obtained by systematically shifting the distances by $\pm$10% (as the analysis is limited to stars with uncertainties less than 10%). In the third row shows the largest bias and scatter for a given metallicity regime between BeSPP ages and ages calculated with J, Ks 2MASS photometry via Xiang & Rix (2022). In the fourth row, the comparison between BeSPP - SAPP age scales of the final validated sample gives an average difference and standard deviation, with an average error of 0.6 Gyrs

	Δ[Fe/H] dex	$\Delta T_{\rm eff}$ K	$\Delta \log g$ dex	age Gyr
IRFM $T_{\rm eff}$	0.01 $\pm$0.04	16 $\pm$52	-0.06 $\pm$0.14	-
d $\pm$ 10%	0.00 $\pm$0.02	2 $\pm$12	0.00 $\pm$0.08	-
J, K_s	-	-	-	0.9 $\pm$2.2
BeSPP - SAPP	-	-	-	0.5 $\pm$0.4

First, we carry out the analysis of atmospheric parameters of stars using the infra-red flux (IRFM) method (Casagrande et al. 2010b, 2021b). The results obtained by applying the IRFM technique to our main sample are provided in Table 3.1. The effective temperatures are in agreement with the reference SAPP values to 16 ± 52 K, whereas the resulting surface gravities and metallicities change by -0.06 ± 0.14 dex and 0.01 ± 0.04 dex, respectively, if $T_{\rm eff}$ is derived from IRFM instead of spectroscopy.

We also investigate the quality of surface gravities calculated by the SAPP by applying a systematic shift to distances that are adopted from (Bailer-Jones et al. 2021). The shift was estimated through the analysis of typical uncertainties of distances: the average distance error in our sample is of the order 8 % pc with the majority of stars having the error of $\sim 5\%$. The resulting stellar parameters calculated with the offset distances are also provided in Table 3.1. The shift has no significant effect on Teff, with the average difference of 2 K and a scatter 12 K, whereas surface gravities and metallicities are affected at the level of 0.00 ± 0.08 and 0.00 ± 0.02, respectively.

In the third step, we explore the sensitivity of ages to stellar parameters by performing the analysis of ages calculated self-consistently within the Bayesian framework versus the approach presented in Xiang & Rix (2022), where only K_s magnitudes are used circumventing the surface gravities. In the latter case, we make uses of either K_s or K_s and J magnitudes using the synthetic photometry associated with evolutionary tracks. We do not change $T_{\rm eff}$ or metallicity scales, owing to their negligibly small sensitivity to the input data (Table 3.1.

We find that the effect on ages is maximum at slightly sub-solar metallicities, with the bias and scatter of $\sim$ 0.9 Gyr and $\sim$ 2.2 Gyr, respectively. Surprisingly, more metal-poor stars (that are also preferentially old), [Fe/H] $\lesssim -0.7$ dex, are least affected by the approach, with the age bias of only 0.3 Gyr and scatter of 1.4 Gyr. From this comparison, we can cut the stars within a fraction of the standard deviation obtaining stars which are consistent with BeSPP. We chose an absolute difference $\pm$ 1 Gyrs for the internal age scales (approximately half of the average standard deviation), reducing the number of stars within the Chronos sample to 3100. By selecting stars which agree to within 1 Gyr of these two age scales, we are left with an *externally* validated sample.

Finally, we compare the ages obtained using BeSPP with the age estimates internally by the SAPP. Since the codes assume a similar algorithm, the same input data and evolutionary tracks, this comparison only demonstrates the *internal* precision of ages. We find the both codes are in excellent agreement, with 0.5 Gyr bias and a scatter of 0.4 Gyr only. Selecting stars which agree between BeSPP and SAPP within 1 Gyr (identical cut to external comparison), we are left with an *internally* validated sample. This final step results in an average precision in fractional age error (accounting for the variance from external, then internal cuts) of 10 % for BeSPP and 11 % for SAPP, reducing the number of stars within the Chronos sub-sample to 2898.

This final set of ages can now confidently be used in future sections and from now on are referred to as calibrated Chronos ages. The age scale we will use in particular will be from BeSPP which uses $T_{\rm eff}$, $\log g$, and [Fe/H] from SAPP.

3.7 Results and Discussion

3.7.1 Chemical abundances

The [Mg/Fe] abundance ratios of our sample against metallicity are shown in Fig.3.5. Here we limit the analysis to the abundance of Mg, because no particular sub-structure is visible in the distribution of Ti or Mn abundance ratios.

As previous studies showed, we also see a prominent bi-modality in the [Mg/Fe] abundance ratios, which is manifested as two over-densities separated at [Mg/Fe]

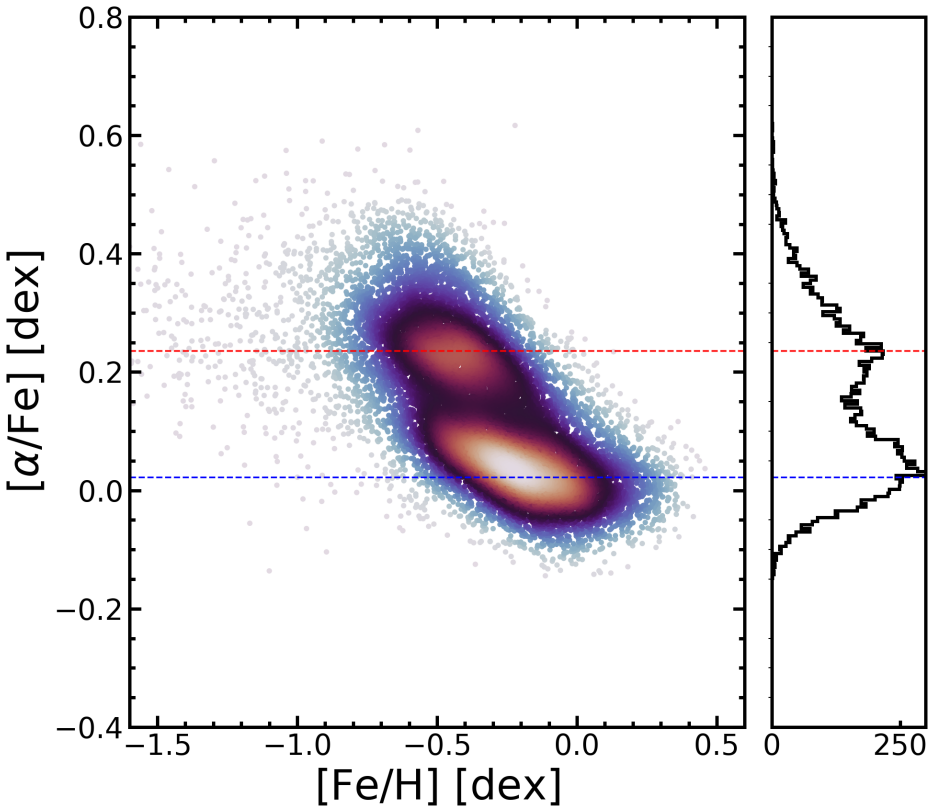

Figure 3.5: The densities of NLTE abundances of [α/Fe] (traced by Mg) as a function of [Fe/H]. The dashed lines represent the average [α/Fe] value for stars which are α-rich (red) and α-poor (blue).

$\approx +0.15$ dex across the entire metallicity range, $-1.5 \approx$ [Fe/H] ≈ -0.2 dex. The low-α component peaks at [Mg/Fe] $\approx +0.05$ dex and the high-α component at [Mg/Fe] $\approx +0.24$ dex. It shall be stressed that no component of the analysis, neither the (spatial distribution) observed data nor the grid (models), have any known non-linear dependence that could lead to this discontinuity in the space of Mg and Fe abundances. In particular, in the spectroscopic grid used in the chemical abundance analysis, all elemental abundances have a random uniform distribution. In agreement with the visible over-densities, we choose to assign stars to the α-rich population, if their associated [Mg/Fe] abundance is above 0.13 dex, and to the α-poor disc otherwise. Throughout the text, we will proceed to call these two sets of stars "α-rich" and "α-poor" populations.

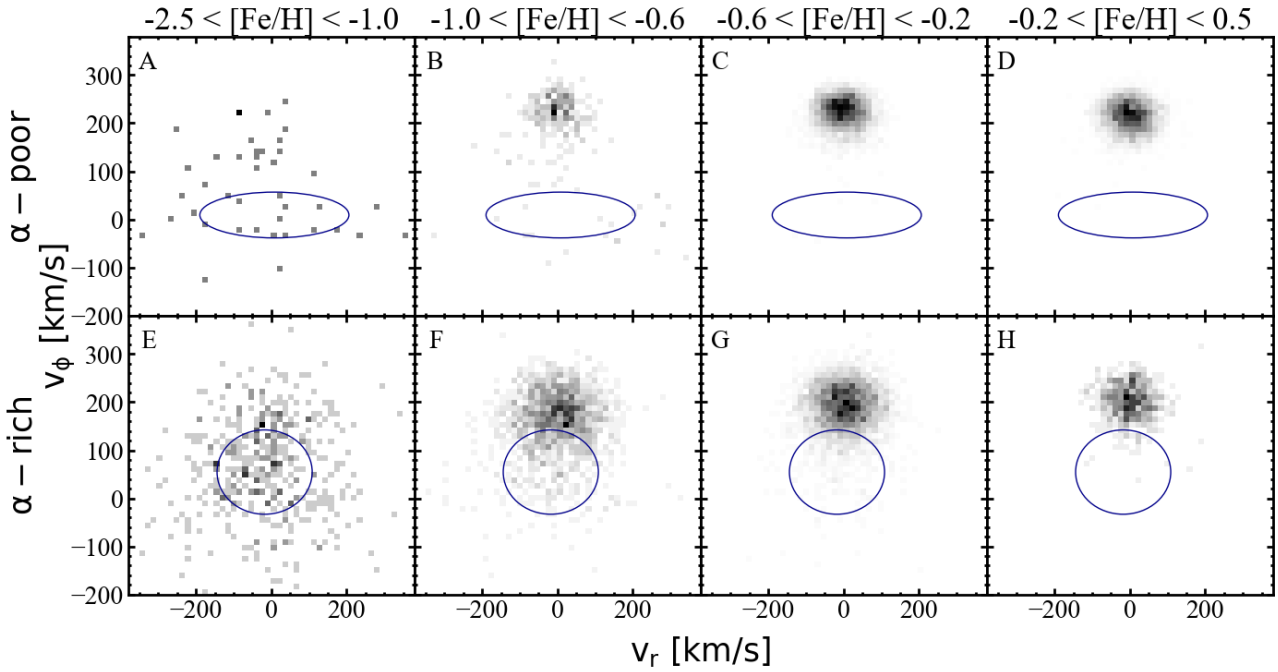

Figure 3.6: Phase-space of the observed Gaia-ESO sample: Circular velocity, V_ϕ, versus radial velocity, V_r, coloured in density. The upper panels represent the α-poor population, and the lower panels represent the α-rich population. Each population is split into two [Fe/H] bins, metal poor and metal solar-rich. The blue ellipse represents the halo distribution following the multi-Gaussian approach described in Belokurov et al. (2018) to determine halo contamination within the disc.

Comparing our distributions with literature, we find an overall satisfactory agreement, although it should be noted that owing to a combination of factors, including vastly different spatial-photometric coverage of observational surveys, their observational strategy, and incomplete volume sampling, certain differences arise that render a one-to-one comparison of chemical abun-

dances in a given volume of the Galaxy impossible. Nonetheless, it appears that our distributions are consistent with the distributions seen in the previous DRs of the Gaia-ESO (e.g. Mikolaitis et al. 2014; Recio-Blanco et al. 2014; Kordopatis et al. 2015), as well as independent studies (e.g. Adibekyan et al. 2013; Bensby et al. 2014). In the latter work, a prominent separation is detected in [Ti/Fe] abundance ratios, whereas the [Mg/Fe] ratios show a more continuous distribution. This could be the consequence of the spatial coverage of the sample. The study by Bensby et al. (2014) focuses on the nearby stars in the solar neighbourhood, whereas our sample probes more extended regions in the R_{gc} - z space, reaching $3 < R_{gc} < 13$ kpc and $|z| \approx \pm 3$ kpc. A similar distribution of the low and high-α/Fe populations is seen in the APOGEE sample (e.g. Hayden et al. 2015). One should note, however, that their α parameter refers to the average of different elements[5], and so their distributions are not directly comparable to the present sample. The GALAH survey results (Bland-Hawthorn et al. 2019; Buder et al. 2021) are also consistent with our distributions. In the chemical distributions of the RAVE stellar sample (Steinmetz et al. 2020), the α-rich component discernible at [α/Fe] $\approx +0.45$, that is somewhat higher compared to our data and the samples from APOGEE[6](Hayden et al. 2015; Jönsson et al. 2020), although consistent within the uncertainties of both samples.

3.7.2 Kinematics and abundances

Figure 3.6 shows the distribution of our α-poor and α-rich samples in the plane of radial velocity, V_r, versus circular velocity, V_ϕ for different metallicity bins. The kinematic quantities were calculated using the positions, proper motions, and parallaxes from Gaia DR3 and the *astropy* package.

It is clearly seen that the majority of stars from both α-rich and α-poor populations are centred with $V_r \simeq 0$ kms^{-1} and $V_\phi \simeq 220$ kms^{-1}, consistent with the expectations for the Galactic disc (Ruchti et al. 2011; Navarro et al. 2011; Bensby et al. 2014). With decreasing metallicity, the velocity dispersion in the radial direction increases, the mean rotation of stars decreases, and a counter-rotating component appears at [Fe/H] ≈ -0.6, which is in line with previous studies of the disc (Fuhrmann 2004; Chiba & Beers 2000; Deason et al. 2017). The perhaps most interesting feature of the observed distributions

[5] O, Mg, Si, S, Ca, and Ti

[6] The Ti abundances from the APOGEE SDSS-DR16 appear to be unreliable.

(Fig. 3.6, panel B) is the presence of a significant fraction of metal-poor, $-1 \lesssim$ [Fe/H] $\lesssim -0.6$, and α-poor stars on disc orbits. In terms of kinematics, these stars are identical to the more metal-rich $\alpha-$poor population suggesting their thin disc origin. In Sect. 3.7.3, we will perform a more detailed analysis of this group in terms of their integrals of motion in order to understand their properties. In the most metal-poor bin, [Fe/H] $\lesssim -1$ dex, low-V_ϕ stars with large radial velocities $|\mathrm{V_r}| \gtrsim 200$ kms^{-1} appear. This population has first been chemically identified by Nissen & Schuster (2010) and Hayes et al. (2018), before finally appearing in Gaia DR2 (Haywood et al. 2018). Belokurov et al. (2018) identified these stars as a population with very radial orbits associated with a massive merger event around 8 to 11 Gyr ago, which was subsequently coined as the Gaia-Sausage Myeong et al. (2018) or the Gaia-Enceladus event Helmi et al. (2018).

Combining Gaia DR2 with APOGEE, Di Matteo et al. (2019) found that the accreted halo component is characterised by the $\mathrm{V}_\phi \approx 0$ kms^{-1} and is approximately Gaussian distributed in $\mathrm{V_r}$, with the corresponding velocity dispersion of ≈ 120 kms^{-1} (Lancaster et al. 2019). For highly prograde velocities, $\mathrm{V}_\phi > 100$ kms^{-1} (Di Matteo et al. 2019, their Fig. 10) however, the contribution of the accreted halo population is of the order of a few percent. Here, we estimate the contamination by the halo stars in our sample following the multi-Gaussian decomposition approach by Belokurov et al. (2018). The model estimates are performed separately for the α-poor and the α-rich populations. In short, we select all stars with $\mathrm{V}_\phi < 0$ and any $\mathrm{V_r}$ value and model the bivariate distribution of V_ϕ and $\mathrm{V_r}$ by a Gaussian that is centred on $\mathrm{V}_\phi = 0$. This resulting bivariate Gaussian function is assumed to represent the halo component of the entire stellar sample. Then, the resulting contamination fraction is calculated as the ratio of the number of stars in this Gaussian to to the total number of stars above a given V_ϕ value. In Table 3.2, we show the resulting expected fractions of the contamination of our sample by halo stars, as predicted by our model for both α populations. Similar to Di Matteo et al. (2019), we find the lowest value of this range to be ~ 110 kms^{-1} (Fig. 3.6). For V_ϕ above this limit, the contamination by the halo is expected to be at the level of $< 1\%$ for the α-poor population, as long as [Fe/H] $\gtrsim -1$. For the most metal-poor bin, [Fe/H] $\lesssim -1$, the contamination is $\sim 12\%$. In the α-rich population, the fractions are not too different in the metallicity bins [Fe/H] $\gtrsim -1$. However, as expected, the halo component becomes dominant over disc for the most metal-poor α-rich bin.

Table 3.2: Contamination of the observed sample by halo stars in %. See text.

Disc population	$V_\phi \geq 110 kms^{-1}$ %	$V_\phi \geq 180 kms^{-1}$ %
α-poor		
$-2.5 <$ [Fe/H]< -1.0	3.5	0.1
$-1.0 <$ [Fe/H]< -0.6	0.2	0.0
$-0.6 <$ [Fe/H]< -0.2	0.0	0.0
$-0.2 <$ [Fe/H]< 0.5	0.0	0.0
α-rich		
$-2.5 <$ [Fe/H]< -1.0	68.9	58.3
$-1.0 <$ [Fe/H]< -0.6	3.3	1.9
$-0.6 <$ [Fe/H]< -0.2	0.7	0.3
$-0.2 <$ [Fe/H]< 0.5	0.0	0.0

In addition, we compute the halo contamination through a slightly different model independent procedure, where instead of fitting the V_ϕ distribution, we calculate the contamination at V_ϕ velocities in individual [Fe/H] bins by reflecting the V_ϕ distribution across $V_\phi = 0$.

Figure 3.7 shows the determination of halo contamination in the thick and thin disc for varying [Fe/H] bins as an alternative method. We analyse stars with $V_\phi < 0$ kms^{-1}, assume symmetry in V_ϕ distribution with respect to $V_\phi = 0$ and therefore determine the number of halo stars with positive circular velocities. The contamination is determined by inspecting the number of stars with $V_\phi > 110$ kms-1 and comparing that to the number of stars in total above the velocity cut. This is determined for each bin of [Fe/H] and so a running average is calculated as opposed to fitting a velocity ellipsoid. This allows us to determine how contamination depends on metallicty and therefore informs the [Fe/H] limit for each alpha- population. Assuming a cut at [Fe/H] = -1, the average halo contamination is less than 10%.

The results of this calculation (Fig. 3.7) confirm the decomposition based on Belokurov et al. (2018), suggesting that above [Fe/H] $\gtrsim -1$ the observed stellar sample is primarily represented by stars with disc-like kinematics, and the contribution of accreted halo stars is marginal (see also Ruchti et al. 2011). It is therefore safe to assume that stars above this metallicity with $\gtrsim 110$ kms^{-1} are representative of the Galactic disc. We use this working definition of the disc in the next section to investigate its evolutionary properties, by combining the chemo-kinematical distributions with the ages of stars.

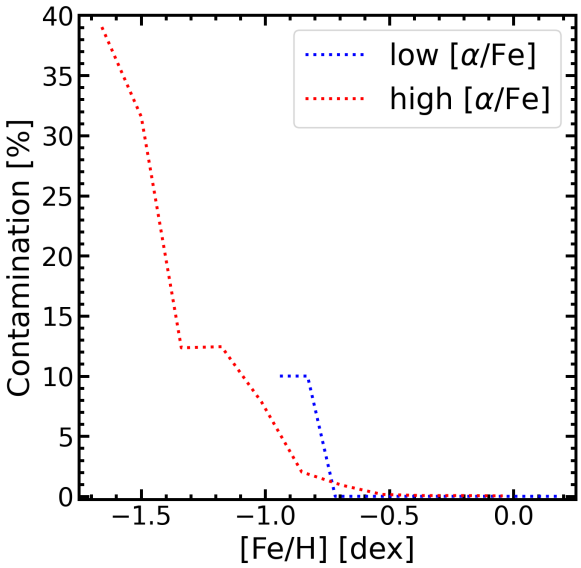

Figure 3.7: Running average of halo contamination in the disc in variable [Fe/H] bins with $V_\phi > 110$ kms^{-1}. The red dotted line represents high α and the blue dotted line represents low α.

3.7.3 Orbital Characteristics

Total Energy and Specific Angular Momentum

It is instructive to analyse the general properties of the data with respect to integrals of motion. Specifically, the relationships between energy E and specific angular momentum L_z help to identify substructure over the entire landscape. This method has successfully been applied to the studies of the Galactic halo (Helmi et al. 2018; Belokurov et al. 2018; Koppelman et al. 2019). Stars which have been accreted and have the same progenitor tend to group together in E-Lz even spread in physical configuration space (Helmi & de Zeeuw 2000; Brown et al. 2005; Gómez 2010; Simpson et al. 2019; Naidu et al. 2020).

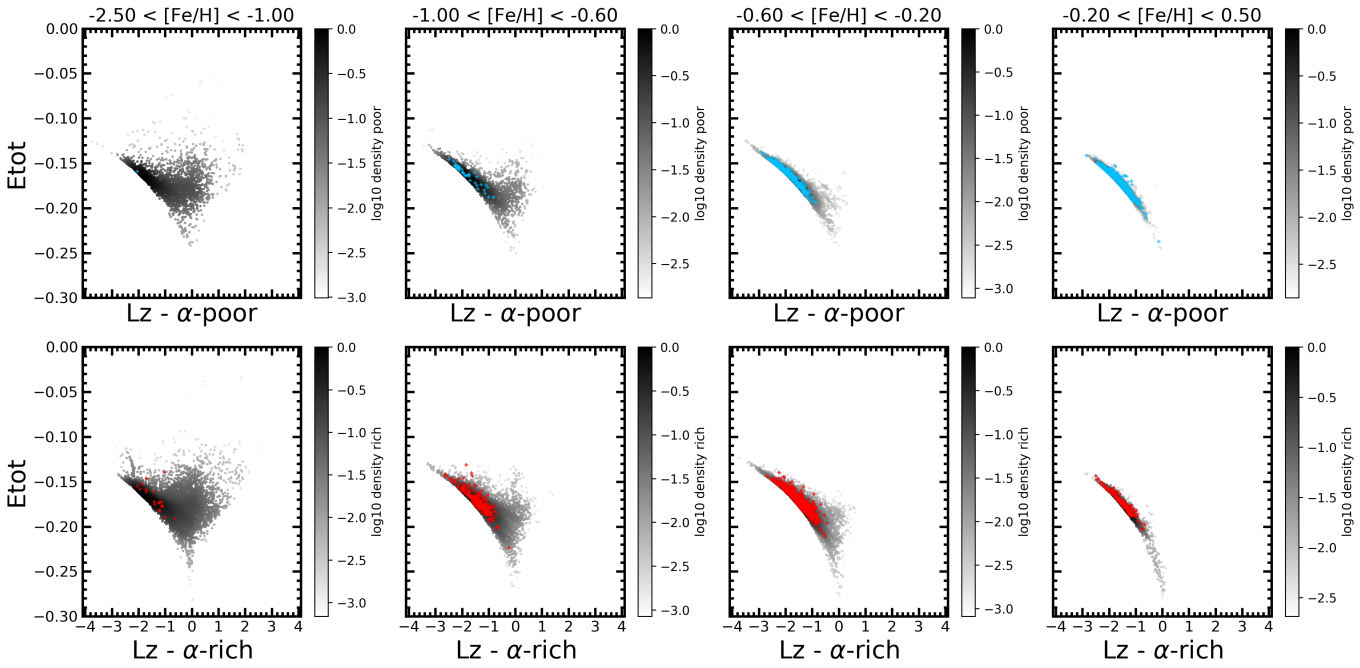

Figure 3.8: Total orbital energy versus specific angular momentum in [Fe/H] bins. For each panel, we show the entire stellar sample in black colour scale representing logarithmic density. Upper panel represents α-poor stars with the Chronos sub-sample coloured in blue. Lower panel represents α-rich stars with the Chronos sub-sample coloured in red.

To derive E-Lz from the 6D Gaia phase space, we used the GalPot code with the Galactic potential from (McMillan 2016). The specific angular momentum is defined as,

$$L_z = V_\phi \times R, \tag{3.1}$$

where V_ϕ is circular velocity and R is Galactocentric radius. The total orbital energy of a system E_{tot} in a cylindrical axisymmetric potential can be split into two terms, that is the kinetic energy describing the kinetic energy of motions in radial and vertical direction and the effective potential

$$E_{tot} = \Phi_{eff} + \frac{1}{2}(V_R^2 + V_Z^2), \tag{3.2}$$

where Φ_{eff} is the effective potential and it includes the gravitational potential, Φ (McMillan 2016), and the centrifugal potential (Bovy 2017),

$$\Phi_{eff}(R,Z,L_z) = \Phi(R,Z) + \frac{L_z^2}{2R^2} \tag{3.3}$$

Figure 3.8 shows the distribution of our full stellar sample in the plane of E_{tot} in Kpc^2 Myr^{-1} versus L_z in Kpc^2 Myr^{-2}. The complete sample is represented by the black colour scale as logarithmic number density.

Action space

In order to further understand the systematic properties of our chemically distinguished samples and to better characterise the old α- and metal-poor sample, we take a step further and look at their vertical and radial actions. In principle, actions and their corresponding angles are just another set of canonical coordinates i.e. $d\vec{\theta} \cdot d\vec{J} = d\vec{x} \cdot d\vec{v}$. However, for non-resonant orbits in axisymmetric potentials, the actions are defined as the constants of motion and are invariant under adiabatic changes and even mostly invariant under radial migration. Therefore, any evolution in action space is caused by the non-axisymmetric nature of the Galaxy.

Furthermore, in those potentials, the three conserved actions J_ϕ, J_r and J_z correspond to our directions in cylindrical coordinates and have a intuitive meaning: J_ϕ is equal to angular momentum L_z. J_R and J_z are a measure of the radial, respectively vertical, excursion of the orbit around its guiding centre radius R_g and the galactic plane. For small excursions and fully decoupled radial and vertical motions, this can be approximated by the are of the ellipsis outlined by the orbit in the $R - v_R$ and $z - Vz$-plane. Using actions hence allows us to fully classify any orbit by just three parameters.

This is also the advantage over taking L_z and E as conserved quantity - in an axis-symmetric potential, we know a third conserved quantity I_3 exists, however, there exists no intuitive meaning and worse, no analytic description for this. Hence, using actions allows us to fully classify any orbit by just 3 parameters. As they are conserved for any orbits, they are also preferential to using velocities in stellar classification which change over the course of an orbital period.

To obtain actions for our stellar sample, we used the `Agama`(Vasiliev 2019) code with the Galactic potential from McMillan (2017). In order to minimise the noise from distance errors, we introduce a parallax cut of 10%, which reduces our sample to 11 137 stars.

Fig. 3.9 shows the resulting action distributions, where we distinguish between the halo population as identified kinematically in Sect. 3.7.2, as well as the α-poor and the α-rich disc components defined chemically.

We can see that all sub-selections except the halo are concentrated around J_r and J_z=0 and seem to be exponential distributed as expected by a pseudoisothermal distribution function (Carlberg & Sellwood 1985; Binney 2010),

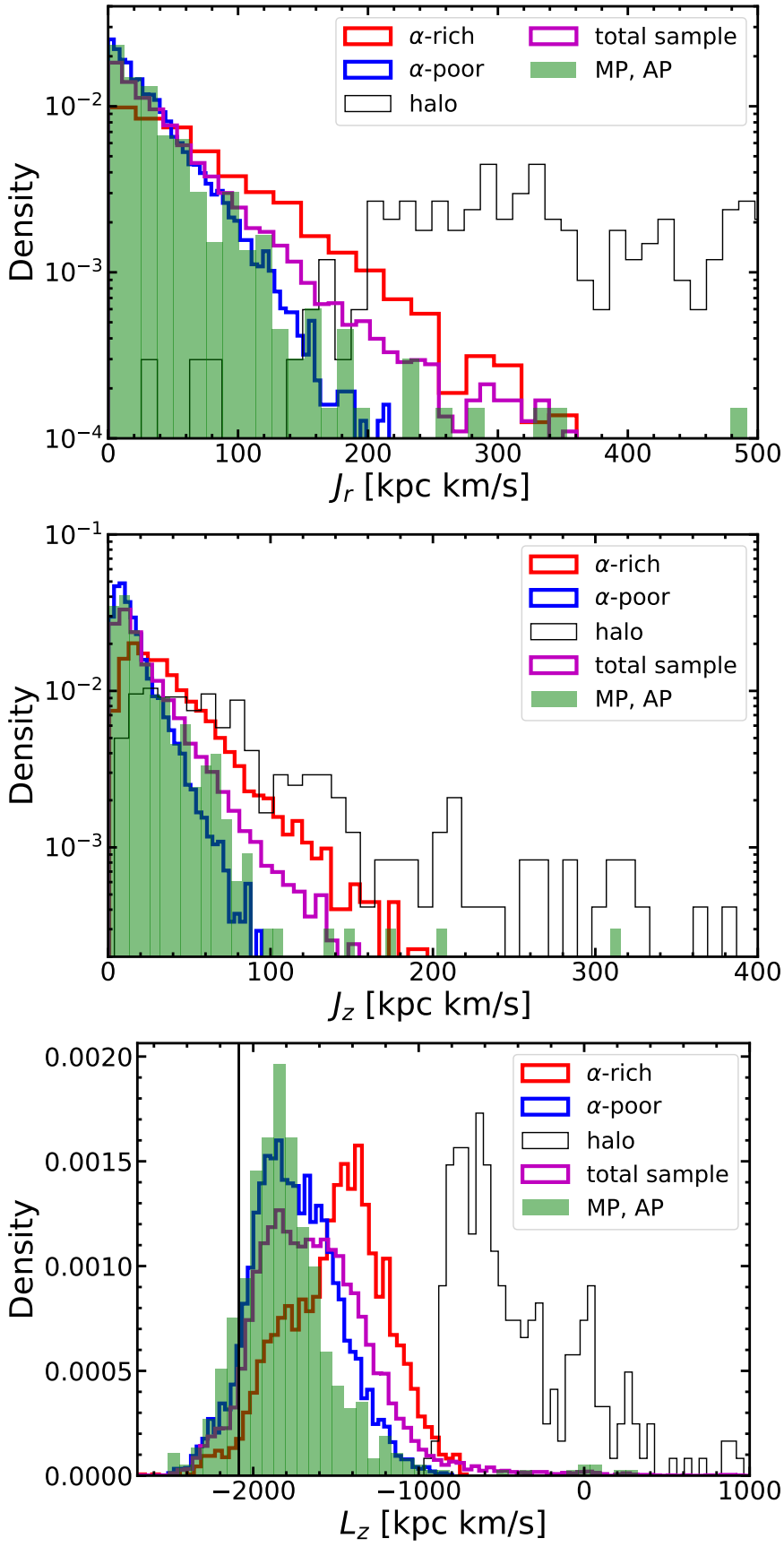

Figure 3.9: Density distribution in all actions for our identified components.

though with different exponential factors. Furthermore, all samples, again except the halo, are centred around an $|L_z|$ slightly lower than the solar value at about -2080 kpc kms^{-1}.[7]. This is a result of the definition of our halo cut which selects all stars with a low v_ϕ. Here, the alpha rich disc tends towards the lower $|L_z|$, i.e. is mostly made up by orbits with guiding centre radius further in the disk. This is a result of the shorter scale length of the α-rich disc with respect to the α-poor one (Bensby et al. 2011; Cheng et al. 2012b).

Distribution of the α-poor, metal poor population: Kinematically Cold Metal Poor Thin Disc

One particularly interesting feature of our disc distributions is the presence of a kinematically cold α- and metal-poor disc component (Fig. 3.9, in filled green). Even after a very strict selection on [Fe/H] and α-abundance is applied ([Fe/H] < -0.5 and [Mg/Fe] < 0.05 dex), it follows quite closely the $J_r$and L_z distribution of the α-poor disc. All but about 10 of these stars are neither in the L_z nor at the high J_r region that could be considered as halo. There is one interesting, slight deviation from the α-poor disc however: It is concentrated at slightly higher $|L_z|$ compared to the full sample, which may indicate that those are outer disc thin disc stars that have since migrated inwards.

Fig. 3.10 shows the density of the cold metal poor disc sample in real space. We can see that we loose nearly all stars with distances of more than ≈ 2 kpc, however, looking at the action plots, we can see that we retain a population at low or even positive L_z which is an indication of the halo population.

Figure 3.11 shows the Kiel diagram and metallicity abundance plane of the sample compared overplotted on the full sample. This sample is not subject to the same constraints made for the Chronos sample as this is purely a kinematic selection of the metal poor alpha poor tail. The cold metal poor disc reveals to mostly contain TO and main-sequence stars with 7 stars which can be identified as RGB stars. In the next section, ages of the Chronos sample are investigated, further ages in the cold metal poor disc are analysed.

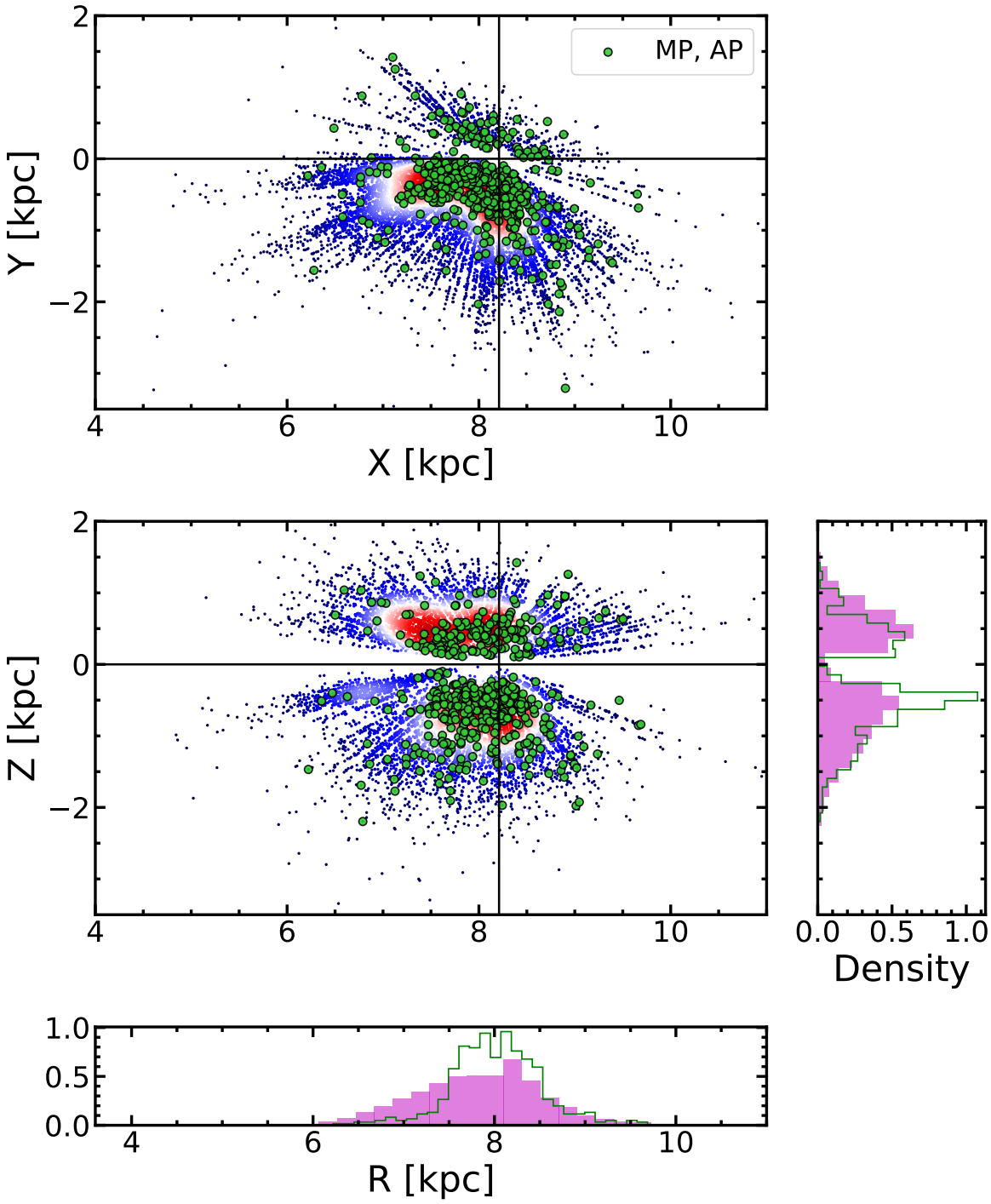

Figure 3.10: Spatial density of the full sample after applying the parallax cut. Overplotted is our metal and alpha poor sample (green dots) with a histogram of the vertical and radial distributions on the edges. The solid magenta histogram is of our full sample.

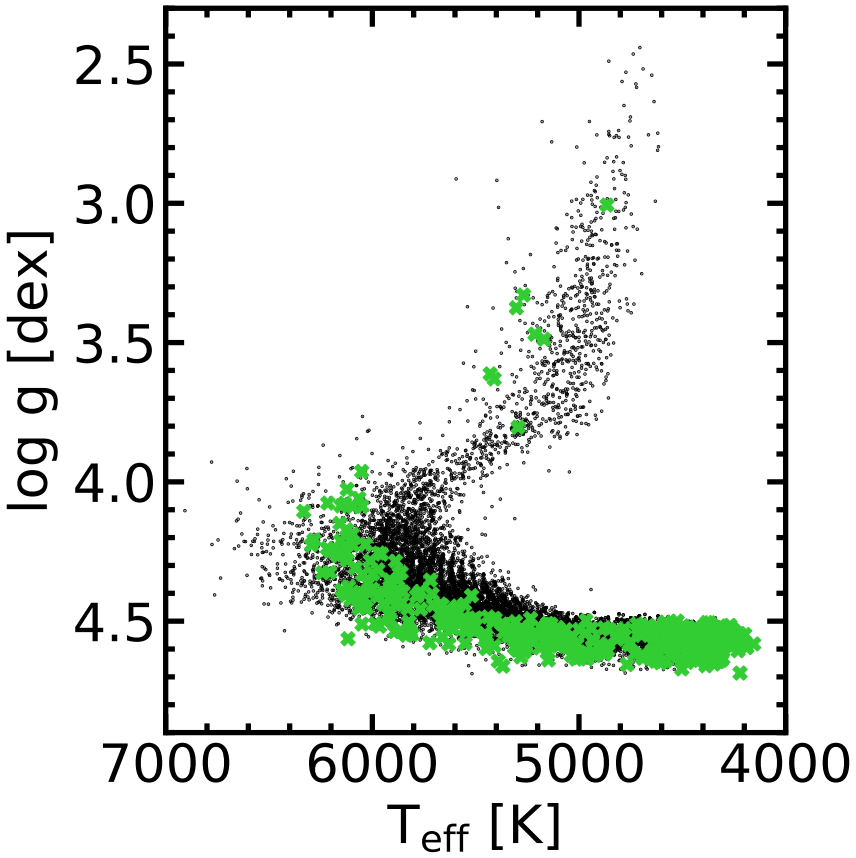

Figure 3.11: $T_{\rm eff}$ vs log$g$ as well as metallicity abundance plane for the full disc sample from Chronos overplotted by the metal and alpha poor component (green crosses).

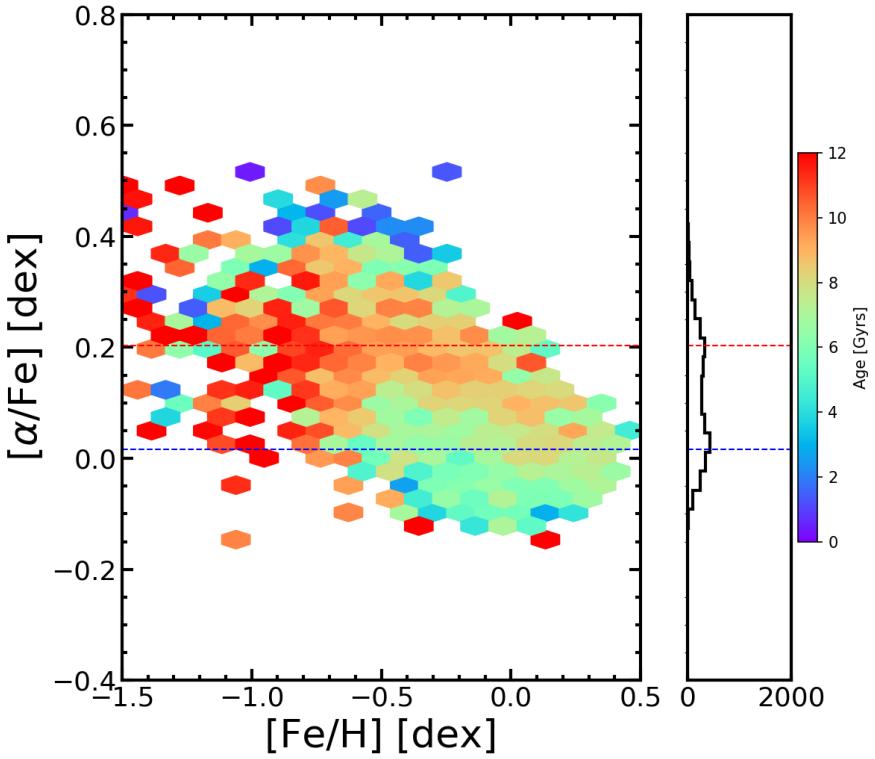

Figure 3.12: $[\alpha/\mathrm{Fe}]$-[Fe/H] space of our Gaia-ESO Chronos sample binned in age.

3.7.4 Ages and abundances of disc stars

In this section, we present the distribution of $[\alpha/\mathrm{Fe}]$ with respect to age for the Galactic disc *Chronos* sample using the kinematic decomposition discussed in Sect. 3.7.2. Figure 3.12 shows $[\alpha/\mathrm{Fe}]$ versus [Fe/H] binned in age for colour scale. It further expanded into [Fe/H] bins for $[\alpha/\mathrm{Fe}]$ vs Age and age bins for $[\alpha/\mathrm{Fe}]$ vs [Fe/H] in Figure 3.13.

The bi-modal distribution in Fig. 3.13 defining the α-rich and α-poor populations clearly shows a strong evolution with age. Most stars in the α-rich population, with the mean $[\alpha/\mathrm{Fe}] \approx 0.24$ dex, have the age of ~ 8 to ~ 12 Gyrs, in line with the results by Xiang & Rix (2022). In contrast, the α-poor population, mean $[\alpha/\mathrm{Fe}] \approx 0.03$ dex, is characterised by a much wider distribution of ages from a few to ~ 10 Gyr. In the intermediate range of ages, $7 \lesssim \tau \lesssim 11$ Gyr, both α-poor and α-rich components overlap in age, which suggests their possible co-evolution over this limited period of time. This reveals an old component of our *Cold metal poor disc*.

[7]Here we use the solar radius of 8.34 kpc from Reid et al. (2014) and solar velocity $V\odot = 12.24\mathrm{kms}^{-1}$ and rotation curve $V_{\mathrm{circ}} = 238$ kms^{-1} from (Schönrich 2012).

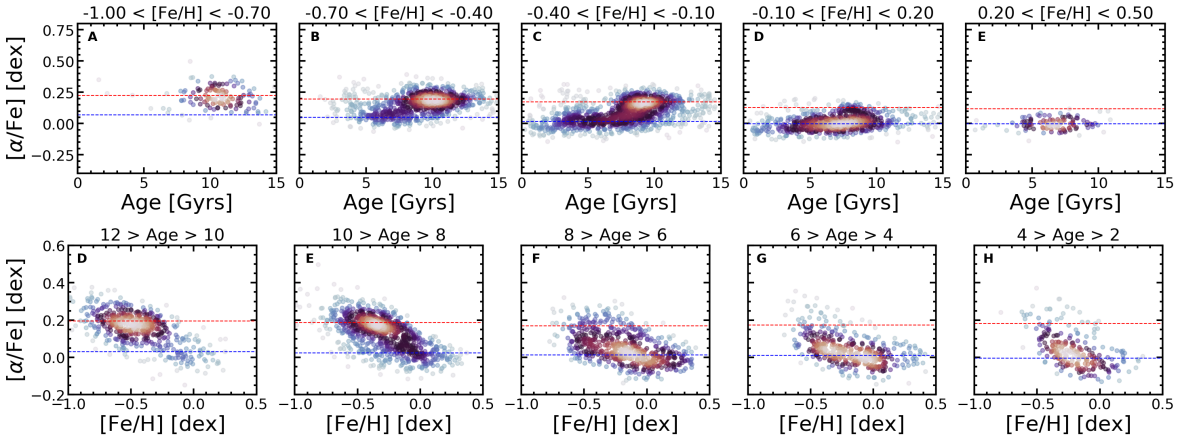

Figure 3.13: The observed sample of Galactic disc stars from the age validated Chronos sample in the [α/Fe]-age (upper panel) and [Fe/H]-age (lower panel) plane.

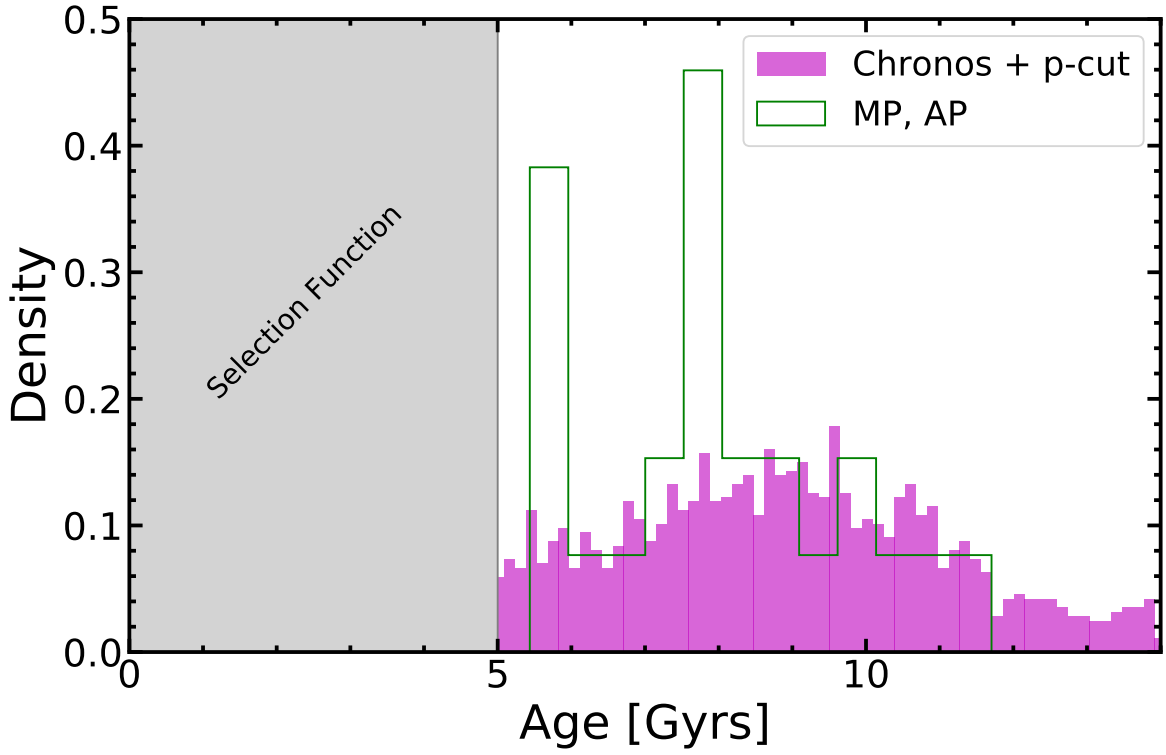

Figure 3.14: The observed sample of Galactic disc stars from the age validated Chronos sample (with a fractional parallax cut of 10%) in the [α/Fe]-age (upper panel) and [Fe/H]-age (lower panel) plane.

The presence of old α-poor stars ranging in metallicities is intriguing although not fully unexpected. We can see this more clearly in Fig. 3.14 where ages below 5 Gyrs are not inspected due to the age bias from the selection function. We can see that comparing the cold metal poor thin disc with the *full disc sample* from Chronos with distance cuts applied that there is a old sample of stars peaking around 8 Gyrs. Among the earlier studies, Hayden et al. (2017) remarked on the significant temporal and chemical ([Fe/H]) overlap of the α-rich and α-poor components of the Galactic disc, studying the properties of TO and subgiant stars in the AMBRE:HARPS survey. Silva Aguirre et al. (2018) identified a population of old α-poor stars through asteroseismic age dating of APOGEE targets in the Kepler field. They report an overlap in age from 8 - 14 Gyrs between the α-poor and α-rich components. A non-negligible fraction of α-poor metal-rich stars with ages up to 9 Gyr is also evident in the results by Xiang & Rix (2022). Similar distributions are seen in the results based on the APOGEE data by Ciucă et al. (2021) and Beraldo e Silva et al. (2021), who find α-poor stars with ages up to ~ 12 Gyr spanning the entire range of metallicity, $-0.7 \lesssim [\mathrm{Fe/H}] \lesssim +0.4$, in the solar neighbourhood. The study by Beraldo e Silva et al. (2021) is relevant in the context of our work, as the spatial coverage is similar, $\mathrm{R_{helio}} \sim 2$ kpc, and the targeted stellar population (subgiants and the lower part of the RGB branch) overlaps with the properties of our observed Gaia-ESO sample. Feuillet et al. (2019) find rather tight age-$[\alpha/\mathrm{Fe}]$ relationships, with some evidence for the presence of old α-poor stars. However, they do not report stellar densities in each bin in the age-$[\alpha/\mathrm{Fe}]$ plane (e.g. their Fig 6), whereas this would be necessary to confirm whether an age-$[\alpha/\mathrm{Fe}]$ bimodality exists in their distributions. The next section, we explore what could have caused this temporal overlap and so the origin of these old stars from the *cold metal poor disc*.

Possibility of Co-evolution epoch of the thin and thick disc

The temporal extent of the thick ($[\alpha/\mathrm{Fe}]$-rich) disc appears to be well-established (Bensby et al. 2005; Haywood et al. 2013; Hayden et al. 2017), and our results reinforce the evidence for a rather limited star formation in this population. In contrast, the age (τ) distribution of the $[\alpha/\mathrm{Fe}]$-poor disc population extends out to $\tau > 10\,\mathrm{Gyr}$ and spans a broad range of metallicities $-0.7 \lesssim [\mathrm{Fe/H}] \lesssim +0.2$. Whereas the extended star formation history of the α-poor disc is not new, within our results, a small population of stars may

hint at interpretation that the $[\alpha/\mathrm{Fe}]$-rich and $[\alpha/\mathrm{Fe}]$-poor disc could possibly co-exist during a limited epoch.

Our analysis is not the first to highlight the possibility of the parallel formation of the Galactic discs. This scenario appear to be consistent with studies based on different age dating methods and different observational samples (Hayden et al. 2017; Ciucă et al. 2021; Beraldo e Silva et al. 2021) and it received support from studies based on other tracers, including the analyses of properties of $\alpha-$poor old RR Lyrae in the disc (Prudil et al. 2020) and high-latitude stellar overdensities (e.g. Laporte et al. 2020). The latter study, in particular, showed that for the Anticenter Stream (ACS), a coherent stream-like outer disc structure with $[\mathrm{Fe/H}] \sim -0.6$ and no enhancement of α elements, the cumulative age distribution is consistent a high fraction of old stars $\tau > 10\,\mathrm{Gyr}$ and an abrupt dearth of young stars. The Monoceros Ring (Newberg et al. 2002) shows more steady star formation through the presence of a more extended distribution stars with ages from ~ 5 to ~ 10 Gyr (Laporte et al. 2020).

At face value, this implies that the Milky Way galaxy already had an $[\alpha/\mathrm{Fe}]$-poor disc in place before $z \sim 2$, around the peak of the cosmic star formation rate density (Madau & Dickinson 2014). The size of the early disc cannot be reliably estimated in this work, because our sample probes a rather limited spatial volume, about few kpc from the Sun. However, we find that even the oldest stars in the alpha-poor disc are not preferentially confined to the inner disc, but are rather broadly distributed over the entire range of Galactocentric radii probed by the observed sample. While such an extended disc size would make the Galaxy seem like an outlier to the general size-evolutionary trend for MW-like galaxies (van Dokkum et al. 2013), we note that the stars in the ACS most probably started out with smaller guiding radii and were later excited to larger ones following interactions with a massive satellite (see Laporte et al. 2019a, for an N-body study on the formation of ACS-like structures). Laporte et al. (2022) argued that estimated time at which the ACS decoupling from the disc is similar to the timescale of the merger via the Gaia-Sausage-Enceladus event (Naidu et al. 2021). This is also consistent with the Beraldo e Silva et al. (2021) interpretation that a significant (30 to 50%) fraction of the local old α-poor stars are migrators from the inner disc.

Several scenarios have been invoked to explain the formation of the thick and thin disc, but only several of them predict a co-evolution of the discs. In cos-

mological simulations of galaxy formation (e.g. Brook et al. 2004; Buck 2020; Agertz et al. 2021), the old α-poor stellar population originates as a result of star formation following a merger that brings pristine (H-rich) metal-free gas from the circumgalactic medium, thus drastically reducing the metallicity of the ISM at a constant (low) $[\alpha/\mathrm{Fe}]$ ratio. These stars are expected to be about 7 to 10 Gyr old, although this depends on the time of the merger. Nonetheless, the main prediction of this scenario is the presence of both alpha-poor and alpha-rich populations at a given metallicity, whereby the alpha-poor population is about 2 Gyr younger. There are also controlled hydrodynamical simulations of clump formation in the primordial disc (Bournaud et al. 2009; Clarke et al. 2019) that follow the evolution of self-enriching high star formation density clumps similar to those seen in high-z galaxies (e.g. Elmegreen & Elmegreen 2005). In these simulations, the formation of the thin disc sequence is accompanied by that of the thick disc (a-rich) sequence, the latter emerging from gas-rich self-enriching clumps in the early α-poor disc. Whereas this scenario is favoured by Beraldo e Silva et al. (2021), whose conclusions on the bimodal age-$[\alpha/\mathrm{Fe}]$ structure of the disc are very similar to ours, Ciucă et al. (2021) interpret their findings in the hybrid framework, involving rapid central enrichment, cold gas accretion (or merger), and radial evolution of the disc (Grand et al. 2018). That is, the signature of gradual chemical enrichment in the disc, with the old part of the thick disc component forming from turbulent well-mixed inner regions owing to a merger or metal-poor gas accretion, and the thin (inner and outer disc) forming at later stages over a continuous period of time fuelled by hot gas accretion from the halo. In summary, our results disfavour strictly sequential formation scenarios or the thin and thick discs and are in line with recent observational studies (Silva Aguirre et al. 2018; Beraldo e Silva et al. 2021; Ciucă et al. 2021). Instead, our data can be best interpreted in the context of the parallel formation scenario of the discs. However, the precision and accuracy of ages is not yet fully sufficient to disentangle between the clumpy formation (as in Clarke et al. 2019) and gradual enrichment involving a metal-poor gas accretion and mergers (as in Grand et al. 2018), that is the two disc formation scenarios that predict that the disc components grew in parallel, at least during a limited period of time, in the early Galaxy.

3.8 Conclusion

In this work, we study the enrichment properties of Galactic disc using the observed abundances, ages, and kinematics of stars observed by the Gaia-ESO survey. We have used spectra from the fourth public data release (DR4) of the Gaia-ESO survey, to derive stellar parameters and non-LTE abundances for stars within a ~ 2 kpc volume about the Sun, with majority of stars spanning $6 < R < 10$ kpc in Galactocentric radius and $|Z| < 2$ kpc in vertical distance from the plane. We kinematically isolate our disc stars and break down the Milky Way into its Galactic components (Halo, α-rich, α-poor disc). And thus, through action space, discover evidence of a cold metal poor thin disc. We further determine ages (τ) for a fraction of stars in the sample, primarily focusing on late main-sequence, subgiant, turn-off stars, and investigate the influence of the survey selection function on the age-metallicity distributions.

We find that the two chemically-defined components of the Galactic disc, $[\alpha/\mathrm{Fe}]$-poor and $[\alpha/\mathrm{Fe}]$-rich, show a significant temporal overlap of about 2 to 3 Gyrs. Both populations are old. The α-rich disc extends out to ages $\tau > 12$ Gyr, and the α-poor component with $-0.7 \lesssim [\mathrm{Fe/H}] \lesssim +0.4$ is present already as early as 10 Gyr ago. The overlap thus refers to the limited period from $\tau \sim 7$ to ~ 11 Gyr, which is when both disc components are clearly visible in the age-α diagram.

Our results therefore could be explained by the parallel formation of the disc components, challenging the classical sequential scenarios, such as the two-infall model with a star-formation hiatus (Chiappini et al. 1997) or the in-situ formation of the thin disc from the thick disc (Bird et al. 2013). Rather, we suggest that the growth of the α-poor and α-rich components accompanied each other during a significant period of time of several Gyr. The two possible options are the formation of the α-rich component from the primordial thin disc, i.e the clumpy formation (Clarke et al. 2019) or gradual formation of the two populations primarily associated with the differential evolution of the inner and outer discs (Grand et al. 2018; Ciucă et al. 2021). There is tentative evidence for the latter, since in our data the α-rich disc component is on average older and more metal-poor than the α-poor component. However, we do find some stars in the α-poor population that are *as old* as those in the α-rich population. Since in the clumpy and distributed star formation scenario, the gas-rich fragments have a high star formation rate density, the paucity of

primordial thin disc stars (compared to thick disc stars) in our observations can in principle also be understood in the framework of the clumpy disc formation model. Future surveys with better coverage and higher quality data such 4MOST, and WEAVE, will allow to provide a better spatial and temporal coverage of the disc allowing to distinguish between the two scenarios. The next goal will be to analyse 1 million Gaia RVS spectra (Recio-Blanco et al. 2022) with the SAPP to investigate the kinematic space further beyond Gaia-ESO coverage.

Chapter 4

Summary

- In the first part of this work, we developed the Stellar Abundances and atmosphere Parameters Pipeline SAPP. The SAPP was developed to analyse multiple types of observational data from large-scale surveys in order to determine fundamental stellar parameters and so to characterise their surface and interior properties. The SAPP combines multiple techniques. The spectroscopy module uses NLTE synthetic spectra computed with *The Payne* (Ting et al. 2019; Kovalev et al. 2019) in combination with observed stellar spectra, which allow the determination of $T_{\rm eff}$, $\log g$, [Fe/H], abundances (Mg, Ti, Mn) and other parameters such as radial velocity, microturbulence, and stellar rotation. The photometry module compares observed photometry from Gaia DR3, 2MASS, Johnsons BV, and distances (Bailer-Jones et al. 2021) to synthetic photometric magnitudes and luminosities based on GARSTEC stellar evolution models. The asteroseismology module compares observed global oscillation parameters ν_{max} and $\delta\nu$ of stars to model asteroseismic values. All modules are combined using a Bayesian algorithm with selected priors to produce a final posterior for each star whereby a final set of fundamental parameters are calculated.
- We apply the SAPP to Gaia-ESO HR10, UVES, and HARPS spectra of FGK benchmark stars described in Gent et al. (2022), for which photometry and asteroseismic parameters are available. We find a good agreement with respect to independently derived stellar parameters, specifically, interferometric Teff values. We show that the combination of different observational information for a star is the most optimal approach, that allows highly accurate and self-consistent estimates of stellar Teff, log(g), metallicities, radii, luminosities, masses, and ages, and therefore

help to ensure that the goals on the accuracy of stellar characterisation in the PLATO space mission are achieved.

- To test the ability of the SAPP to characterise red giant branch stars and clusters, we derived stellar parameters for the kinematically-selected members of the well-studied literature clusters NGC 104, NGC 1261, NGC 362, NGC 4590, NGC 6253, NGC 6752. We find an excellent agreement in derived stellar parameters and NLTE metallicities of the cluster members, with a very small intra-cluster dispersion of typically 0.05 dex, except NGC 6752. The results are in good agreement with previous literature analysis of the clusters, although most previous studies employed LTE synthetic spectral models. The internal scatter of the intra-cluster NLTE metallicities is smaller compared to the strictly spectroscopic NLTE analysis of Kovalev et al. (2019) that re-inforces the evidence that the combination of photometry, parallaxes, and spectra improves the astrophysical characterisation of stars.
- In the second part of this work, we applied the SAPP pipeline to the entire public release of the Gaia-ESO large spectroscopic survey. We analysed 53,147 stars to test the applicability of the pipeline as well as to improve the constraints on chemical, kinematical and temporal structure of the Milky Way's using more accurate stellar abundances and ages. From the detailed chemo-dynamical analysis, we found that our stellar sample shows well-defined structure corresponding to the expectations for the Galactic disc and the halo.
- Further, we analysed the orbital characteristics of the Galactic disc stars via action potentials and found evidence for a kinematically-cold metal-poor, [Fe/H] $\approx$ -0.6, and α-poor (thin) disc component. The analysis of the phase-space suggests that stars in this component could have migrated from the outer disc of the Galaxy, and a non-negligible fraction of them is old, with ages above 8 Gyr. The distribution of α-rich and α-poor stars may hint at a temporal overlap between the thin and thick disc implying the possiblity of a co-evolution. We explore the formation scenarios of the Galactic disc with respect to parallel formation of the α-poor and α-rich disc, and so provide a possible origin to these small group of stars with old ages.
- The development of the SAPP for the past 3 years has been working towards the goal of analysing large stellar surveys efficiently by com-

bining different types of observational data within a robust statistical framework. I have worked closely with missions such as PLATO Rauer et al. 2016, 4MOST Seifert et al. 2016, and WEAVE Famaey et al. 2016 in order to achieve this.

- The modular nature SAPP allows it to be continuously updated with the latest physics, models and gives flexibility to analyse different future and current surveys such as SDSS-V (Kollmeier et al. 2017). Further, in my collaboration with PLATO, SAPP has been improved to analyse M-dwarfs in the Milky Way via APOGEE spectra (in-prep).
- With the Gaia-ESO (Randich et al. 2022) survey finished, this allowed us to consider the selection function, and systematics investigated over the duration of the survey. Gaia-ESO provided an incredible testing ground for medium resolution spectra, resembling high resolution spectra for WEAVE and 4MOST. Where we expect data for both within the next year. The advantage being that WEAVE covers the northern hemisphere and 4MOST covering the southern hemisphere, both surveys expected to be used within the PLATO space mission.
- Through my membership in WEAVE, 4MOST and in PLATO I will have proprietary access to an unprecedented number of high-quality spectra of exo-host candidates over the next years. The current input catalogues of the 4MIDABLE-HR survey (Bensby et al. 2019) contains over $4\text{x}10^6$ stars with over $2\text{x}10^6$ expected to have a signal-to-noise (SNR) $>$ 100/, in which I am a member, include several thousands of confirmed exo-planet hosts, 4×10^5 targets from TESS, and targets in the long-pointing field of PLATO (Nascimbeni et al. 2022).
- The SAPP is intended to be a core analytical tool for large scale current and future surveys. The applicability and flexibility of the pipeline has been made for public use for the leisure of the scientific community.

4.1 Publications

First Author

Gent, M. R., Bergemann, M., Serenelli, A., et al. 2022, Astron. Astrophys., 658, A147

Gent, M. R., Eitner, P., Bergemann, M. et al. 2022, arXiv e-prints, arXiv:2206.10949

Co-Author

Eitner, P., Bergemann, M., Ruiter, A. J. et al. 2022, arXiv e-prints, arXiv:2206.10258

Nielsen, J., Gent, M. R., et al. 2022 "Planet formation throughout the Milky way: Planet populations in the context of Galactic chemical evolution" (subm to A&A)

Olander, T., Gent, M. R., Heiter, U. et al. 2022 "Performance of the Stellar Abundances and atmospheric Parameters Pipeline on M dwarfs" (in-prep to be submitted to A&A)

References

Adibekyan, V. Z., Figueira, P., Santos, N. C., et al. 2013, Astron. Astrophys., 554, A44

Agertz, O., Renaud, F., Feltzing, S., et al. 2021, Mon. Not. R. Astron. Soc., 503, 5826

Aller, L. H. 1942, , 1, 11

Alonso, A., Arribas, S., & Martinez-Roger, C. 1994, Astron. Astrophys., 282, 684

Amarsi, A. M., Nissen, P. E., & Skúladóttir, Á. 2019, Astron. Astrophys., 630, A104

Anguiano, B., Freeman, K., Steinmetz, M., & de Boer, E. W. 2012, in European Physical Journal Web of Conferences, Vol. 19, European Physical Journal Web of Conferences, 05009

Arribas, S. & Martinez Roger, C. 1989, Astron. Astrophys., 215, 305

Astropy Collaboration, Robitaille, T. P., Tollerud, E. J., et al. 2013, Astron. Astrophys., 558, A33

Aumann, H. H. & Probst, R. G. 1991, Astrophys. J., 368, 264

Bailer-Jones, C. A. L., Rybizki, J., Fouesneau, M., Demleitner, M., & Andrae, R. 2021, Astron. J., 161, 147

Bailer-Jones, C. A. L., Rybizki, J., Fouesneau, M., Mantelet, G., & Andrae, R. 2018, Astron. J., 156, 58

Barbuy, B. 2019, in The La Silla Observatory - From the Inauguration to the Future, 5

Barbuy, B., Chiappini, C., & Gerhard, O. 2018, ARA&A, 56, 223

Bastian, N. & Lardo, C. 2018, ARA&A, 56, 83

Bazot, M., Bourguignon, S., & Christensen-Dalsgaard, J. 2012, Mon. Not. R. Astron. Soc., 427, 1847

Bazot, M., Creevey, O., Christensen-Dalsgaard, J., & Meléndez, J. 2018, Astron. Astrophys., 619, A172

Belkacem, K., Dupret, M. A., Baudin, F., et al. 2012, Astron. Astrophys., 540, L7

Belkacem, K., Goupil, M. J., Dupret, M. A., et al. 2011, Astron. Astrophys., 530, A142

Belokurov, V., Erkal, D., Evans, N. W., Koposov, S. E., & Deason, A. J. 2018, Mon. Not. R. Astron. Soc., 478, 611

Belokurov, V., Zucker, D. B., Evans, N. W., et al. 2006, Astrophys. J. Lett., 642, L137

Belyaev, A. K. & Voronov, Y. V. 2020, Astrophys. J., 893, 59

Bensby, T., Alves-Brito, A., Oey, M. S., Yong, D., & Meléndez, J. 2011, Astrophys. J. Lett., 735, L46

Bensby, T., Bergemann, M., Rybizki, J., et al. 2019, The Messenger, 175, 35

Bensby, T., Feltzing, S., & Lundström, I. 2003, Astron. Astrophys., 410, 527

Bensby, T., Feltzing, S., Lundström, I., & Ilyin, I. 2005, Astron. Astrophys., 433, 185

Bensby, T., Feltzing, S., & Oey, M. S. 2014, Exploring the Milky Way stellar disk. A detailed elemental abundance study of 714 F and G dwarf stars in the solar neighbourhood

Bensby, T., Zenn, A. R., Oey, M. S., & Feltzing, S. 2007, Astrophys. J. Lett., 663, L13

Beraldo e Silva, L., Debattista, V. P., Nidever, D., Amarante, J. A. S., & Garver, B. 2021, Mon. Not. R. Astron. Soc., 502, 260

Bergemann, M., Collet, R., Amarsi, A. M., et al. 2017, Astrophys. J., 847, 15

Bergemann, M., Gallagher, A. J., Eitner, P., et al. 2019, Astron. Astrophys., 631, A80

Bergemann, M., Hoppe, R., Semenova, E., et al. 2021, Mon. Not. R. Astron. Soc., 508, 2236

Bergemann, M., Lind, K., Collet, R., Magic, Z., & Asplund, M. 2012, Mon. Not. R. Astron. Soc., 427, 27

Bergemann, M., Ruchti, G. R., Serenelli, A., et al. 2014, Astron. Astrophys., 565, A89

Bialek, S., Fabbro, S., Venn, K. A., et al. 2020, Mon. Not. R. Astron. Soc., 498, 3817

Binney, J. 2010, Mon. Not. R. Astron. Soc., 401, 2318

Bird, J. C., Kazantzidis, S., & Weinberg, D. H. 2012, Mon. Not. R. Astron. Soc., 420, 913

Bird, J. C., Kazantzidis, S., Weinberg, D. H., et al. 2013, Astrophys. J., 773, 43

Blackwell, D. E. & Shallis, M. J. 1977, Mon. Not. R. Astron. Soc., 180, 177

Blackwell, D. E., Shallis, M. J., & Selby, M. J. 1979, Mon. Not. R. Astron. Soc., 188, 847

Bland-Hawthorn, J. & Gerhard, O. 2016a, ARA&A, 54, 529

Bland-Hawthorn, J. & Gerhard, O. 2016b, ARA&A, 54, 529

Bland-Hawthorn, J., Sharma, S., Tepper-Garcia, T., et al. 2019, Mon. Not. R. Astron. Soc., 486, 1167

Böhm-Vitense, E. 1958, , 46, 108

Borucki, W. J., Koch, D., Basri, G., et al. 2010, Science, 327, 977

Bournaud, F., Elmegreen, B. G., & Martig, M. 2009, Astrophys. J. Lett., 707, L1

Bovy, J. 2017, Mon. Not. R. Astron. Soc., 470, 1360

Bovy, J., Rix, H.-W., Schlafly, E. F., et al. 2016, Astrophys. J., 823, 30

Boyajian, T. S., McAlister, H. A., van Belle, G., et al. 2012, Astrophys. J., 746, 101

Brandão, I. M., Doğan, G., Christensen-Dalsgaard, J., et al. 2011, Astron. Astrophys., 527, A37

Brook, C. B., Gibson, B. K., Martel, H., & Kawata, D. 2005, Astrophys. J., 630, 298

Brook, C. B., Kawata, D., Gibson, B. K., & Freeman, K. C. 2004, Astrophys. J., 612, 894

Brown, W. R., Geller, M. J., Kenyon, S. J., & Kurtz, M. J. 2005, Astrophys. J. Lett., 622, L33

Bruntt, H., Basu, S., Smalley, B., et al. 2012, Mon. Not. R. Astron. Soc., 423, 122

Bruntt, H., Bedding, T. R., Quirion, P. O., et al. 2010, Mon. Not. R. Astron. Soc., 405, 1907

Buchhave, L. A., Bizzarro, M., Latham, D. W., et al. 2014, Nature, 509, 593

Buchhave, L. A. & Latham, D. W. 2015, Astrophys. J., 808, 187

Buck, T. 2020, Mon. Not. R. Astron. Soc., 491, 5435

Buder, S., Sharma, S., Kos, J., et al. 2021, Mon. Not. R. Astron. Soc.[[arXiv]2011.02505]

Canuto, V. M. & Mazzitelli, I. 1991, Astrophys. J., 370, 295

Capitanio, L., Lallement, R., Vergely, J. L., Elyajouri, M., & Monreal-Ibero, A. 2017, Astron. Astrophys., 606, A65

Carlberg, R. G. & Sellwood, J. A. 1985, Astrophys. J., 292, 79

Carpenter, J. M. 2001, Astron. J., 121, 2851

Carretta, E., Gratton, R. G., Bragaglia, A., Bonifacio, P., & Pasquini, L. 2004, Astron. Astrophys., 416, 925

Carrier, F., Eggenberger, P., & Bouchy, F. 2005, Astron. Astrophys., 434, 1085

Carter, B. S. 1990, Mon. Not. R. Astron. Soc., 242, 1

Casagrande, L., Lin, J., Rains, A. D., et al. 2020, arXiv e-prints, arXiv:2011.02517

Casagrande, L., Lin, J., Rains, A. D., et al. 2021a, Mon. Not. R. Astron. Soc., 507, 2684

Casagrande, L., Lin, J., Rains, A. D., et al. 2021b, Mon. Not. R. Astron. Soc., 507, 2684

Casagrande, L., Portinari, L., & Flynn, C. 2006, Mon. Not. R. Astron. Soc., 373, 13

Casagrande, L., Ramírez, I., Meléndez, J., Bessell, M., & Asplund, M. 2010a, Astron. Astrophys., 512, A54

Casagrande, L., Ramírez, I., Meléndez, J., Bessell, M., & Asplund, M. 2010b, Astron. Astrophys., 512, A54

Casagrande, L., Schönrich, R., Asplund, M., et al. 2011, Astron. Astrophys., 530, A138

Cayrel, R., Hill, V., Beers, T. C., et al. 2001, Nature, 409, 691

Challouf, M., Nardetto, N., Domiciano de Souza, A., et al. 2015, Astron. Astrophys., 579, A107

Challouf, M., Nardetto, N., Mourard, D., et al. 2014, Astron. Astrophys., 570, A104

Chaplin, W. J. & Miglio, A. 2013, ARA&A, 51, 353

Chaplin, W. J., Serenelli, A. M., Miglio, A., et al. 2020, Nature Astronomy, 4, 382

Cheng, J. Y., Rockosi, C. M., Morrison, H. L., et al. 2012a, Astrophys. J., 752, 51

Cheng, J. Y., Rockosi, C. M., Morrison, H. L., et al. 2012b, Astrophys. J., 752, 51

Chiappini, C., Matteucci, F., Beers, T. C., & Nomoto, K. 1999, Astrophys. J., 515, 226

Chiappini, C., Matteucci, F., & Gratton, R. 1997, Astrophys. J., 477, 765

Chiavassa, A., Casagrande, L., Collet, R., et al. 2018, Astron. Astrophys., 611, A11

Chiba, M. & Beers, T. C. 2000, Astron. J., 119, 2843

Christensen-Dalsgaard, J. 2002, Reviews of Modern Physics, 74, 1073

Chu, Y. Q. & Cui, X. Q. 1996, in Ground-Based Astronomy in Asia, ed. N. Kaifu, 327

Ciucă, I., Kawata, D., Miglio, A., Davies, G. R., & Grand, R. J. J. 2021, Mon. Not. R. Astron. Soc., 503, 2814

Clarke, A. J., Debattista, V. P., Nidever, D. L., et al. 2019, Mon. Not. R. Astron. Soc., 484, 3476

Cowan, J., Sneden, C., Burles, S., et al. 2002, The Astrophysical Journal, 572, 861

Cox, J. P. & Giuli, R. T. 1968, Principles of stellar structure

Creevey, O. L., Metcalfe, T. S., Schultheis, M., et al. 2017, Astron. Astrophys., 601, A67

Cui, X.-Q., Zhao, Y.-H., Chu, Y.-Q., et al. 2012, Research in Astronomy and Astrophysics, 12, 1197

Cutri, R. M., Skrutskie, M. F., van Dyk, S., et al. 2003, VizieR Online Data Catalog, II/246

Czesla, S., Schröter, S., Schneider, C. P., et al. 2019, PyA: Python astronomy-related packages

Dalton, G., Trager, S., Abrams, D. C., et al. 2014, in Society of Photo-Optical Instrumentation Engineers (SPIE) Conference Series, Vol. 9147, Ground-based and Airborne Instrumentation for Astronomy V, ed. S. K. Ramsay, I. S. McLean, & H. Takami, 91470L

Das, P. & Sanders, J. L. 2019, Mon. Not. R. Astron. Soc., 484, 294

de Jong, R. S., Agertz, O., Berbel, A. A., et al. 2019, The Messenger, 175, 3

De Silva, G. M., Freeman, K. C., Bland-Hawthorn, J., et al. 2015, Mon. Not. R. Astron. Soc., 449, 2604

Deason, A. J., Belokurov, V., Koposov, S. E., et al. 2017, Mon. Not. R. Astron. Soc., 470, 1259

Dekker, H., D'Odorico, S., Kaufer, A., Delabre, B., & Kotzlowski, H. 2000, in Society of Photo-Optical Instrumentation Engineers (SPIE) Conference Series, Vol. 4008, Optical and IR Telescope Instrumentation and Detectors, ed. M. Iye & A. F. Moorwood, 534–545

del Burgo, C. & Allende Prieto, C. 2018, Mon. Not. R. Astron. Soc., 479, 1953

Den Hartog, E. A., Lawler, J. E., Sneden, C., et al. 2021, Astrophys. J. Suppl., 255, 27

Di Matteo, P., Haywood, M., Lehnert, M. D., et al. 2019, Astron. Astrophys., 632, A4

Duong, L., Freeman, K. C., Asplund, M., et al. 2018, Mon. Not. R. Astron. Soc., 476, 5216

Edvardsson, B., Gustafsson, B., Andersen, J., et al. 1993, in Astronomische Gesellschaft Abstract Series, Vol. 8, Astronomische Gesellschaft Abstract Series, 105

Eggenberger, P. & Carrier, F. 2006, Astron. Astrophys., 449, 293

Elmegreen, B. G. & Elmegreen, D. M. 2005, Astrophys. J., 627, 632

Engels, D., Sherwood, W. A., Wamsteker, W., & Schultz, G. V. 1981, A&AS, 45, 5

Evans, Neal J., I., Levreault, R. M., Beckwith, S., & Skrutskie, M. 1987, Astrophys. J., 320, 364

Famaey, B., Antoja, T., Romero-Gomez, M., et al. 2016, in SF2A-2016: Proceedings of the Annual meeting of the French Society of Astronomy and Astrophysics, ed. C. Reylé, J. Richard, L. Cambrésy, M. Deleuil, E. Pécontal, L. Tresse, & I. Vauglin, 281–286

Feltzing, S. & Bensby, T. 2009, in IAU Symposium, Vol. 258, The Ages of Stars, ed. E. E. Mamajek, D. R. Soderblom, & R. F. G. Wyse, 23–30

Feuillet, D. K., Frankel, N., Lind, K., et al. 2019, Mon. Not. R. Astron. Soc., 489, 1742

Fields, B. D., Olive, K. A., Yeh, T.-H., & Young, C. 2020, Journal of Cosmology and Astroparticle Physics, 2020, 010

Freeman, K. & Bland-Hawthorn, J. 2002, ARA&A, 40, 487

Freytag, B., Steffen, M., Ludwig, H. G., et al. 2012, Journal of Computational Physics, 231, 919

Fuhrmann, K. 1998, Astron. Astrophys., 338, 161

Fuhrmann, K. 2004, Astronomische Nachrichten, 325, 3

Fuhrmann, K. 2008, Mon. Not. R. Astron. Soc., 384, 173

Gaia Collaboration. 2020, VizieR Online Data Catalog, I/350

Gaia Collaboration, Brown, A. G. A., Vallenari, A., et al. 2018, Astron. Astrophys., 616, A1

Gaia Collaboration, Brown, A. G. A., Vallenari, A., et al. 2020, arXiv e-prints, arXiv:2012.01533

Gaia Collaboration, Prusti, T., de Bruijne, J. H. J., et al. 2016, Astron. Astrophys., 595, A1

Gallagher, A. J., Bergemann, M., Collet, R., et al. 2020, Astron. Astrophys., 634, A55

Gallenne, A., Pietrzyński, G., Graczyk, D., et al. 2018, Astron. Astrophys., 616, A68

Gebek, A. & Matthee, J. 2021, arXiv e-prints, arXiv:2102.04561

Gehren, T., Liang, Y. C., Shi, J. R., Zhang, H. W., & Zhao, G. 2004, Astron. Astrophys., 413, 1045

Geller, A. M., Leiner, E. M., Bellini, A., et al. 2017, Astrophys. J., 840, 66

Gent, M. R., Bergemann, M., Serenelli, A., et al. 2022, Astron. Astrophys., 658, A147

Ghosh, S. K., Iyengar, K. V. K., Rengarajan, T. N., et al. 1984, Mon. Not. R. Astron. Soc., 206, 611

Giesers, B., Kamann, S., Dreizler, S., et al. 2019, Astron. Astrophys., 632, A3

Gilmore, G., Randich, S., Asplund, M., et al. 2012a, The Messenger, 147, 25

Gilmore, G., Randich, S., Asplund, M., et al. 2012b, The Messenger, 147, 25

Gilmore, G. & Reid, N. 1983, Mon. Not. R. Astron. Soc., 202, 1025

Glass, I. S. 1974, Monthly Notes of the Astronomical Society of South Africa, 33, 53

Gómez, G. C. 2010, in Astronomical Society of the Pacific Conference Series, Vol. 438, The Dynamic Interstellar Medium: A Celebration of the Canadian Galactic Plane Survey, ed. R. Kothes, T. L. Landecker, & A. G. Willis, 31

González Hernández, J. I. & Bonifacio, P. 2009, Astron. Astrophys., 497, 497

Goupil, M. 2017, in European Physical Journal Web of Conferences, Vol. 160, European Physical Journal Web of Conferences, 01003

Graczyk, D., Konorski, P., Pietrzyński, G., et al. 2017, Astrophys. J., 837, 7

Graczyk, D., Pietrzyński, G., Gieren, W., et al. 2019, Astrophys. J., 872, 85

Grand, R. J. J., Bustamante, S., Gómez, F. A., et al. 2018, Mon. Not. R. Astron. Soc., 474, 3629

Grevesse, N. & Sauval, A. J. 1998, Space Science Reviews, 85, 161

Gruberbauer, M., Guenther, D. B., & Kallinger, T. 2012, Astrophys. J., 749, 109

Grupp, F. 2004a, Astron. Astrophys., 420, 289

Grupp, F. 2004b, Astron. Astrophys., 426, 309

Gustafsson, B., Edvardsson, B., Eriksson, K., et al. 2008, Astron. Astrophys., 486, 951

Hayashi, H. & Chiba, M. 2006, PASJ, 58, 835

Hayden, M. R., Bovy, J., Holtzman, J. A., et al. 2015, Astrophys. J., 808, 132

Hayden, M. R., Recio-Blanco, A., de Laverny, P., Mikolaitis, S., & Worley, C. C. 2017, Astron. Astrophys., 608, L1

Hayes, C. R., Majewski, S. R., Shetrone, M., et al. 2018, The Astrophysical Journal, 852, 49

Haywood, M., Di Matteo, P., Lehnert, M. D., Katz, D., & Gómez, A. 2013, Astron. Astrophys., 560, A109

Haywood, M., Matteo, P. D., Lehnert, M. D., et al. 2018, The Astrophysical Journal, 863, 113

Haywood, M., Snaith, O., Lehnert, M. D., Di Matteo, P., & Khoperskov, S. 2019, Astron. Astrophys., 625, A105

Heiter, U., Jofré, P., Gustafsson, B., et al. 2015, Astron. Astrophys., 582, A49

Helmi, A. 2020, ARA&A, 58, 205

Helmi, A., Babusiaux, C., Koppelman, H. H., et al. 2018, Nature, 563, 85

Helmi, A. & de Zeeuw, P. T. 2000, Mon. Not. R. Astron. Soc., 319, 657

Higl, J., Siess, L., Weiss, A., & Ritter, H. 2018, Astron. Astrophys., 617, A36

Howes, L. M., Lindegren, L., Feltzing, S., Church, R. P., & Bensby, T. 2019, Astron. Astrophys., 622, A27

Huber, D., Bedding, T. R., Stello, D., et al. 2011, Astrophys. J., 743, 143

Huber, D., Chaplin, W. J., Christensen-Dalsgaard, J., et al. 2013, Astrophys. J., 767, 127

Jofré, P., Heiter, U., & Soubiran, C. 2019, ARA&A, 57, 571

Jofré, P., Heiter, U., Soubiran, C., et al. 2014, Astron. Astrophys., 564, A133

Jofré, P., Heiter, U., Tucci Maia, M., et al. 2018, Research Notes of the American Astronomical Society, 2, 152

Johnson, H. L. 1967, Astrophys. J., 149, 345

Johnson, H. L., Mcarthur, J. W., & Mitchell, R. I. 1968, Astrophys. J., 152, 465

Johnson, H. L., Mitchell, R. I., Iriarte, B., & Wisniewski, W. Z. 1966, Communications of the Lunar and Planetary Laboratory, 4, 99

Jönsson, H., Holtzman, J. A., Allende Prieto, C., et al. 2020, Astron. J., 160, 120

Jørgensen, B. R. & Lindegren, L. 2005, Astron. Astrophys., 436, 127

Joyce, M. & Chaboyer, B. 2018, Astrophys. J., 864, 99

Kazantzidis, S., Zentner, A. R., Kravtsov, A. V., Bullock, J. S., & Debattista, V. P. 2009, Astrophys. J., 700, 1896

Kervella, P., Thévenin, F., & Lovis, C. 2017, Astron. Astrophys., 598, L7

Kervella, P., Thévenin, F., Morel, P., et al. 2004, Astron. Astrophys., 413, 251

Khoperskov, S., Haywood, M., Snaith, O., et al. 2021, Mon. Not. R. Astron. Soc., 501, 5176

Kollmeier, J. A., Zasowski, G., Rix, H.-W., et al. 2017, arXiv e-prints, arXiv:1711.03234

Koppelman, H. H., Helmi, A., Massari, D., Price-Whelan, A. M., & Starkenburg, T. K. 2019, Astron. Astrophys., 631, L9

Kordopatis, G., Recio-Blanco, A., de Laverny, P., et al. 2011, Astron. Astrophys., 535, A107

Kordopatis, G., Wyse, R. F. G., Gilmore, G., et al. 2015, Astron. Astrophys., 582, A122

Kovalev, M., Bergemann, M., Ting, Y.-S., & Rix, H.-W. 2019, Astron. Astrophys., 628, A54

Kroupa, P. 2001, Mon. Not. R. Astron. Soc., 322, 231

Lancaster, L., Koposov, S. E., Belokurov, V., Evans, N. W., & Deason, A. J. 2019, Mon. Not. R. Astron. Soc., 486, 378

Laporte, C. F. P., Belokurov, V., Koposov, S. E., Smith, M. C., & Hill, V. 2020, Mon. Not. R. Astron. Soc., 492, L61

Laporte, C. F. P., Johnston, K. V., Gómez, F. A., Garavito-Camargo, N., & Besla, G. 2018, Mon. Not. R. Astron. Soc., 481, 286

Laporte, C. F. P., Johnston, K. V., & Tzanidakis, A. 2019a, Mon. Not. R. Astron. Soc., 483, 1427

Laporte, C. F. P., Koposov, S. E., & Belokurov, V. 2022, Mon. Not. R. Astron. Soc., 510, L13

Laporte, C. F. P., Minchev, I., Johnston, K. V., & Gómez, F. A. 2019b, Mon. Not. R. Astron. Soc., 485, 3134

Lee, Y. S., Beers, T. C., An, D., et al. 2011, Astrophys. J., 738, 187

Lian, J., Thomas, D., Maraston, C., et al. 2020, Mon. Not. R. Astron. Soc., 497, 2371

Liebert, J., Fontaine, G., Young, P. A., Williams, K. A., & Arnett, D. 2013, Astrophys. J., 769, 7

Lin, S., Tinker, J. L., Klypin, A., et al. 2020, Mon. Not. R. Astron. Soc.[[arXiv]2007.08996]

Lind, K., Amarsi, A. M., Asplund, M., et al. 2017, Mon. Not. R. Astron. Soc., 468, 4311

Lind, K., Bergemann, M., & Asplund, M. 2012, Mon. Not. R. Astron. Soc., 427, 50

Lineweaver, C. H. 1999, arXiv e-prints, astro

Liu, Z., Yang, W., Bi, S., et al. 2013, The Astrophysical Journal, 780, 152

Loebman, S. R., Roškar, R., Debattista, V. P., et al. 2011, Astrophys. J., 737, 8

Low, F. J. & Johnson, H. L. 1964, Astrophys. J., 139, 1130

Lund, M. N., Knudstrup, E., Silva Aguirre, V., et al. 2019, Astron. J., 158, 248

Mackereth, J. T., Bovy, J., Schiavon, R. P., et al. 2017, Mon. Not. R. Astron. Soc., 471, 3057

Mackereth, J. T., Crain, R. A., Schiavon, R. P., et al. 2018, Mon. Not. R. Astron. Soc., 477, 5072

Madau, P. & Dickinson, M. 2014, ARA&A, 52, 415

Maderak, R. M., Deliyannis, C. P., Anthony-Twarog, B. J., et al. 2015, Astron. J., 149, 141

Magic, Z., Collet, R., Asplund, M., et al. 2013a, Astron. Astrophys., 557, A26

Magic, Z., Collet, R., Hayek, W., & Asplund, M. 2013b, Astron. Astrophys., 560, A8

Magrini, L., Randich, S., Kordopatis, G., et al. 2017, Astron. Astrophys., 603, A2

Majewski, S. R., Schiavon, R. P., Frinchaboy, P. M., et al. 2017, Astron. J., 154, 94

Majewski, S. R., Skrutskie, M. F., Schiavon, R. P., et al. 2007, in American Astronomical Society Meeting Abstracts, Vol. 211, American Astronomical Society Meeting Abstracts, 132.08

Martínez-Barbosa, C. A., Brown, A. G. A., & Portegies Zwart, S. 2014, in EAS Publications Series, Vol. 67-68, EAS Publications Series, 123–126

Mashonkina, L., Sitnova, T., & Belyaev, A. K. 2017, Astron. Astrophys., 605, A53

Mayor, M., Pepe, F., Queloz, D., et al. 2003, The Messenger, 114, 20

McMahon, R. G., Banerji, M., Gonzalez, E., et al. 2013, The Messenger, 154, 35

McMillan, P. J. 2016, Monthly Notices of the Royal Astronomical Society, 465, 76

McMillan, P. J. 2017, Mon. Not. R. Astron. Soc., 465, 76

McMillan, P. J., Kordopatis, G., Kunder, A., et al. 2018, Mon. Not. R. Astron. Soc., 477, 5279

Mikolaitis, Š., Hill, V., Recio-Blanco, A., et al. 2014, Astron. Astrophys., 572, A33

Minchev, I., Chiappini, C., & Martig, M. 2013, Astron. Astrophys., 558, A9

Minchev, I. & Famaey, B. 2010, in EAS Publications Series, Vol. 45, EAS Publications Series, 299–302

Minchev, I., Famaey, B., Combes, F., et al. 2011, Astron. Astrophys., 527, A147

Miranda, M. S., Pilkington, K., Gibson, B. K., et al. 2016, Astron. Astrophys., 587, A10

Mitschang, A. W., De Silva, G., Zucker, D. B., et al. 2014, Monthly Notices of the Royal Astronomical Society, 438, 2753

Monroe, T. R., Meléndez, J., Ramírez, I., et al. 2013, Astrophys. J. Lett., 774, L32

Montalto, M., Piotto, G., Marrese, P. M., et al. 2021, arXiv e-prints, arXiv:2108.13712

Mortier, A., Sousa, S. G., Adibekyan, V. Z., Brandão, I. M., & Santos, N. C. 2014, Astron. Astrophys., 572, A95

Moster, B. P., Macciò, A. V., Somerville, R. S., Naab, T., & Cox, T. J. 2012, Mon. Not. R. Astron. Soc., 423, 2045

Mourard, D., Bério, P., Perraut, K., et al. 2017, Journal of the Optical Society of America A, 34, A37

Myeong, G. C., Evans, N. W., Belokurov, V., Sanders, J. L., & Koposov, S. E. 2018, Astrophys. J. Lett., 856, L26

Naidu, R. P., Conroy, C., Bonaca, A., et al. 2021, Astrophys. J., 923, 92

Naidu, R. P., Tacchella, S., Mason, C. A., et al. 2020, Astrophys. J., 892, 109

Nandakumar, G., Hayden, M. R., Sharma, S., et al. 2020, arXiv e-prints, arXiv:2011.02783

Nandakumar, G., Schultheis, M., Hayden, M., et al. 2017, Astron. Astrophys., 606, A97

Nardetto, N. 2018, arXiv e-prints, arXiv:1801.04158

Nascimbeni, V., Piotto, G., Börner, A., et al. 2022, Astron. Astrophys., 658, A31

Navarro, J. F., Abadi, M. G., Venn, K. A., Freeman, K. C., & Anguiano, B. 2011, Mon. Not. R. Astron. Soc., 412, 1203

Ness, M., Hogg, D. W., Rix, H. W., Ho, A. Y. Q., & Zasowski, G. 2015, Astrophys. J., 808, 16

Ness, M. & Lang, D. 2016, Astron. J., 152, 14

Newberg, H. J., Yanny, B., Rockosi, C., et al. 2002, Astrophys. J., 569, 245

Nidever, D. L., Bovy, J., Bird, J. C., et al. 2014, Astrophys. J., 796, 38

Nissen, P. E. & Schuster, W. J. 2010, Astron. Astrophys., 511, L10

Nissen, P. E., Silva Aguirre, V., Christensen-Dalsgaard, J., et al. 2017, Astron. Astrophys., 608, A112

Nordlund, Å., Stein, R. F., & Asplund, M. 2009, Living Reviews in Solar Physics, 6, 2

Nordström, B., Andersen, J., Holmberg, J., et al. 2004a, PASA, 21, 129

Nordström, B., Mayor, M., Andersen, J., et al. 2004b, The Messenger, 118, 61

Offner, S. S. R., Clark, P. C., Hennebelle, P., et al. 2014, in Protostars and Planets VI, ed. H. Beuther, R. S. Klessen, C. P. Dullemond, & T. Henning, 53

Pagel, B. E. J. & Edmunds, M. G. 1981, ARA&A, 19, 77

Palla, M., Matteucci, F., Spitoni, E., Vincenzo, F., & Grisoni, V. 2020, arXiv e-prints, arXiv:2008.07484

Pannetier, C., Mourard, D., Berio, P., et al. 2020, in Society of Photo-Optical Instrumentation Engineers (SPIE) Conference Series, Vol. 11446, Society of Photo-Optical Instrumentation Engineers (SPIE) Conference Series, 114460T

Perryman, M. A. C., Lindegren, L., Kovalevsky, J., et al. 1997a, Astron. Astrophys., 500, 501

Perryman, M. A. C., Lindegren, L., Kovalevsky, J., et al. 1997b, Astron. Astrophys., 500, 501

Pietrzyński, G., Graczyk, D., Gallenne, A., et al. 2019, Nature, 567, 200

Pinsonneault, M. H., Elsworth, Y. P., Tayar, J., et al. 2018, Astrophys. J. Suppl., 239, 32

Piskunov, N. & Valenti, J. A. 2017, Astron. Astrophys., 597, A16

Plez, B. 2012, Turbospectrum: Code for spectral synthesis, ascl:1205.004

Pont, F. & Eyer, L. 2004, Mon. Not. R. Astron. Soc., 351, 487

Pourbaix, D. & Boffin, H. M. J. 2016, Astron. Astrophys., 586, A90

Price-Whelan, A. M., Sipőcz, B. M., Günther, H. M., et al. 2018, Astron. J., 156, 123

Prša, A., Harmanec, P., Torres, G., et al. 2016, The Astronomical Journal, 152, 41

Prudil, Z., Dékány, I., Grebel, E. K., & Kunder, A. 2020, Mon. Not. R. Astron. Soc., 492, 3408

Quillen, A. C., Minchev, I., Bland-Hawthorn, J., & Haywood, M. 2009, Mon. Not. R. Astron. Soc., 397, 1599

Rains, A. D., Ireland, M. J., White, T. R., Casagrande, L., & Karovicova, I. 2020, Mon. Not. R. Astron. Soc., 493, 2377

Randich, S., Gilmore, G., & Gaia-ESO Consortium. 2013, The Messenger, 154, 47

Randich, S., Gilmore, G., Magrini, L., et al. 2022, Astron. Astrophys., 666, A121

Rauer, H., Aerts, C., Cabrera, J., & PLATO Team. 2016, Astronomische Nachrichten, 337, 961

Rauer, H., Catala, C., Aerts, C., et al. 2014, Experimental Astronomy, 38, 249

Read, J. I., Lake, G., Agertz, O., & Debattista, V. P. 2008, Mon. Not. R. Astron. Soc., 389, 1041

Recio-Blanco, A., Bijaoui, A., & de Laverny, P. 2006, Mon. Not. R. Astron. Soc., 370, 141

Recio-Blanco, A., de Laverny, P., Kordopatis, G., et al. 2014, Astron. Astrophys., 567, A5

Recio-Blanco, A., de Laverny, P., Palicio, P. A., et al. 2022, arXiv e-prints, arXiv:2206.05541

Reddy, B. E., Lambert, D. L., & Allende Prieto, C. 2006, Mon. Not. R. Astron. Soc., 367, 1329

Reid, M. J., Menten, K. M., Brunthaler, A., et al. 2014, Astrophys. J., 783, 130

Ricker, G. R., Winn, J. N., Vanderspek, R., et al. 2015, Journal of Astronomical Telescopes, Instruments, and Systems, 1, 014003

Rix, H.-W., Ting, Y.-S., Conroy, C., & Hogg, D. W. 2016, Astrophys. J. Lett., 826, L25

Rocha-Pinto, H. J., Maciel, W. J., Scalo, J., & Flynn, C. 2000, Astron. Astrophys., 358, 850

Roth, M., Echevarria, J., Tapia, M., et al. 1984, Astron. Astrophys., 137, L9

Ruchti, G. R., Bergemann, M., Serenelli, A., Casagrande, L., & Lind, K. 2013, Mon. Not. R. Astron. Soc., 429, 126

Ruchti, G. R., Fulbright, J. P., Wyse, R. F. G., et al. 2011, Astrophys. J., 737, 9

Rybizki, J., Just, A., & Rix, H.-W. 2017, Astron. Astrophys., 605, A59

Sahlholdt, C. L., Feltzing, S., & Feuillet, D. K. 2022, Mon. Not. R. Astron. Soc., 510, 4669

Sahlholdt, C. L., Feltzing, S., Lindegren, L., & Church, R. P. 2019, Mon. Not. R. Astron. Soc., 482, 895

Salpeter, E. E. 1955, Astrophys. J., 121, 161

Salsi, A., Nardetto, N., Mourard, D., et al. 2020, Astron. Astrophys., 640, A2

Salsi, A., Nardetto, N., Mourard, D., et al. 2021, Astron. Astrophys., 652, A26

Sbordone, L., Bonifacio, P., Caffau, E., et al. 2010, Astron. Astrophys., 522, A26

Schlesinger, K. J., Johnson, J. A., Rockosi, C. M., et al. 2014, Astrophys. J., 791, 112

Schönrich, R. 2012, Mon. Not. R. Astron. Soc., 427, 274

Schönrich, R. & Bergemann, M. 2014, Monthly Notices of the Royal Astronomical Society, 443, 698

Schönrich, R. & Binney, J. 2009a, Mon. Not. R. Astron. Soc., 396, 203

Schönrich, R. & Binney, J. 2009b, Mon. Not. R. Astron. Soc., 396, 203

Schönrich, R. & Binney, J. 2009c, Mon. Not. R. Astron. Soc., 399, 1145

Schönrich, R. & Binney, J. 2009d, Mon. Not. R. Astron. Soc., 399, 1145

Searle, L. 1971, Astrophys. J., 168, 327

Seifert, W., Xu, W., Buschkamp, P., et al. 2016, in Society of Photo-Optical Instrumentation Engineers (SPIE) Conference Series, Vol. 9908, Ground-based and Airborne Instrumentation for Astronomy VI, ed. C. J. Evans, L. Simard, & H. Takami, 990890

Selby, M. J., Hepburn, I., Blackwell, D. E., et al. 1988, A&AS, 74, 127

Sellwood, J. A. & Binney, J. J. 2002, Mon. Not. R. Astron. Soc., 336, 785

Semenova, E., Bergemann, M., Deal, M., et al. 2020, Astron. Astrophys., 643, A164

Serenelli, A., Johnson, J., Huber, D., et al. 2017, Astrophys. J. Suppl., 233, 23

Serenelli, A. M., Bergemann, M., Ruchti, G., & Casagrande, L. 2013, Mon. Not. R. Astron. Soc., 429, 3645

Sharma, S., Stello, D., Bland-Hawthorn, J., et al. 2019, Mon. Not. R. Astron. Soc., 490, 5335

Silva Aguirre, V., Bojsen-Hansen, M., Slumstrup, D., et al. 2018, Mon. Not. R. Astron. Soc., 475, 5487

Silva Aguirre, V., Lund, M. N., Antia, H. M., et al. 2017, Astrophys. J., 835, 173

Simpson, C. M., Gargiulo, I., Gómez, F. A., et al. 2019, Mon. Not. R. Astron. Soc., 490, L32

Skrutskie, M. F., Cutri, R. M., Stiening, R., et al. 2006, Astron. J., 131, 1163

Sofue, Y. 2020, Galaxies, 8, 37

Sonoi, T., Ludwig, H. G., Dupret, M. A., et al. 2019, Astron. Astrophys., 621, A84

Spite, F. & Spite, M. 1982, Astron. Astrophys., 115, 357

Spitoni, E., Silva Aguirre, V., Matteucci, F., Calura, F., & Grisoni, V. 2019, Astron. Astrophys., 623, A60

Stanghellini, L., Berg, D., Bresolin, F., Cunha, K., & Magrini, L. 2019, arXiv e-prints, arXiv:1905.04096

Steigman, G. 2007, Annual Review of Nuclear and Particle Science, 57, 463

Steinmetz, M., Guiglion, G., McMillan, P. J., et al. 2020, Astron. J., 160, 83

Steinmetz, M., Zwitter, T., Siebert, A., et al. 2006, The Astronomical Journal, 132, 1645

Steinmetz, M., Zwitter, T., Siebert, A., et al. 2006, Astron. J., 132, 1645

Stewart, K. R., Bullock, J. S., Wechsler, R. H., & Maller, A. H. 2009, Astrophys. J., 702, 307

Stonkutė, E., Koposov, S. E., Howes, L. M., et al. 2016, Mon. Not. R. Astron. Soc., 460, 1131

Tapia, M., Roth, M., Costero, R., & Navarro, S. 1984, , 9, 65

ten Brummelaar, T. A., McAlister, H. A., Ridgway, S. T., et al. 2005, Astrophys. J., 628, 453

Thévenin, F., Kervella, P., Pichon, B., et al. 2005, Astron. Astrophys., 436, 253

Thompson, B. B., Few, C. G., Bergemann, M., et al. 2018, Mon. Not. R. Astron. Soc., 473, 185

Thoul, A. A., Bahcall, J. N., & Loeb, A. 1994, Astrophys. J., 421, 828

Ting, Y.-S., Conroy, C., & Rix, H.-W. 2016, Astrophys. J., 826, 83

Ting, Y.-S., Conroy, C., Rix, H.-W., & Cargile, P. 2019, The Astrophysical Journal, 879, 69

Tolstoy, E., Hill, V., & Tosi, M. 2009, ARA&A, 47, 371

Tsantaki, M., Santos, N. C., Sousa, S. G., et al. 2019, Mon. Not. R. Astron. Soc., 485, 2772

Valenti, J. A. & Piskunov, N. 1996, A&AS, 118, 595

van Belle, G. T., Ciardi, D. R., & Boden, A. F. 2007, Astrophys. J., 657, 1058

van Dokkum, P. G., Leja, J., Nelson, E. J., et al. 2013, Astrophys. J. Lett., 771, L35

van Leeuwen, F. 2007, Astron. Astrophys., 474, 653

VandenBerg, D. A., Bergbusch, P. A., Dotter, A., et al. 2012, Astrophys. J., 755, 15

Vasiliev, E. 2019, Mon. Not. R. Astron. Soc., 482, 1525

Veeder, G. J., Matson, D. L., & Smith, J. C. 1978, Astron. J., 83, 651

Vera-Ciro, C., D'Onghia, E., & Navarro, J. F. 2016, Astrophys. J., 833, 42

Vernazza, J. E., Avrett, E. H., & Loeser, R. 1981, Astrophys. J. Suppl., 45, 635

Villalobos, Á. & Helmi, A. 2008, Mon. Not. R. Astron. Soc., 391, 1806

Villalobos, Á., Kazantzidis, S., & Helmi, A. 2010, Astrophys. J., 718, 314

Vögler, A., Shelyag, S., Schüssler, M., et al. 2005, Astron. Astrophys., 429, 335

Weiss, A. & Schlattl, H. 2008, Ap&SS, 316, 99

Wheeler, A., Ness, M., Buder, S., et al. 2020, Astrophys. J., 898, 58

White, M. & Croft, R. A. C. 2000, Astrophys. J., 539, 497

White, T. R., Bedding, T. R., Stello, D., et al. 2011, Astrophys. J., 743, 161

White, T. R., Huber, D., Maestro, V., et al. 2013, Mon. Not. R. Astron. Soc., 433, 1262

Wu, T. & Li, Y. 2017, Astrophys. J., 846, 41

Xiang, M. & Rix, H.-W. 2022, arXiv e-prints, arXiv:2203.12110

Xiang, M., Ting, Y.-S., Rix, H.-W., et al. 2019, Astrophys. J. Suppl., 245, 34

Yanny, B., Rockosi, C., Newberg, H. J., et al. 2009, Astron. J., 137, 4377